Oscillations of rapidly rotating neutron stars

Dissertation

zur Erlangung des Grades eines Doktors
der Naturwissenschaften
der Fakultät für Mathematik und Physik
zu Eberhard-Karls-Universität zu Tübingen

vorgelegt von
Efstratios Boutloukos
aus Amsterdam

2006

Tag der mündlichen Prüfung:	18.08.2006
Dekan:	Prof. Dr. Peter Schmid
1. Berichterstatter:	P.D. Dr. Hans-Peter Nollert
2. Berichterstatter:	Prof. Dr. Willhelm Kley

Abstract

Neutron stars are one of the possible products of the evolution of stars, consisting of the most compact form of matter with dimensions. The concentration of mass more than the solar one within about 20km, requires general relativistic description, with the equation of state governing the physics still being largely unknown. The observational analogue of neutron stars are believed to be pulsars, which are found to rotate with periods down to $\sim$ 1msec. Rapidly rotating compact objects like these, are extremely interesting for physics, since they provide conditions that could hardly be produced in a laboratory on earth.

Electromagnetic radiation is, so far, the only way to observe and study these objects, with gravitational waves being the promising new window that general theory of relativity has predicted to open in the future. The recent technological achievements in laser interferometry are just enabling detection of such waves from our galaxy. Apart from sudden violent events, such as collisions between two compact obects, oscillations from single neutron stars are also a good source for gravitational wave signals. Excited through various astrophysical scenaria, some oscillations can become unstable and emit gravitational waves for a sufficient amount of time to be received and detected from earth. The knowledge of the properties of the oscillations (eg. frequency and damping time) is required for tuning the detectors and has been the goal of various studies. A fully relativistic 3-dimensional numerical time evolution would resolve the problem, being though hardly conceivable due to computational limitations. Various approximations have given contradictory results in the past, mainly due to the failure of the applied spherical symmetry to describe rotating neutron stars. We therefor attack this problem in a simplified but consistent way, and aim to reveal some fundamental aspects of neutron star oscillations.

We use linearized perturbation theory to describe the oscillations of neutron stars modeled by polytropic equations of state. In the limit of no rotation we adopt a spherically symmetric background and are able to confirm results of previous studies, finding an infinite spectrum of pressure driven modes at frequencies above about 2kHz as well as oscillations of the spacetime at frequencies of about 10kHz. The two groups of modes have in this case different character, with the first having even parity (polar modes) and the latter odd parity (axial modes).

For rotating stars we use an axisymmetric background, with the perturbations having a $e^{im\phi}$-behavior and a series of associated Legendre polynomials, P_ℓ^m, describing their θ-dependence. The equations grow though now much more lengthy, and the numerical implementation becomes more difficult. We therefore adopt an approximation (so-called "Cowling") that was found to give consistent and quite accurate results in no rotation, by neglecting the perturbations of the spacetime and concentrating on the fluid perturbations. By this, an eigenvalue problem is formed, solved for all possible solutions.

Next to the infinite set of pressure modes, we also found the modes driven by rotation (inertial modes). They also form an infinite set, but are confined in a frequency range dependent from the rotational frequency and the compactness of the star. The presence of a corresponding continuous spectrum could not be excluded. For values of the azimuthal index $m \geq 2$, all the inertial modes are unstable and for increasingly high m they tend to move into the range of frequencies of the pressure modes.

While pressure modes were easily identified both through their eigenfunctions as well as via their frequencies, for inertial modes the same task was more tedious. The dense frequency distribution of modes requires looking at the eigenfunctions, but these have, in this case, a complicated behavior, owing to the contribution from several ℓ that form the mode. Still, individual modes have been identified and could be followed for increasing resolution. Based on the characteristics of the θ-part of the velocity perturbation from other studies on the fundamental r-mode, we found a mode resembling these criteria for a slowly rotating model; its frequency –1.41 times the spin frequency of the star– is in agreement with previous results in that regime. For a rapidly rotating neutron star model, a similar mode can still be identified, with its eigenfunction deviating though more from the expected form, and its frequency being higher (rather than lower as expected by other studies) than in slow rotation.

Despite the discoveries of general properties of the inertial mode spectrum, the identification of modes in there might still be problematic. Reason for that is the presence of the infinite set of inertial modes – which might as well be continuous –that could even not allow the existence of the r-mode. But even if present, its behavior is probably numerically influenced by the neighboring solutions, which could even lead to misidentifying it, especially for rapid rotation. Larger memory power would allow increasing the resolution of the problem and possibly the clarification of the above questions. Numerical 3D evolution could also provide a definite answer, while a successful detection of such a mode through gravitational waves would be the final confirmation of the existence of unstable modes.

A search for a signature of a neutron star's non-radial modes in the electromagnetic spectrum the low-mass X-ray binary Circinus X-1 could not support the connection between quasi-periodic oscillations (QPOs) and quasi-normal modes, but did extend the observed range of kHz QPO frequencies to a new regime providing a unique test for QPO-models. The frequency-frequency correlations confirmed the identification of the underlying compact object as a neutron star.

Contents

Oscillations of rapidly rotating neutron stars

Stratos Boutloukos

October 16, 2006

Part I

Neutron star oscillations as sources of gravitational waves

Chapter 1

Introduction

1.1 Motivation

Neutron stars are the most compact form of matter that gravity allows to have dimensions in astronomical scales. Due to this compactness, even small perturbations in the equilibrium of such objects could be violent enough to produce a strong signal (mainly through gravitational wave emission) detectable from the earth. A wealth of information has been retrieved in the past through the study of oscillations (in the electromagnetic spectrum) from much less compact objects such as the sun or variable stars. A brief summary of the achievements of the so-called asteroseismology will be given below, together with further motivation for the search for gravitational waves from neutron star oscillations.

Radial oscillations have long been observed from variables stars such as Cepheids, RR Lyrae and Mira variables. Non-radial oscillations were though first considered as the reason for producing the variabilities in the spectrum of a β Cephei (β Canis Majoris) in 1951 by Ledoux. The breakthrough was achieved in 1962 by Leighton, Noyes and Simon who discovered the 5-minute-oscillation of the sun. By now, hundreds of the sun's pressure modes, as well as some low-order gravity modes are seen in its spectrum (see below for the definition of these modes). The study of their frequencies and further characteristics is a branch in astronomy by itself, called helioseismology, and contributed the most towards our knowledge about the inner composition of the sun. In the meanwhile, non-radial oscillations have been identified from many other stars, such as Ap stars, early type O and B stars and even white dwarfs. Dependent mainly on the compactness of the star, these frequencies can be as low as 0.1 mHz for pressure-modes and one order of magnitude smaller for gravity-modes, while for white dwarfs they have been observed up to 10 mHz.

Just as every physical body, neutron stars also retain their own distinct set of oscillation modes, at which they oscillate when excited. The character and frequencies of these modes depend on the neutron star model. We concentrate here on isentropic models, where a star's equilibrium as well as its perturbations

can be described with the same one-parameter equation of state $p = p(\epsilon)$ and constant entropy (Lockitch and Friedman, 1999) (also called barotropic (Lockitch *et al*, 2004)). Deviations from an isentropic model become important only if the radian spin frequency is comparable to or smaller than the Brunt-Väisälä frequency, which for neutron stars is on the order of 100Hz (Lockitch *et al*, 2001). Otherwise, stars retain a set of pressure modes (p-modes) as well as one of inertial modes. For models with composition gradient or finite temperature, the star would allow also many gravity modes (g-modes) to be excited. A short summary of the properties of these families of modes, as attained by previous analyses is given below.

A rich oscillation spectrum exists for any neutron star model. Since, under several circumstances, a family of modes can be degenerate in frequency, we preferably define a mode from its eigenfunction. Assuming a spherically symmetric background, the angular behavior of a mode can be expressed as a spherical harmonic ($Y_{\ell m}$) and specific values of the harmonic indices can be assigned to it. If the perturbations behave like $(-1)^{\ell}$ under space iversion, they are called even or polar ones; odd or axial ones have $(-1)^{\ell+1}$ parity. Along the surface of constant radius, a mode will have ℓ nodal lines: m azimuthal ones and $\ell - m$ in the θ-direction (see eg. Unno *et al*, 1989). Along the radial direction a fundamental mode will not have any nodes, while, for example, the second overtone will have two nodes. For the classification of the modes for various models we need, however, to look at their eigenfrequencies as well.

The pressure modes were the first to be studied since they exist even for constant density stars ("MacLaurin spheroids" or "incompressible fluids") in Newtonian gravity. The lowest-frequency mode (the fundamental (f-) mode) has then a frequency that is given by

$$\sqrt{\frac{2\ell(\ell-1)}{2\ell+1}\frac{M}{R^3}}$$

while for several equations of state it gets values of about 2.3kHz $\pm$ $\sim$700Hz. Rotation does not significantly affect the pressure mode frequencies up to rotation rates of about half the break-up frequency (Font *et al*, 2001). For faster rotation, the f-mode decreases in frequency for several 100 Hz. For some neutron star models rotation close to the break-up frequency brings the f-mode to the zero-frequency plane, marking its instability (see below). There are infinitely many pressure modes with increasingly high frequencies.

Inertial modes are called the ones that are driven by rotation and have thus zero frequency for non-rotating stars. In the spherical limit they have pure axial parity, in contrast to the g-modes that have polar one. In isentropic models rotation causes a mixture of axial and polar parity, leading to what was occasionally called 'hybrid modes'. In non-isentropic stars the inertial modes would retain pure axial parity and were named r-modes due to their similarity with the Rossby waves of terrestrial mechanics. In Newtonian physics the $\ell = m$ inertial modes of isentropic stars have still pure axial nature, with the fundamental one

having frequency

$$\sigma = m\Omega \left[1 - \frac{2}{\ell(\ell+1)}\right];$$

in general relativity all modes (apart from the dipole ones) have mixed parity. There is an infinite number of inertial modes for relativistic isentropic stars (Lockitch *et al*, 2004), with their frequencies being typically several 100 Hz.

For a review regarding fluid oscillations of neutron stars see Nollert (1999) and Kokkotas and Schmidt (1999); equilibria and perturbations of rotating neutron stars bare reviewed by Stergioulas (2003) while Andersson and Kokkotas (2001) concentrate on r-modes.

Physical phenomena that can lead to excitation of various modes are the very birth of a neutron star after a supernova explosion, where the proto-neutron star is hot and rapidly rotating, as well as the infall of matter at accreting neutron stars which form binary systems with a main-sequence companion. Compact binaries are also expected to excite fluid oscillations at the latest stage of evolution, when the separation becomes of the same order as the size of the stars.

In order to be able to observe oscillations, a mechanism is needed to bring the oscillation amplitudes to high level and preferably keep them there for a significant amount of time. Instabilities are shown to be doing that work, and can play an important role in neutron star physics. Friedman and Schutz (1978) (after Chandrasekhar (1970)) showed with the so-called CFS instability that modes can become unstable, depending on their frequency with respect to the rotational frequency of the star and the character of the mode.

Andersson (1998) discovered that the r-modes are unstable for any rotation rate of a perfect fluid star. In presence of dissipation, the modes will grow in amplitude until saturation is reached, with the whole procedure being determined by its growth time and the damping times of these anticipating mechanisms (Andersson, 2003). Since the discovery of this new class of unstable modes, much excitement was spread among the scientific community concerning the detectability of such modes through gravitational waves, and consequently a lot of studies were devoted on testing the growth of these modes. Most challenging are the presence of strong magnetic fields (Rezzolla, Lamb & Shapiro, 2000) and the non-linear coupling with other (higher order) modes (Brink *et al*, 2004a), while the presence of a crust and hyperons in the core can also limit the instability. Since not only the saturation amplitude does determine the detectability but also the duration of the instability, the r-modes[1] are still considered an important source for gravitational waves.

The same mechanism can also cause the f-mode of a neutron star to become unstable. Still, this occurs only when the rotation frequency of the star is close to the Kepler limit (Yoshida & Eriguchi, 1999); this is, however, expected to be the case for a newly born neutron star. Many g-modes can become unstable as well, although their growth is most likely suppressed by viscous dissipation

[1] We will be referring to r-modes also for relativistic stars even though they are defined in Newtonian gravity, and their character in general relativity is different.

(Lai, 1999). The latter are related to either composition gradient or finite temperature, which are not considered in this work.

Gravitational waves The reason for all this excitement is the perspective of opening a new window in astronomy through gravitational waves. Their prediction in the framework of general relativity has initiated laborious attempts to detect such from astrophysical sources. Due to the weak interaction with matter, one needs quite a strong signal to be observable. Even our nearby sun cannot produce any sufficient gravitational wave emission. Since a time-varying quadruple moment is necessary for the emission of gravitational waves, one needs a non-spherical-symmetric motion of compact matter for that. The best sources therefor are black holes and neutron stars, with the mass of the object determining how far away such a signal can be seen. More violent events, like collisions of two compact objects, will of course produce a much stronger signal, whose duration though will be shorter and the probability of occurrence in an observable distance might eventually be smaller. Oscillation modes, on the other hand, are present for an extended period of time and according to the instability scenario above, can be excited to large amplitude to be observed from the earth. Apart from the many more sources in our galaxy, the long duration of such a signal can especially advance the search of such a signal through continuous observations with matched filtering.

Especially exciting are the information that one can draw out of observing one or more oscillations from a neutron star. Andersson & Kokkotas (1998) computed the frequencies and damping times of the fundamental pressure mode and a w(ave)-mode of non-rotating stars for several equations of state, and found that there is a well-defined relation between the frequency of the mode and the compactness of the star, as well as between the damping time and the mean density (Fig. 1.1). In the case of observing an oscillation mode from a neutron star one could estimate through these relations both M/R and M/R^3, ie. determine the mass *and* the radius of the neutron star, still a holy grail in astronomy. Depending on the mode observed, this procedure can be direct or iterative by excluding some equations of state and then rather restricting the parameters in a narrow range. By including rotation into the analysis, also the spin frequency can be determined, but also more observation would be needed.

Gravitational wave astronomy is just reaching the sensitivity required for such observations after many years of technical development. The bar detectors that paved the way and occasionally produced some excitement by coincidences likely related to gravitational waves (Astone *et al*, 2002) are now being overtaken by laser interferometers. GEO-600 in Hanover and LIGO in Stanford and Livingston (followed by TAMA in Japan and VIRGO in Italy) are carrying the hopes of this – still young – research area; common science runs and data analysis are already taken between the two groups, with the most recent one (S4 during 2005) marking the attainment of the planed sensitivity of the current stage and spreading optimism for a doubtless detection within short time. The first source seen can be a violent event, such as a compact binary merger in

Figure 1.1: The real and (normalized) imaginary part of the f-mode frequency for various equations of state (from Andersson & Kokkotas (1998)).

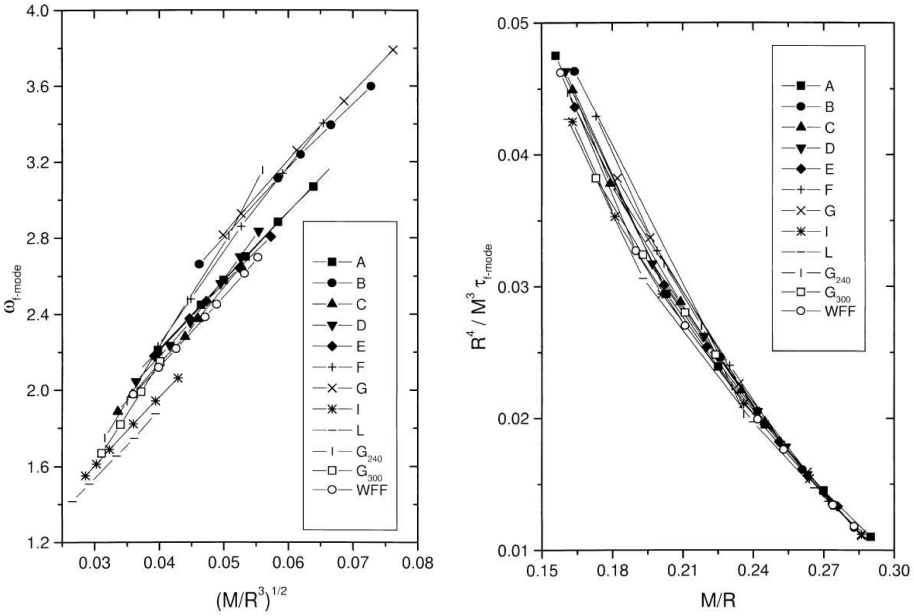

the Milky Way or a supernova explosion in the solar neighborhood, but can also be a careful observation of a persistent emission, eg. through neutron star oscillations. The number density of compact binaries is being corrected down, bringing up again the attention to r-modes and other unstable neutron star oscillations. The planed update of GEO-600 is a unique opportunity of adopting special techniques to advance observations in the frequency range needed for the above, ie. in the few hundred up to kHz range. Narrow-banding in high frequencies is indeed well considered as the next generation form of operation of GEO-600, which should be ready by 2010 (Willke *et al*, 2006), see fig. 1.2. In the meanwhile the suspense rises about when gravitational waves will be observed and whether the first source ever seen might be from neutron star oscillations.

1.2 Previous work

The astrophysical importance of neutron stars oscillations and their relevance to gravitational waves gave rise to numerous works towards calculating their properties analytically as well as numerically. Perturbation theory provided a first tool towards this direction and set the baseline of our current knowledge. As a first step, the early studies had used simplified physics, such as Newtonian gravity, no rotation and incompressible fluids. As a more realistic description, the slow-rotation approximation and polytropic equations of state were used,

Figure 1.2: The sensitivity curve of the planed high-frequency upgrade of GEO-600 for three cases of fine-tuning (after Hough (2004).)

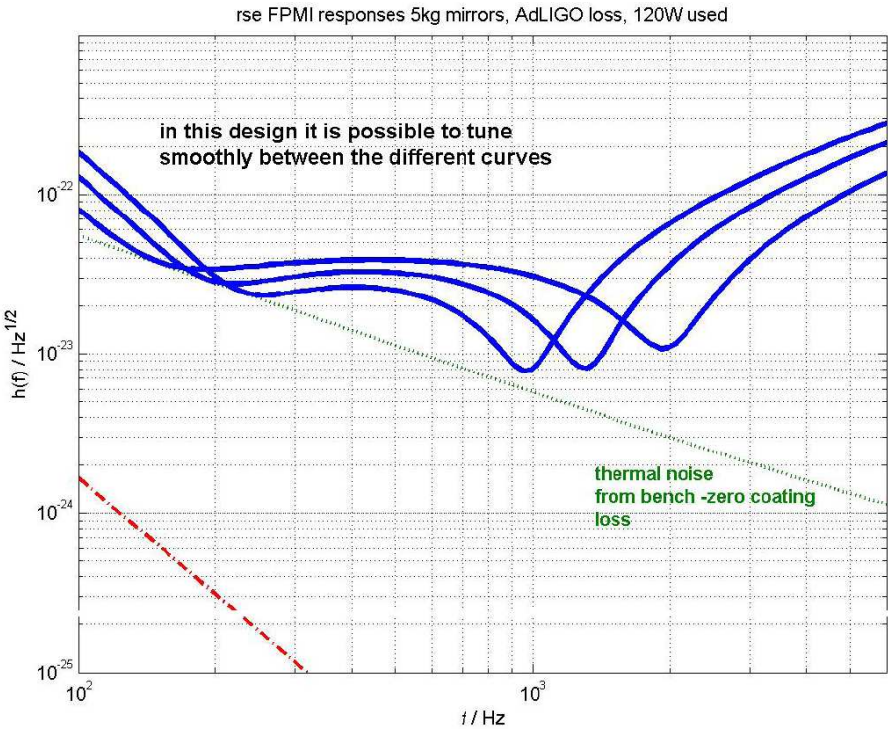

while the relativistic Cowling approximation (fixed spacetime, see later in this section) proved to be more than 80% accurate compared to fully relativistic results. Recently, full 3D relativistic time-evolutions became possible, and rapid rotation combined with relativistic gravity are giving the first results, but still a lot of questions are open. We review here the results attained so far with several approaches and point out what is still missing.

In Newtonian gravity the perturbation equation describing the frequencies of pressure modes is of Sturm-Liouville type (see eg. Cowling, 1941) and the solution is an infinite set of modes with a frequency range unbound from above. This analysis was extended in a relativistic framework (see eg. Thorne & Campolattaro, 1967; Detweiler & Lindblom, 1985), but as Chandrasekhar & Ferrari (1995) showed, the relativistic modes have a one-to-one analogy with the Newtonian ones as the models get less and less relativistic.

The range of frequencies that the inertial modes cover has been studied in the same framework (see Greenspan, 1968) and is found to be finite. Lindblom and Ipser (1999) found for Newtonian incompressible stars the analytic solutions to extend from $(-2-m)\nu$ to $(2-m)\nu$ where ν is the rotational frequency of the star and m the azimuthal index. Later Brink *et al* (2004) computed a large

set of such modes in the same framework and confirmed modes up to 30th order to have frequencies confined within this range. Ruoff *et al* (2003) studied the inertial mode spectrum for relativistic barotropic (as well as non-barotropic) stars in the slow-rotation approximation by including coupling of modes up to a maximum harmonic index ℓ_{max}. Next to distinct inertial modes they found a continuous spectrum whose width depends on the compactness of the star and on ℓ_{max}. They all lie roughly between $-\nu$ and ν for $m = 0$ and between -2ν and 0 for $m = 2$. For $\ell_{max} \to \infty$ the authors expect the continuous spectrum to fully cover this range with individual modes still existing inside the continuous spectrum. On the other hand, Lockitch *et al* (2004) argue in their appendix that only individual modes should be present.

Most studies of neutron star oscillations use the so-called Cowling approximation where one looks only at fluid displacements and neglects metric perturbations (Cowling, 1941 after Emden, 1907). Lockitch *et al* (2001) consider the results of Ruoff *et al* (2003) unreliable due to its use. In the slow-rotation regime, however, Yoshida *et al* (2005) found what they identify as the fundamental r-mode to deviate only a few percent of the rotational frequency of the star from the modes calculated without the Cowling approximation, using the scheme introduced by Lockitch *et al* (2001). This confirmed earlier results from Provost *et al* (1981). Thus, although Finn (1988) showed that one should not use the relativistic Cowling approximation for calculating g-modes (which have low frequency and involve large fluid velocities), it appears that for r-modes, which have similar properties, frequencies can be calculated fairly accurately with this approach. Furthermore, the Cowling approximation has been shown (Yoshida & Kojima, 1998) to give accurate results (up to about 20%) for relativistic non-radial p-modes.

On the other hand, using the slow-rotation approximation may be more problematic than the Cowling approximation. It seems that when going beyond the first order in the rotation rate of the star, results may differ considerably from those obtained in first order (Beyer and Kokkotas, 1999). Therefor, it is necessary to discard the slow-rotation limit, and take into account the flattening of the star due to rotation. The presence of a continuous spectrum might well be an artifact of the slow-rotation approximation.

1.3 Methodology

The full-nonlinear time evolution of a rapidly rotating relativistic neutron star would be able to resolve most of the open questions regarding oscillations and stability. This is though a very complicated system to solve and would require too much computational time. We will therefor try to approach the problem from a simplified point of view in order to reveal some of its aspects and pave the way for forthcoming works. Perturbative methods are computationally much less expensive and linear perturbation theory has proved to describe well oscillations of small amplitude. Time-evolution has the advantage of pointing out the strongest modes excited, but mode calculation reveals also the weaker ones and

thus also the general properties of the frequency distribution. General relativity and rapid rotation are the main ingredients of this analysis, whose combination is what makes it so special, since at the starting point of this work they were never successfully applied together.

We will thus perform mode-calculation on a perturbative scheme of rapidly rotating neutron stars in general relativity. They main focus of this work will be the unstable modes, ie. the inertial modes and the fundamental pressure mode, but we will also study the general characteristics of the mode spectrum. Given the results discussed above, we expect to come against an infinite number of pressure modes with frequencies on the order of kHz and higher, and possibly an infinite number of mixed parity inertial modes, with frequencies dependent on the rotation rate of the star.

In order to get a better insight into neutron star oscillations and experience in numerically solving such problems, we will first study non-rotating stars in chapter 2. Because the problem for rapidly rotating ones is expected to be somewhat different and may demand special care, we elaborate on the numerical scheme that can be used for that case and establish an appropriate procedure in chapter 3. Eventually we deal with the oscillation mode problem for rapidly rotating neutron stars, both for axisymmetric and non-axisymmetric perturbations, in chapter 4. We end with some general remarks and the overall conclusion in chapter 5.

Chapter 2

Spherical symmetric background

In this part we initiate the mode calculation problem for neutron stars and pave the way for the inclusion of rotation. Therefor we need to perform a consistent analysis and watch for changes that may occur when switching to rotating stars. For the sake of simplicity we will use polytropic equations of state, and specifically one described by $p = 100\text{km}^2 \times \rho^2$. Such an equation of state is a good description of the background of neutron stars, regardless of rotation.

2.1 Problem set-up

For non-rotating stars, the background is spherically symmetric and can be described by the Schwarzschild metric:

$$ds^2 = -e^{2\nu}dt^2 + e^{2\lambda}dr^2 + r^2(d\theta^2 + \sin^2\theta d\phi^2),$$

where ν, and λ are functions only of the radial coordinate r; θ and ϕ are the usual spherical coordinates.

For a zero-temperature perfect fluid the energy-momentum tensor has the form

$$T_{\mu\nu} = pg_{\mu\nu} + (p + \rho)u_\mu u_\nu$$

where $p(r), \rho(r)$ are the pressure and density of the star, while $u_\mu = \{-e^\nu, 0, 0, 0\}$ is the 4-velocity of the fluid. The profile of the above variables throughout the star and thus its structure can be found by solving the Einstein equations

$$R_{\mu\nu} = 8\pi(T_{\mu\nu} - \frac{1}{2}g_{\mu\nu}T^\alpha_\alpha)$$

and the conservation of energy-momentum

$$T^{\mu}_{\nu;\mu} = 0$$

Due to the tensor symmetries and the relation between p and ρ, eventually just three equations suffice to describe the interior of the star which are known as Tolman-Oppenheimer-Volkov (TOV) equations:

$$\nu' = 4\pi r p e^{2\lambda} + \frac{e^{2\lambda} - 1}{2r} \tag{2.1}$$

$$\lambda' = 4\pi r \rho e^{2\lambda} - \frac{e^{2\lambda} - 1}{2r} \tag{2.2}$$

$$p' = -(p + \rho)\nu' \tag{2.3}$$

($' \equiv d/dr$)

On this background we assume now a perturbation of $g_{\alpha\beta}$: $h_{\alpha\beta}$. We have then the perturbed Christoffel symbols

$$\delta\Gamma^{\kappa}_{\mu\nu} = \frac{1}{2} g^{\alpha\kappa}(h_{\alpha\nu;\mu} + h_{\alpha\mu;\nu} - h_{\mu\nu;\alpha})$$

and the perturbed Ricci tensor

$$\delta R_{\mu\nu} = \delta\Gamma^{\alpha}_{\mu\nu;\alpha} - \delta\Gamma^{\alpha}_{\mu\alpha;\nu}.$$

The perturbed Einstein equations then read:

$$\delta R_{\mu\nu} = 8\pi(\delta T_{\mu\nu} - \frac{1}{2}(g_{\mu\nu}(g^{\kappa\lambda}\delta T_{\kappa\lambda} - h_{\kappa\lambda}T^{\kappa\lambda}) + h_{\mu\nu}T^{\alpha}_{\alpha})) \tag{2.4}$$

while

$$\delta T_{\mu\nu} = \delta p g_{\mu\nu} + p h_{\mu\nu} + (p + \rho)(u_\mu \delta u_\nu + u_\nu \delta u_\mu) + (\delta p + \delta\rho) u_\mu u_\nu$$

is the perturbed form of the energy momentum tensor.

$\delta\rho$ and $\delta p = C_s^2 \delta\rho$ are the density and pressure perturbations respectively while $C_s = \sqrt{\frac{dp}{d\rho}}$ is the speed of sound in the fluid; δu_μ stands for the perturbed 4-velocity, which describes the velocities of the fluid perturbations.

These three perturbed quantities of the fluid are related through the equations of motion which arise from the condition

$$\begin{aligned} \delta\left(T^{\nu}_{\mu;\nu}\right) &= g^{\kappa\nu}\left[(\delta T_{\mu\kappa})_{,\nu} - \delta\Gamma^{\rho}_{\nu\kappa}T_{\mu\rho} - \delta T_{\mu\rho}\Gamma^{\rho}_{\nu\kappa} - \Gamma^{\rho}_{\mu\nu}\delta T_{\rho\kappa} - T_{\rho\kappa}\delta\Gamma^{\rho}_{\mu\nu}\right] - h^{\kappa\nu}T_{\mu\kappa;\nu} \\ &= 0 \end{aligned} \tag{2.5}$$

All together gives us a system of equations for fluid and metric variables in the four-dimensional spacetime describing the evolution of a perturbation.

The problem can be simplified much more when the symmetry of the problem is recognized and a decomposition into spherical harmonics ($Y_{\ell m}(\theta, \phi)$) is applied. The pressure perturbation, for example, would then be expressed as $p(t, r, \theta, \phi) = p(t, r)Y_{\ell m}(\theta, \phi)$. By using the equation that the $Y_{\ell m}$'s satisfy,

$$\sin^2\theta \frac{\partial^2 Y_{lm}}{\partial^2 \theta} + \frac{\partial^2 Y_{lm}}{\partial^2 \phi} + \cos\theta \sin\theta \frac{\partial Y_{lm}}{\partial \theta} + \sin^2\theta \ell(\ell+1) Y_{lm} = 0,$$

the angular dependencies are eventually removed and the index ℓ appears in the equations. If we also assume an harmonic time dependence, $p(t, r) = p(r)e^{i\sigma t}$, we are eventually left with a one-dimensional problem to solve. We will now proceed in solving some explicit cases for non-rotating stars that have been studied before and whose results we can compare with the literature.

2.2 Radial modes

Due to the spherical symmetry, all derivatives with respect to the angular coordinates (θ, ϕ) vanish, and the general description for the metric perturbation reduces to

$$h_{\mu\nu} = \begin{pmatrix} S_1(t,r) & 0 & 0 & 0 \\ 0 & S_3(t,r) & 0 & 0 \\ 0 & 0 & T(t,r) & 0 \\ 0 & 0 & 0 & T(t,r)\sin^2\theta \end{pmatrix}$$

We have also made use here of the additional freedom of the Regge-Wheeler gauge by eliminating the t-r component of $h_{\mu\nu}$. The perturbed 4-velocity then reads:

$$\delta u_\alpha = \left(\frac{1}{2} S_1(t,r), \delta u_r, 0, 0\right)$$

The equations of motion of the fluid, with the help of the momentum constraint and an additional condition, which used up the final gauge freedom in order to eliminate the T(t,r) variable, led to a single wave-equation for one fluid variable, the fluid displacement vector $\zeta(t, r)$ ($\dot{\zeta} \sim \delta u_r$):

$$W \frac{\partial^2 \zeta}{\partial t^2} = \frac{\partial}{\partial r}(P \frac{\partial \zeta}{\partial r}) + Q\zeta \tag{2.6}$$

with
$W = (p + \rho)e^{3\lambda+\nu}/r^2$
$P = (p + \rho)e^{\lambda+3\nu}C_s^2/r^2$
$Q = (p + \rho)e^{\lambda+3\nu}(\nu'^2 + 4\frac{\nu'}{r} - 8\pi e^{2\lambda}p)/r^2$

This was turned into a set of two ordinary differential equations of first order for the variables $y_1(r) = e^{i\sigma t}\zeta(t, r)$ and $y_2(r) = P \times y_1'$. We integrate

Table 2.1: The first three radial modes computed with our code for a polytropic equation of state with ($\rho_c = 3 \times 10^{15}\mathrm{gr/cm}^3$) compared to the results of Ruoff (2001b).

Our results	Literature
2,137	2,141
6,865	6,871
10,308	10,319

them from the center of the star (initial values $y_1(\Delta x) \simeq y_{10}\Delta x^3, y_2(\Delta x) \simeq y_{20}$ with regularity condition $y_1 0 = y_{20}/(3P_0)$) until its surface. The satisfaction of the boundary condition there, $y_2(R) = 0$, reveals us the eigenfrequencies. We found a series of solutions, the first three of which are presented in table. 2.1 We notice that our results are in good agreement (within less then 1%) with the same calculations by Ruoff (2001b).

The small discrepancy is possibly due to the use of just single numerical precision; later in this work, when results get more demanding, we switch to double precision. This gives us confidence that both the numerical procedure and the integration routine have been performed properly. This was also the sole scope of this analysis since the radial modes are the most trivial and well known solutions of the eigenvalue problem. They are of no further interest, since for non-rotating stars they do not produce any gravitational wave emission, which is also the reason why the eigenvalues are purely real numbers. Only in the case of rotation these modes will couple to non-radial ones and get a complex frequency, the imaginary part of which describes the damping due to outgoing radiation.

2.3 Non Radial modes

The decomposition of the non-radial perturbations into spherical harmonics reveals two groups of variables that behave differently under rotation, the polar (even parity) and the axial (odd parity) ones. In the non rotating case they are completely decoupled and can be studied separately.

2.3.1 Axial modes

The perturbed metric in the Regge-Wheeler gauge reads:

$$h_{\mu\nu} = \begin{pmatrix} 0 & 0 & -e^{\nu-\lambda}V_1\partial_\phi Y_{lm}/\sin\theta & e^{\nu-\lambda}V_1\sin\theta\partial_\theta Y_{lm} \\ 0 & 0 & -e^{\lambda-\nu}V_2\partial_\phi Y_{lm}/\sin\theta & e^{\lambda-\nu}V_2\sin\theta\partial_\theta Y_{lm} \\ \star & \star & 0 & 0 \\ \star & \star & 0 & 0 \end{pmatrix}$$

$(V_{1,2} = V_{1,2}(t,r), \partial_\phi Y_{lm} \equiv \frac{\partial Y_{lm}}{\partial \phi}, \partial_\theta Y_{lm} \equiv \frac{\partial Y_{lm}}{\partial \theta}, \star \equiv$ symmetric part)

The corresponding velocity perturbations are

$$\delta u_\alpha = u_3(r)\,(0, 0, -\partial_\phi Y_{lm}/\sin\theta, \sin\theta \partial_\theta Y_{lm})$$

The t-t component of the perturbed Einstein equations reveals that

$$H(t,r) \equiv \frac{\delta\rho}{p+\rho} C_s^2 = 0 \tag{2.7}$$

From the equations of motion it then follows that

$$\frac{\partial u_3}{\partial t} = 0 \tag{2.8}$$

That means that the axial perturbations (in the non-rotating case) do not produce any oscillation of the fluid ($\sigma \neq 0 \Rightarrow u_3(r) = 0$). Therefore the perturbation itself would be fully described by a metric variable.

The two metric variables are related through the evolution equations

$$\frac{\partial^2 V_1}{\partial t^2} = e^{2(\nu-\lambda)} \left\{ \frac{\partial^2 V_0}{\partial t \partial r} + \left[4\pi r(p-\rho) e^{2\lambda} + \frac{e^{2\lambda}-3}{r} \right] \frac{\partial V_0}{\partial t} + e^{2\lambda} \frac{2-\ell(\ell+1)}{r^2} V_0 \right\} \tag{2.9}$$

$$\frac{\partial V_0}{\partial t} = \frac{\partial V_1}{\partial r} \tag{2.10}$$

which can be combined to a single equation for V_1:

$$\frac{\partial^2 V_1}{\partial t^2} = e^{2(\nu-\lambda)} \left\{ \frac{\partial^2 V_1}{\partial r^2} + (\nu' - \lambda' - \frac{2}{r}) \frac{\partial V_1}{\partial r} + e^{2\lambda} \frac{2-\ell(\ell+1)}{r^2} V_1 \right\} \tag{2.11}$$

(where we also made use of the TOV relations), or for $Q = \frac{V_1}{r}$:

$$\frac{\partial^2 Q}{\partial t^2} = e^{2(\nu-\lambda)} \left\{ \frac{\partial^2 Q}{\partial r^2} + (\nu' - \lambda') \frac{\partial Q}{\partial r} + \left[\frac{e^{2\lambda}[2-\ell(\ell+1)] - 2}{r^2} + \frac{(\nu'-\lambda')}{r} \right] Q \right\} \tag{2.12}$$

By introducing the tortoise coordinate $r_\star$ through $\frac{d}{dr_*} = e^{\nu-\lambda} \frac{d}{dr}$ we can additionally eliminate the first spatial derivative of Q:

$$\frac{\partial^2 Q}{\partial t^2} = \frac{\partial^2 Q}{\partial r_*^2} + e^{2\nu}[4\pi(p-\rho) + \frac{6m - r\ell(\ell+1)}{r^3}]Q, \tag{2.13}$$

where we returned to the more familiar variables (pressure, density, mass-function).

We integrate from the center of the star – initial data $Q(\Delta x) = Q_0 \Delta x^{\ell+1}$, $\frac{dQ}{dr}|_{\Delta x} = Q_0'(\ell+1)\Delta x^\ell$ – until infinity (set at $1000 \times R$) where we expect the wave to be purely outgoing, $\sim e^{-i\sigma r_\star}$. We do this by demanding the Wronskian of our variable and the exponential factor to vanish. The complex frequencies that

Table 2.2: The w-modes of a neutron star with a polytropic equation with $\rho_c = 5\times10^{16}\mathrm{gr/cm}^3$. Presented are the real and imaginary part of the frequency in kHz for the three numerical methods described in the text: (H-P) for the method of Nollert (1990), ($r_\star$) for the one of Andersson (1998) and (r) for a alternative version of the latter developed here.

(H-P)		($r_\star$)		(r)	
σ_R	σ_I	σ_R	σ_I	σ_R	σ_I
13.772	0.441	13.772	0.441	13.771	0.441
15.912	0.990	15.912	0.990	15.912	0.990
18.128	1.578	18.128	1.578	18.128	1.578
20.287	2.135	20.287	2.135	20.288	2.132

satisfy this last condition are then the eigenmodes. The problem that occurs is that, because the imaginary parts of the frequencies are positive, the wanted solution diverges exponentially towards infinity, ie. too large numbers at our boundary.

One method that avoids this problem was proposed by Nollert (1990). It uses the analytic expression of the outgoing solution (instead of just the leading order term)

$$\phi(r\to\infty) = e^{-i\sigma r}r^{-i\sigma}\left(\sum_{n=0}^{N} a_n r^{-n} + O(r^{-N-1})\right)$$

and takes the sum over an optimum number of terms dependent from the integration distance $N \approx 2|\sigma|r_N$ for which it is shown that the growth is suppressed. One has to integrate until just outside the surface of the star and then calculate the Wronskian at the preferred distance.

Another solution to this numerical problem was proposed by Andersson (1998), who suggested integrating along a line at the complex $r_\star$ plane for which $arg(r_\star) = -arg(\sigma)$. By excluding an in-going wave from infinity ($e^{+i\sigma r_\star}$) the outgoing solution should go like $e^{-i\sigma r_\star}$. The exponent of that term has then a zero imaginary part and therefor it does not grow. One has then to integrate many wavelengths ($2\pi/|\sigma|$) outside the star, in order to get rid of the unwanted solution (with the plus sign on the exponent). For an optimal accuracy even a 1000-wavelength distance is necessary.

We applied both methods to a dense – $\rho_c = 5\times10^{16}\mathrm{gr/cm}^3$, $R = 4.99$km, $M = 1.52$km – polytropic model; we also used an alternative of the second method, by integrating along a complex r coordinate (instead of $r_\star$) which runs faster. The results are presented in table 2.3.1 and are in good agreement with each other.

The same, though, procedure for a less dense model – $\rho_c = 3\times10^{15}\mathrm{gr/cm}^3$, $R = 8.86$ km, $M = 1.87$km– revealed the divergence of $r_\star$ from r for less compact models (table 2.3.1). These apparently do not favor the use of a complex r path

Table 2.3: The same as in table 2.3.1 but for a less dense model with $\rho_c = 3 \times 10^{15}\mathrm{gr/cm}^3$

(H-P)		($r_\star$)		(r)	
σ_R	σ_I	σ_R	σ_I	σ_R	σ_I
5.601	14.692	5.601	14.692	5.408	9.000
10.501	5.390	10.501	5.390	10.501	5.391
				10.897	10.003
				14.849	9.917
17.993	8.521	17.993	8.521	17.867	8.384
				19.796	9.814
				23.706	10.031
26.840	10.225	26.840	10.225	26.697	9.411

for the integration method and one should then perform it along the complex $r_\star$ path. This may not surprise us since for a Schwarzschild geometry the tortoise coordinate outside the star can be given as function of the r coordinate through

$$r_\star = r + 2M \log\Big(\frac{r}{2M} - 1\Big).$$

Thus $\frac{r_\star}{r}$ gets closer to 1 for increasing M/r (in the range that we consider) making then their difference less significant. Besides, for very dense (constant density) models one could in principle also integrate along the real r axis and find quite accurate results (Kokkotas, 1994).

The axial modes can thus be well solved with our code so that we can proceed in dealing with the polar modes. For non-rotating stars the axial modes consist just of the w-modes which are highly damped and only weak sources of gravitational waves since they do not couple to matter oscillations. For rotating stars the axial modes will include also fluid oscillations gaining again our attention.

Apart from successfully applying these new numerical procedures and handling the more demanding integration outside the star, we also experienced how much a slight modification in the analysis can influence the results, by introducing additional (unphysical) modes.

2.3.2 Polar modes

The perturbed metric in the Regge-Wheeler gauge reads:

$$h_{\mu\nu} = \begin{pmatrix} e^{2\nu}(rS + F/r)Y_{lm} & e^{2\lambda}H_1 Y_{lm} & 0 & 0 \\ e^{2\lambda}H_1 Y_{lm} & e^{2\lambda}(rS + F/r)Y_{lm} & 0 & 0 \\ 0 & 0 & rFY_{lm} & 0 \\ 0 & 0 & 0 & r\sin^2\theta FY_{lm} \end{pmatrix}$$

With the perturbed 4-velocity

$$\delta u_\alpha = -\frac{e^\nu}{r}\left(\frac{1}{2}(r^2S+F)Y_{lm}, (u_1-\frac{u_2}{r})Y_{lm}, u_2\partial_\theta Y_{lm}, u_2\partial_\phi Y_{lm}\right) \qquad (2.14)$$

and the fluid variable $\delta p = \frac{H(p+\rho)}{r}Y_{lm}$, the perturbed field equations give two coupled wave equations for S,F:

$$\begin{aligned}\frac{\partial^2 S}{\partial t^2} &= e^{2(\nu-\lambda)}\left\{\frac{\partial^2 S}{\partial r^2}+\left[4\nu'^2+\frac{5\nu'+3\lambda'}{r}-2\frac{e^{2\lambda}-1}{r^2}-e^{2\lambda}\frac{\ell(\ell+1)}{r^2}\right]S\right.\\ &\left.+(5\nu'-\lambda')\frac{\partial S}{\partial r}+\frac{4}{r^4}\left(r^2\nu'^2+r\lambda'+1-e^{2\lambda}\right)F\right\} \qquad (2.15)\end{aligned}$$

$$\begin{aligned}\frac{\partial^2 F}{\partial t^2} &= e^{2(\nu-\lambda)}\left\{\frac{\partial^2 F}{\partial r^2}+\frac{1}{r^2}\left[r(3\lambda'+\nu')+2\left(e^{2\lambda}-1\right)-e^{2\lambda}\ell(\ell+1)\right]F\right.\\ &\left.+(\nu'-\lambda')\frac{\partial F}{\partial r}+2[r(\nu'+\lambda')-1]S+\frac{2}{r}(\nu'+\lambda')\left(\frac{1}{C_s^2}-1\right)H\right\} \qquad (2.16)\end{aligned}$$

as well as the Hamiltonian constraint:

$$\begin{aligned}\frac{2(\nu'+\lambda')}{rC_s^2}H = &-\frac{\partial^2 F}{\partial r^2}+\lambda'\frac{\partial F}{\partial r}+r\frac{\partial S}{\partial r}+\left(2-2r\lambda'+\frac{1}{2}e^{2\lambda}\ell(\ell+1)\right)S\\ &+\frac{1}{r^2}\left(e^{2\lambda}[\ell(\ell+1)-1]+1-3r\lambda'\right)F \qquad (2.17)\end{aligned}$$

We additionally get the fluid equations of motion:

$$\begin{aligned}\frac{\partial H}{\partial t} &= e^{2(\nu-\lambda)}\left\{\left[C_s^2(2\nu'-\lambda'+\frac{1}{r})-\nu'\right]u_1+C_s^2\left(\frac{\partial u_1}{\partial r}-\frac{1}{r}\frac{\partial u_2}{\partial r}\right)\right.\\ &\left.+\frac{1}{r^2}\left[C_s^2(r\lambda'-2r\nu'-e^{2\lambda}\ell(\ell+1))+r\nu'\right]u_2\right\}\\ &+[C_s^2(r\lambda'+2)-r\nu']H_1+rC_s^2\frac{\partial H_1}{\partial r}-\frac{C_s^2}{2}\left(r^2\frac{\partial S}{\partial t}+3\frac{\partial F}{\partial t}\right) \qquad (2.18)\\ \frac{\partial u_1}{\partial t} &= \frac{\partial H}{\partial r}-\frac{1}{2}\left(r^2\frac{\partial S}{\partial r}+2rS+\frac{\partial F}{\partial r}\right) \qquad (2.19)\\ \frac{\partial u_2}{\partial t} &= H-\frac{1}{2}(r^2S+F) \qquad (2.20)\end{aligned}$$

The above equations[1], with the help of the perturbed field equations, can be combined to a single wave equation for H:

$$\begin{aligned}\frac{\partial^2 H}{\partial t^2} &= e^{2(\nu-\lambda)}\left\{C_s^2\frac{\partial^2 H}{\partial r^2}+[C_s^2(2\nu'-\lambda')-\nu']\frac{\partial H}{\partial r}+\nu'\frac{C_s^2-1}{2}\left(r^2\frac{\partial S}{\partial r}-\frac{\partial F}{\partial r}\right)\right.\\ &+\frac{1}{r^2}[C_s^2(r\nu'+4r\lambda'-e^{2\lambda}\ell(\ell+1))+r(2\nu'+\lambda')]H\\ &\left.+\left[\frac{C_s^2}{r^2}(\frac{7}{2}r\nu'+r\lambda'-e^{2\lambda}+1)-\frac{\nu'}{r}(2r\nu'+\frac{1}{2})\right](r^2S+F)\right\} \qquad (2.21)\end{aligned}$$

[1]Ruoff (2001) dealt with the same problem with the corresponding equation of eq. 2.18 being their eq. 54a which is however not the same due a type-fault there.

Cowling approximation This is a good point to make use of the so-called Cowling approximation. We can try solving the above problem by neglecting the metric variables and deal just with the fluid variable. So by setting S and F to zero, the equations of motion become

$$\begin{aligned}\frac{\partial H}{\partial t} &= e^{2(\nu-\lambda)}\left\{\left[C_s^2\left(2\nu'-\lambda'+\frac{1}{r}\right)-\nu'\right]u_1+C_s^2\left(\frac{\partial u_1}{\partial r}-\frac{1}{r}\frac{\partial u_2}{\partial r}\right)\right.\\ &\left.+\left[C_s^2\left(\frac{\lambda'-2\nu'}{r}-\frac{e^{2\lambda}\ell(\ell+1)}{r^2}\right)+\frac{\nu'}{r}\right]u_2\right\} \qquad (2.22)\end{aligned}$$

$$\frac{\partial u_1}{\partial t}=\frac{\partial H}{\partial r} \qquad (2.23)$$

$$\frac{\partial u_2}{\partial t}=H \qquad (2.24)$$

which can than easily be reduced to a single equation for H:

$$\begin{aligned}\frac{\partial^2 H}{\partial t^2} &= e^{2(\nu-\lambda)}\left\{C_s^2\frac{\partial^2 H}{\partial r^2}+[C_s^2(2\nu'-\lambda')-\nu']\frac{\partial H}{\partial r}\right.\\ &\left.+\frac{1}{r^2}[C_s^2(r\lambda'-2r\nu'-e^{2\lambda}\ell(\ell+1))+r\nu']H\right\} \qquad (2.25)\end{aligned}$$

The odd thing is that this is somewhat different than what we get if we neglect the metric variables at the final wave equation for H (Eq. 2.21):

$$\begin{aligned}\frac{\partial^2 H}{\partial t^2} &= e^{2(\nu-\lambda)}\left\{C_s^2\frac{\partial^2 H}{\partial r^2}+[C_s^2(2\nu'-\lambda')-\nu']\frac{\partial H}{\partial r}\right.\\ &\left.+\frac{1}{r^2}[C_s^2(r\nu'+4r\lambda'-e^{2\lambda}\ell(\ell+1))+r(2\nu'+\lambda')]H\right\} \qquad (2.26)\end{aligned}$$

If we try to derive modes from this last equation, with the standard procedure of the time-independent analysis, we also get different numbers than from Eq. 2.25 directly (table 2.3.2).

The ones from eq. 2.25 appear actually to be more accurate ones, but the question that arises is whether this is the right thing to do, since there seems then to be an inconsistency in the field equations (fluid variables=metric variables$\equiv$ 0). Still, no relativistic star can sustain oscillations of its fluid without distortions of its background spacetime and the degree of approximation depends on how strong the neglected and used variables are related to each other. This is also possibly the reason why the f-mode appears more inaccurate: since it describes motion larger towards the surface, it couples with the spacetime more then the 'internal' p-modes do.

Concentrating on the results of the standard Cowling approximation, we notice that the accuracy of the results (compared with those of the full system)

Table 2.4: The first 5 pressure modes for the model of table2.3.1 solved by neglecting the metric perturbation in the beginning and the end of the analysis, as well as for the full problem (from table 2.3.2).

Modes (KHz)	Cowling approx.	late Cowling ap.	full case
f-mode	3.297	2.463	2.869
1st p-mode	7.257	6.497	6.548
2nd p-mode	10.613	9.973	9.982
3rd p-mode	13.803	13.265	13.266
4th p-mode	16.927	16.467	16.465

and thus also of the approximation itself, gets better as the order of the modes increases. The reason for that is the same as the one stated above. It is thus save to use this approximation for higher order modes but for f-modes, for example, one has to accept an error of almost 15%. The big advantage though is that it is much more easy to handle than the full case, while still giving the overall picture and the distribution of the modes.

Still, for the case of non-rotating neutron stars that we are studying here, the polar case can be fully solved in a similar way to the axial case, without the use of the Cowling approximation; the difference is that the equations involve now three variables inside the star (the fluid one and the two metric ones) and two outside of it (the – dependent from each other – metric ones).

With Taylor expansion at the center one first finds the r-dependence of the three variables there:

$$h = h_0 r^\ell,\ s = s_0 r^{\ell+1},\ f = f_0 r^{\ell+1}$$

Their amplitudes (h_0, s_0, f_0) represent the three degrees of freedom that the problem has. One has then to make use of two of them in order to leave the last one for the determination of the eigenfrequency. This happens with a regularity condition at the center and a junction condition at the surface. We are looking thus for the right combination of starting values (amplitudes) that satisfy the junction condition at the surface (vanishing of the Lagrangian pressure perturbation). We achieve this by integrating twice till the surface for a linearly independent set of starting values (eg. 2,3,5) and find the linear combination of them (and also the corresponding values at the surface) that give $\Delta p = 0$ (which in practise gives the same equation as 2.21 with $C_s^2 = 0$). One can do that for all three variables and defining the starting value of one as function of the other two or integrate a (complete) set of equations for only two variables).

The integration of the two metric variables outside of the star along a complex $r_\star$ path and demanding (any)one of them to resemble an outgoing wave reveals the modes. We quantify this condition by looking for the zeroes of the Wronskian between S and $e^{-i\sigma r_\star}$ on the two-dimensional complex frequency plane. In practise we calculate the absolute value of the above quantity

Table 2.5: The two group of modes for polar perturbations for the polytropic model with $\rho_c = 3 \times 10^{15} \mathrm{gr/cm}^3$. Listed are the real and imaginary parts of the frequencies for fluid and wave modes, as computed by Leins (1994), to which our search agreed up to the limitations of our code. For transforming the frequencies of the w-modes from geometrical units into Hz one needs to multiply with 3×10^5 (see appendix A).

Fluid modes (Hz)		Wave modes (km^{-1})	
σ_R	σ_I	σ_R	σ_I
2869.4	1.4689	0.269	0.141
6548.6	0.2578	0.468	0.198
9982.1	0.0007	0.655	0.227

$(S' + i\sigma S/(1 - 2M/r_\infty)$, where r_∞ is our outer boundary) and look for its minima. Since by this we can only restrict the solutions to a narrow range rather than calculate them, we perform our search by plotting the above quantity and compare with results from the literature. We were interested in identifying the modes and ceased increasing resolution after the accuracy approached the limitations of our code (of the order of 1%). Some of the modes identified are shown in table 2.3.2 and the contour plot of an initial resolution covering that modes is given in figure 2.1. We note the w-modes have much higher frequencies (the first w-mode has 12,843 Hz), but also a comparably high imaginary part (in contrast to the pressure modes).

By these we are confident of reproducing the results of the literature even when taking the metric perturbations into account and also developed a code to perform this more complicated numerical work. Furthermore, we successfully dealt with a system of coupled equations and gained an inside of how changes/errors in some terms can effect the results. The modes calculated are by themselves a good reference, since they are not expected to change much under rotation.

Figure 2.1: The contour plot of the w-modes presented in table 2.3.2 The x and y axis give the real and imaginary part of the frequency in geometrical units while the z axis shows the absolute value of the Wronskian between a metric perturbation and the expression for the outgoing wave ($e^{-i\sigma r_\star}$) in arbitrary units. At the lower plot, the contour of the Wronskian together with the results of Leins (1994) are shown.

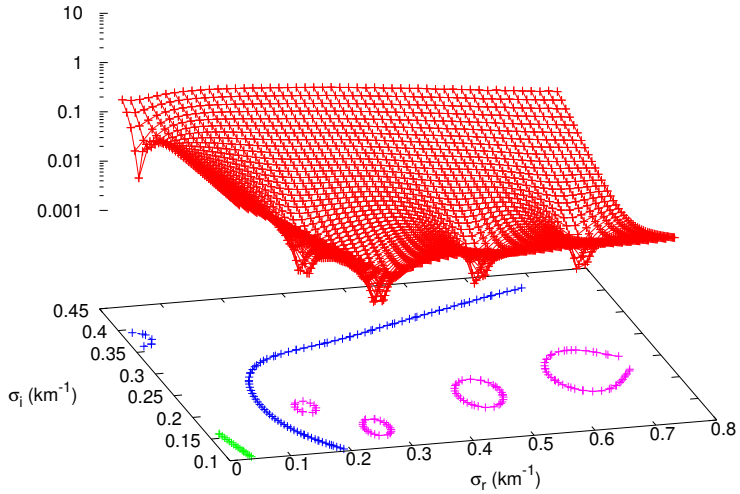

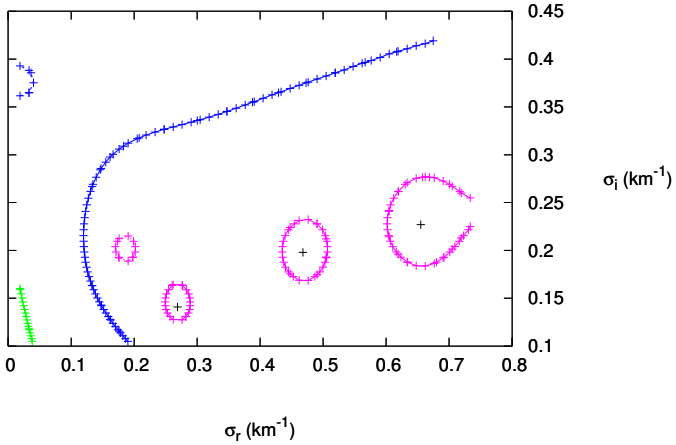

Chapter 3

Going from spherical symmetry to axisymmetry

3.1 The spherical background in two dimensions

After solving the one-dimensional problem and before moving to rotating stars, where flattening will break the spherical symmetry, we need to test whether the methods applied sofar will work also on a two-dimensional grid. To do this we will examine the same problem of a non-rotating star, by ignoring though the spherical symmetry and assuming that the variables are functions of both r and θ. If the analysis could be also applied straightforward in that case, then the whole procedure has good chances of applying also on a non-spherically symmetric background.

Let thus be

$$ds^2 = -e^{2\nu(r,\theta)}dt^2 + e^{2\lambda(r,\theta)}dr^2 + r^2(d\theta^2 + \sin^2\theta d\phi^2)$$

From the conservation of the energy-momentum tensor, $T^{\mu}_{\nu;\mu} = 0$, we get the Tolman-Oppenheimer-Volkoff equations (Oppenheimer & Volkoff, 1939; Tolman, 1939) for the background quantities:

$$0 = \frac{\partial^2\lambda}{\partial\theta^2} + \left(\frac{\partial\lambda}{\partial\theta}\right)^2 - 2re^{-2\lambda}\frac{\partial\lambda}{\partial r} + \frac{\cos\theta}{\sin\theta}\frac{\partial\lambda}{\partial\theta} + e^{-2\lambda} - 1 + 8\pi r^2\rho \tag{3.1}$$

$$0 = \frac{\partial^2\nu}{\partial\theta^2} + \left(\frac{\partial\nu}{\partial\theta}\right)^2 + 2re^{-2\lambda}\frac{\partial\nu}{\partial r} + \frac{\cos\theta}{\sin\theta}\frac{\partial\nu}{\partial\theta} + e^{-2\lambda} - 1 - 8\pi r^2 p \tag{3.2}$$

$$0 = r\left(\frac{\partial\lambda}{\partial r} - \frac{\partial\nu}{\partial r}\right) - r^2\left[\frac{\partial^2\nu}{\partial r^2} + \left(\frac{\partial\nu}{\partial r}\right)^2 - \frac{\partial\nu}{\partial r}\frac{\partial\lambda}{\partial r}\right] - e^{2\lambda}\frac{\partial\nu}{\partial\theta}\frac{\partial\lambda}{\partial\theta} - e^{2\lambda}\frac{\cos\theta}{\sin\theta}\left(\frac{\partial\nu}{\partial\theta} + \frac{\partial\lambda}{\partial\theta}\right) + 8\pi r^2 e^{2\lambda}p \tag{3.3}$$

$$0 = r\left(\frac{\partial\lambda}{\partial r} - \frac{\partial\nu}{\partial r}\right) - r^2\left[\frac{\partial^2\nu}{\partial r^2} + \left(\frac{\partial\nu}{\partial r}\right)^2 - \frac{\partial\nu}{\partial r}\,\frac{\partial\lambda}{\partial r}\right] - e^{2\lambda}\frac{\partial\nu}{\partial\theta}\,\frac{\partial\lambda}{\partial\theta} -$$
$$e^{2\lambda}\left[\frac{\partial^2\nu}{\partial\theta^2} + \left(\frac{\partial\nu}{\partial\theta}\right)^2 + \frac{\partial^2\lambda}{\partial\theta^2} + \left(\frac{\partial\lambda}{\partial\theta}\right)^2\right] + 8\pi r^2 e^{2\lambda}p \qquad (3.4)$$

$$\frac{\partial p}{\partial r} = -(p+\rho)\frac{\partial\nu}{\partial r} \qquad (3.5)$$

$$\frac{\partial p}{\partial\theta} = -(p+\rho)\frac{\partial\nu}{\partial\theta} \qquad (3.6)$$

$$\frac{\partial\rho}{\partial r} = \frac{\partial p}{\partial r}/C_s^2 \qquad (3.7)$$

$$\frac{\partial\rho}{\partial\theta} = \frac{\partial p}{\partial\theta}/C_s^2 \qquad (3.8)$$

Instead of decomposing the perturbed variables into spherical harmonics, we assume axisymmetry and let the angular dependence be absorbed by the perturbed quantities. By using, thus, the fluid variable

$$\delta p(t,r,\theta,\phi) = H(t,r,\theta)(p+\rho)e^{im\phi}$$

and the perturbed 4-velocity [1]

$$\delta u_\alpha = \{0, -\frac{e^{2\nu}}{r}\frac{u_1-u_2}{r}, -\frac{e^{2\nu}}{r}\frac{\partial u_2}{\partial\theta} - i\,m\frac{u_3}{\sin\theta}, -\frac{e^{2\nu}}{r}i\,m\,u_2 + \sin\theta\frac{\partial u_3}{\partial\theta}\}e^{i\,m\phi},$$

we get from the equations of motion the perturbation equations for a stationary spacetime:

$$\delta T^\mu_{\phi;\mu} = 0 \quad\Rightarrow\quad \frac{\partial u_2}{\partial t} = -\frac{I}{e^\nu m}\left(\frac{\partial^2 u_3}{\partial t\partial\theta}r\sin\theta + Ime^\nu H\right) \qquad (3.9)$$

$$\delta T^\mu_{r;\mu} = 0 \quad\Rightarrow\quad \frac{\partial u_1}{\partial t} = -\frac{H}{r} + \frac{\partial H}{\partial r} + \frac{1}{r}\frac{\partial u_2}{\partial t} \qquad (3.10)$$

$$\delta T^\mu_{\theta;\mu} = 0 \quad\Rightarrow\quad \frac{\partial u_3}{\partial t} = -\frac{e^\nu\sin\theta}{Imr}\left(\frac{\partial H}{\partial\theta} - \frac{\partial^2 u_2}{\partial\theta\partial t}\right) \qquad (3.11)$$

$$\begin{aligned}\delta T^\mu_{t;\mu} = 0 \quad\Rightarrow\quad \frac{\partial H}{\partial t} &= \frac{e^{2\nu-2\lambda}}{r^2}\left\{C_s^2\left[(\lambda'-2\nu')r^2 - r\right] + r^2\nu'\right\}u_1 \\ &+\frac{e^{2\nu-2\lambda}}{r^2\sin\theta}\left[rC_s^2\sin^2\theta\lambda' + r\sin^2\theta\nu'(1-2C_s^2) - m^2e^{2\lambda}C_s^2\right]u_2 \\ &+\frac{e^\nu Im}{r}\sin\theta\left[\frac{\partial\nu}{\partial\theta}(C_s^2-1) + C_s^2\frac{\partial\lambda}{\partial\theta}\right]u_3 \\ &-\frac{e^{2\nu}}{r^2\sin^2\theta}\left[-\sin^2\theta C_s^2\frac{\partial\lambda}{\partial\theta} + \sin^2\theta\frac{\partial\nu}{\partial\theta} - 2C_s^2\sin^2\theta\frac{\partial\nu}{\partial\theta} - \cos\theta\sin\theta C_s^2\right]\frac{\partial u_2}{\partial\theta} \\ &-\frac{e^{2\nu-2\lambda}}{r}C_s^2\frac{\partial u_2}{\partial r} + \frac{e^{2\nu-2\lambda}}{r}C_s^2\frac{\partial u_1}{\partial r} + \frac{e^{2\nu}}{r^2}C_s^2\frac{\partial^2 u_2}{\partial\theta^2}, \end{aligned} \qquad (3.12)$$

[1] u_1, u_2 describe the polar perturbations of the 4-velocity, u_3 the axial ones.

and after assuming an harmonic time dependency, $e^{i\omega t}$:

$$
\begin{aligned}
i\omega u_2 &= H + A\,\frac{\partial u_3}{\partial \theta} && (3.13)\\
i\omega u_1 &= -\frac{H}{r} + \frac{\partial H}{\partial r} + i\omega\frac{u_2}{r} \quad = \frac{\partial H}{\partial r} + B\,\frac{\partial u_3}{\partial \theta} && (3.14)\\
i\omega u_3 &= C(\frac{\partial H}{\partial \theta} - i\omega\frac{\partial u_2}{\partial \theta}) = D\left[\left(\cos\theta - \sin\theta\frac{\partial \nu}{\partial \theta}\right)\frac{\partial u_3}{\partial \theta} + \sin\theta\frac{\partial^2 u_3}{\partial \theta^2}\right] && (3.15)\\
i\omega H &= E\,u_1 + F\,u_2 + G\,\frac{\partial u_1}{\partial r} + J\,u_3 + K\,\frac{\partial u_2}{\partial \theta} + L\,\frac{\partial^2 u_2}{\partial \theta^2}, && (3.16)
\end{aligned}
$$

where A-G,J-L are the corresponding functions of the background quantities (ν, λ), the speed of sound (C_s^2) (which are by themselves functions of r, θ), while the index m appears as a free parameter (instead of ℓ). In the right hand sides of eqs. 3.14 and 3.15, u_2 is already eliminated by means of eq. 3.13. The fact that $u_1 = \frac{\partial u_2}{\partial r}$ has been used in the derivation of eq. 3.16. One can also eliminate u_1 and u_2 in eq. 3.16 after taking the derivative over time and get schematically

$$
\begin{aligned}
-\omega^2 H &= a\,H + b\,\frac{\partial H}{\partial r} + c\,\frac{\partial^2 H}{\partial r^2} + d\,\frac{\partial^2 H}{\partial \theta^2} + e\,\frac{\partial H}{\partial \theta}\\
&\quad + f\,u_3 + g\,\frac{\partial u_3}{\partial \theta} + h\,\frac{\partial^2 u_3}{\partial \theta^2} + j\,\frac{\partial^3 u_3}{\partial \theta^3} && (3.17)
\end{aligned}
$$

(a-j again functions of the background quantities) which together with eq. 3.15 form a set of two partial differential equations for two unknown functions H, u_3. Interestingly, eq.3.15 can be written as a set of two ordinary differential equations for two variables $(u_3, \frac{\partial u_3}{\partial \theta})$ and can so be used to integrate u_3 on a known background grid and then one can use the computed values for the integration of H through the elliptic [2] partial differential equation 3.17 through an iterative method. In the general case though, H, u_1 as well as u_2, u_3 or also the metric perturbations, might not easily be separated. One would then have to integrate a coupled system of partial differential equations (as is also necessary for the background quantities).

3.2 Numerical solution

The standard procedure to numerically solve differential equations inside a region is to replace them by difference equations. For second order equations this has the form:

$$
\begin{aligned}
f'(x_i) &= \frac{f_{i+1} - f_{i-1}}{2h} + O(h^2) && (3.18)\\
f''(x_i) &= \frac{f_{i+1} - 2f_i + fi - 1}{h^2} + O(h^2) && (3.19)
\end{aligned}
$$

[2] Criterion $c \times d = e^{4\nu - 2\lambda}\frac{C_s^2}{r^2}C_s^2 > 0$.

for central differences. If we apply this to the fluid variable H, for both its dependencies (r, θ), and substitute in eq. 3.17 - with the u_3 terms eliminated-,

$$\frac{\partial^2 H}{\partial r^2} + \tilde{d}\,\frac{\partial^2 H}{\partial \theta^2} + \tilde{b}\,\frac{\partial H}{\partial r} + \tilde{e}\,\frac{\partial H}{\partial \theta} + (\tilde{a} - \tilde{\omega}^2)\,H = 0, \tag{3.20}$$

where

$$\begin{aligned}
\tilde{d} \equiv \frac{d}{c} &= \frac{e^{2\lambda}}{r^2} \\
\tilde{b} \equiv \frac{b}{c} &= 2\frac{\partial \nu}{\partial r} - \frac{\partial \lambda}{\partial r} - \frac{1}{C_s^2}\frac{\partial \nu}{\partial r} \\
\tilde{e} \equiv \frac{e}{c} &= \frac{e^{2\lambda}}{r^2}\left(2\frac{\partial \nu}{\partial \theta} + \frac{\partial \lambda}{\partial \theta} + \frac{\cos\theta}{\sin\theta} - \frac{1}{C_s^2}\frac{\partial \nu}{\partial \theta}\right) \\
\tilde{a} - \tilde{\omega}^2 \equiv \frac{a - \omega^2}{c} &= -\frac{2}{r}\frac{\partial \nu}{\partial r} + \frac{1}{r}\frac{\partial \lambda}{\partial r} - \frac{m^2 e^{2\lambda}}{r^2 \sin^2\theta} + \frac{1}{C_s^2 r}\frac{\partial \nu}{\partial r} - \frac{e^{2\lambda - 2\nu}\omega^2}{C_s^2},
\end{aligned}$$

we get the relationship:

$$\begin{aligned}
H(r_{j+1}, \theta_i) \equiv H_i^{j+1} &= \frac{2 + 2\tilde{d}\frac{\Delta r^2}{\Delta \theta^2} + (\tilde{\omega}^2 - \tilde{a})\Delta r^2}{1 + \frac{\tilde{b}\Delta r}{2}} H_i^j - \frac{1 - \tilde{b}\Delta r/2}{1 + \tilde{b}\Delta r/2} H_i^{j-1} \\
&\quad - \frac{\tilde{e}\frac{\Delta r^2}{2\Delta \theta} + \tilde{d}\frac{\Delta r^2}{\Delta \theta^2}}{1 + \tilde{b}\Delta r/2}\left(H_{i+1}^j + H_{i-1}^j\right) \\
&\equiv k\,H_i^j - \ell\,H_i^{j-1} - m\,\left(H_{i+1}^j + H_{i-1}^j\right)
\end{aligned} \tag{3.21}$$

One can now attack the problem as a boundary value problem, by taking the difference equations of all the grid-lines (including the boundary ones where the appropriate conditions are imposed) and solve them simultaneously in a (degenerate) matrix form, or integrate the first grid-line outwards through the above relationship as an initial value problem. The last one ('shooting method') is though of questioned stability and convergence. Whether it is stable or not can be checked if we assume an error at $j = 0$ of the form

$$e_i^0 = e^{I\beta i \Delta\theta}$$

and expect it to grow at the j-th row as

$$e_i^j = e^{\alpha j \Delta r} e^{I\beta i \Delta\theta}$$

By inserting this into eq. 3.21, the relationship that results is the quadratic

$$\left(e^{\alpha\Delta r}\right)^2 + (2m\cos\beta\Delta\theta - k)e^{\alpha\Delta r} + \ell = 0 \tag{3.22}$$

The product of the two solutions of this equation equals

$$e_{1,2}^{\alpha\Delta r} = \ell > 1 \tag{3.23}$$

($\tilde{b} < 0$),which means that there exists at least one solution that grows outwards (for increasing r), *unless* the discriminant of eq. 3.22 is non-positive. This condition leads to

$$\begin{aligned} -2 \leq & \quad 2m\cos\beta\Delta\theta - k \quad \leq 2 \Rightarrow \\ -2 \leq & \quad \frac{\left[2\tilde{d}(\cos\beta\Delta\theta - 1) + 2\tilde{e}\right]\frac{\Delta r^2}{\Delta\theta^2} - 2 + (\tilde{\omega}^2 - \tilde{a})\Delta r^2}{1 + \tilde{b}\Delta r/2} \quad \leq 2 \end{aligned} \tag{3.24}$$

For $1 + \tilde{b}\Delta r/2 \simeq 1$ (till close to the surface..) and $\Delta r^2 \times \Delta\theta^2 \ll 1$ we get

$$0 \leq 2\left[\tilde{d}(\cos\beta\Delta\theta - 1) + \tilde{e}\right]\Delta r^2 \leq 4\Delta\theta^2 \tag{3.25}$$

which, since actually $\tilde{e} \sim \frac{\cos\theta}{\sin\theta}$, is not everywhere fulfilled.

In contrast to the previous method - the explicit one - on can also use an implicit scheme. The θ-derivatives will not be given by central differences at $\{i, j\}$, eqs. 3.18, 3.19, but through the average of two, one located at $\{j+1, i\}$ and one at $\{j-1, i\}$. So, our integration scheme, in analogy to eq. 3.21, will look like

$$\begin{aligned} &\left[\frac{\tilde{e}}{4\Delta\theta} + \frac{\tilde{d}}{2\Delta\theta^2}\right]\left(H_{i+1}^{j+1} + H_{i-1}^{j+1}\right) + H_i^{j+1}\left[\frac{1}{\Delta r^2} + \frac{\tilde{b}}{2\Delta r} - \frac{\tilde{d}}{\Delta\theta^2}\right] = \\ &\qquad\qquad H_i^j\left[\frac{2}{\Delta r^2} + \tilde{\omega}^2 - \tilde{a}\right] \\ &+H_i^{j-1}\left[\frac{\tilde{b}}{2\Delta r} - \frac{1}{\Delta r^2} + \frac{\tilde{d}}{\Delta\theta^2}\right] - \left[\frac{\tilde{e}}{4\Delta\theta^2} + \frac{\tilde{d}}{2\Delta\theta}\right]\left(H_{i+1}^{j-1} + H_{i-1}^{j-1}\right) \end{aligned} \tag{3.26}$$

where now we have three unknowns ($\{j+1\}$-row elements) per equation, so we have to solve a complete set of equations for the $\{j+1\}$-row.

If we imply the same stability criterion as before we get, in analogy to eq. 3.22, the following quadratic equation for the error at the j-th row

$$\begin{aligned} 0 = &\left[\left(\frac{\tilde{e}}{4\Delta\theta} + \frac{\tilde{d}}{2\Delta\theta^2}\right)\left(e^{I\beta\Delta\theta} + e^{-I\beta\Delta\theta}\right) + \frac{1}{\Delta r^2} + \frac{\tilde{b}}{2\Delta r} - \frac{\tilde{d}}{\Delta\theta^2}\right]\left(e^{\alpha\Delta r}\right)^2 \\ &\qquad - \left[\frac{2}{\Delta r^2} + \tilde{\omega}^2 - \tilde{a}\right]\left(e^{\alpha\Delta r}\right) \\ &+\left[\left(\frac{\tilde{e}}{4\Delta\theta} + \frac{\tilde{d}}{2\Delta\theta^2}\right)\left(e^{I\beta\Delta\theta} + e^{-I\beta\Delta\theta}\right) + \frac{1}{\Delta r^2} - \frac{\tilde{b}}{2\Delta r} - \frac{\tilde{d}}{\Delta\theta^2}\right] \end{aligned} \tag{3.27}$$

The product of the two solutions of eq. 3.27 equals

$$\begin{aligned} e_{1,2}^{\alpha\Delta r} &= \frac{\left(\frac{\tilde{e}}{2\Delta\theta} + \frac{\tilde{d}}{\Delta\theta^2}\right)\cos\beta\Delta\theta - \frac{\tilde{d}}{\Delta\theta^2} + \frac{1}{\Delta r^2} - \frac{\tilde{b}}{2\Delta r}}{\left(\frac{\tilde{e}}{2\Delta\theta} + \frac{\tilde{d}}{\Delta\theta^2}\right)\cos\beta\Delta\theta - \frac{\tilde{d}}{\Delta\theta^2} + \frac{1}{\Delta r^2} + \frac{\tilde{b}}{2\Delta r}} \\ &= 1 - \frac{\tilde{b}/\Delta r}{\left(\frac{\tilde{e}}{2\Delta\theta} + \frac{\tilde{d}}{\Delta\theta^2}\right)\cos\beta\Delta\theta - \frac{\tilde{d}}{\Delta\theta^2} + \frac{1}{\Delta\theta^2} + \frac{\tilde{b}}{2\Delta r}} \end{aligned} \tag{3.28}$$

and in order to have a stable integration this has to be smaller then 1; since $\tilde{b} < 0$, the wanted condition, under the same approximations as in the explicit method, is

$$1 < \frac{\Delta r^2}{\Delta \theta^2} \tilde{d}(1 - \cos \beta \Delta \theta) \tag{3.29}$$

This condition, however, is very sensitive on the stepsizes and cannot guarantee the stability of the numerical scheme. Since we need to develop a method that will work for arbitrary resolution, we consider some alternative ideas. The nature of the (eigenvalue) problem suggests solving the whole system of equations simultaneously on a fixed grid. On of these methods is the so-called QR-algorithm

3.3 The QR-algorithm

The Cowling approximation in stellar oscillations is a special case, not only because it describes well the full case but also because it is a well defined Sturm-Liouville problem. When the boundary conditions are implied the system of equations to be solved form an eigenvalue problem. That is then much easier solved as there are specific routines dealing with such cases. The QR-algorithm is an alternative of the power method, for systems with degenerate eigenvalues or where all the eigenvalues are required.

3.3.1 Numerical procedure

We briefly describe the numerical method used in this work. We discretize the system of equations at every grid point, including the boundaries by making use of the boundary conditions. This results in a system of linear equations of the form

$$\mathbf{A} \cdot X = 0 \tag{3.30}$$

where the unknowns X are the discrete perturbation quantities at all grid points, and the coefficient matrix $\mathbf{A}$ represents the equations resulting from the perturbation equations at all grid points and from the boundary conditions. $\mathbf{A}$ is a highly sparse matrix. The components of $\mathbf{A}$ depend on the frequency parameter σ. It is now possible to examine the condition of $\mathbf{A}$, searching for values of σ which make $\mathbf{A}$ degenerate, since this is the only way that Eq. (3.30) allows non-trivial solutions for the perturbation quantities.

In the cases we study here, we may rewrite eq. 3.30 as an eigenvalue problem of the form

$$\tilde{\mathbf{A}} \cdot X = i\sigma X \tag{3.31}$$

Note that this is a special case and not generally possible; it will probably not work for the general perturbation equations which result if one does not use the Cowling approximation.

We may now use a standard routine for finding eigenvalues of eq. 3.31. We use the routine `cg.f` from the EISPACK package of the NETLIB libraries which handles general complex matrices by use of the QR-algorithm. The characteristic frequencies of the star's oscillation modes are obtained as eigenvalues of eq. 3.31, the perturbation quantities X are the corresponding eigenvalues. The output of the code is sorted by decreasing complex frequency amplitude.

3.3.2 Testing the method

In order to test the QR-algorithm we applied it to the problem of polar perturbations of spherical symmetric stars with the use of the Cowling approximation (solved in section 2.3.2). We find that the results converge to the expected number (here we compare with the output of our integration routine with the highest accuracy) in second order with respect to the radial resolution [3]. We will apply now this method to our eigenvalue problem for axisymmetric neutron stars.

[3] We used here central differences.

Chapter 4

Axisymmetric background

4.1 Problem set-up

4.1.1 Equilibrium background

Pulsars, believed to be the observational analogue of neutron stars, have been observed to spin up to millisecond periods. This results in significant deviations from spherical symmetry both for the fluid configuration of the star and for the spacetime. Equilibrium solutions will thus not be spherically symmetric, but axisymmetric at most. The general form of an axisymmetric metric describing a rotating body can be written as:

$$ds^2 = -e^{\gamma+\rho}dt^2 + e^{2\alpha}\left(dr^2 + r^2 d\theta^2\right) + e^{\gamma-\rho}r^2\sin^2\theta\left(d\phi - \omega dt\right)^2. \qquad (4.1)$$

where r,θ,ϕ are quasi-isotropic coordinates, reducing to isentropic ones for no rotation (see Stergioulas, 2003). Restricting ourselves to uniform rotation with frequency Ω, the 4-velocity of the fluid is given by $u^\alpha = U^0\{1, 0, 0, \Omega\}$, with an energy-moment tensor $T_{\mu\nu} = p\, g_{\mu\nu} + (p + \epsilon)\, u_\mu u_\nu$, assuming that the star consists of an ideal fluid. For the equation of state we use a simple polytropic model of the form $p = k \times \rho_0^\gamma$. The main difference with the polytropic equation of state used in the previous chapter (2), is that ρ_0 is not identical any more with the total energy-density ϵ, but rather form it together with the internal energy-density $\rho_i = \frac{p}{\gamma-1}$, ie $\epsilon = \rho_0 + \rho_i$. Using a realistic equation of state in tabulated form would not affect our analysis or our numerical procedure. Again, we restrict ourselves to a polytropic equation of state to facilitate comparison of our results with previous studies by other authors.

For rapidly rotating stars, the background quantities cannot be solved any more through equations as simple as eqs. 2.1. The dependency on both r and θ coordinates of the (increased in number) variables, yield a complicated system of equations that needs to be integrated carefully. We use the RNS code of Stergioulas & Friedman (1995) for computing the background models, which is based on the Komatsu-Eriguchi-Hachisu method (Komatsu *et al*, 1989). The grid of the RNS code has fixed spacing on coordinates $s = \frac{r}{r+r_e}$ and $\mu = \cos\theta$.

Table 4.1: The polytropic ($p = k \times \rho_0^\gamma$) models produced with the RNS code used here. The ones marked with an asterisk ($\star$) were also used by Font *et al* (2001) and all have $k = 217.856\text{km}^2$ and $\epsilon_c = 0.894 \times 10^{15}\text{g/cm}^3$. A less massive star described by the poly-2 model was initially used and has $k = 100\text{km}^2$ and $\epsilon_c = 3 \times 10^{15}\text{g/cm}^3$.

Model	Gravitational Mass	Radius	Ω	Rotation rate (ν)
poly-2	$1.05\text{M}_\odot$	8.78 km	0	0
BU0*	$1.4\text{M}_\odot$	14.15 km	0	0
BU1*	$1.432\text{M}_\odot$	14.51 km	2.185 kHz	348Hz
BU6*	$1.627\text{M}_\odot$	17.25 km	4.984 kHz	793Hz

In order to avoid extrapolating the values of the background quantities to other points, we will work on the same grid and will be evaluating the derivatives that appear in our equations through $\frac{\partial}{\partial r} = \frac{r_e}{(r+r_e)^2}\frac{\partial}{\partial s}$ and $\frac{\partial}{\partial \theta} = -\sin\theta\frac{\partial}{\partial \mu}$. To avoid confusion we will consistently refer to the dependency on r, θ in the equations, keeping in mind the above.

The same code was also used by Font *et al* (2001); we will occasionally refer to their results for comparison. Some of their models which we will be using here are shown in Table 4.1. For those the parameters in the equation of state are $k = 217.856\text{km}^2$ and $\gamma = 2$ and the central density is $\epsilon_c = 0.894 \times 10^{15}\text{g/cm}^3$. BU1 is a non-rotating model, while BU1 and BU6 describe a slowly and rapidly rotating neutron star respectively. The radius presented is the circumferential one at the equator, which is not equal to the coordinate radius, due to the use of quasi-isotropic coordinates (see above). We will be using the coordinate radius when showing eigenfunctions, but one has to keep in mind that this is not the physical radius, which at the equator would be given by $e^{(\gamma-\rho)/2}r$, together of course with the transformation to SI units (see appendix A). So the BU1 model has a coordinate radius of 8.32 (in RNS units), the BU1 8.12 and BU6 9.95.

4.1.2 Perturbations

Using the above stationary configurations, we assume small deviations for the fluid variables and study their linearized perturbations. Since the background is not spherically symmetric it is not helpful to decompose the perturbations into spherical harmonics. Instead exploit the axisymmetry of the background by writing the perturbation quantities as

$$\delta p = He^{im\phi} \tag{4.2}$$

$$\delta u_\alpha = \frac{1}{p+\epsilon}\{-\Omega f_3, f_1, f_2, f_3\}e^{im\phi}, \tag{4.3}$$

where H, f_i are functions of t, r, θ. The relation $\delta u_t = -\Omega \delta u_\phi$ used above, was derived from the condition

$$-1 = u_\mu u^\nu = g_{\mu\nu} u^\mu u^\nu = \left(\tilde{g}_{\mu\nu} + h_{\mu\nu}\right)\left(u^\mu + \delta u^\mu\right)\left((u^\nu + \delta u^\nu\right)$$

with $h_{\mu\nu} \approx 0$, while the reason for the normalization with $p + \epsilon$ will become clear in the paragraph with the boundary conditions. The perturbation of the energy-density is related to the pressure perturbation through

$$\delta p = \frac{dp}{d\epsilon}\delta\epsilon \equiv C_s^2 \delta\epsilon,$$

where C_s is the speed of sound.

Again we use the relativistic Cowling approximation, (Cowling (1941)) by neglecting the metric perturbations. This will not allow us to calculate any damping of the modes due to emission of gravitational waves, but we can estimate the oscillation frequencies and study the overall structure of the spectrum (see also section 1.2). The full set of perturbed equations including the metric perturbations, apart from lengthy, would require accounting for the boundary conditions at infinity, still an unresolved problem in general relativity. An additional advantage of the Cowling approximation reflects on the numerical procedure that gives a form to our problem that can be solved straightforward (see section 3.3).

The equations that describe the behavior of the perturbed quantities arise from the perturbed form of the conservation of energy-momentum for stationary spacetime (equations of motion for the fluid):

$$\delta\left(T^\nu_{\mu;\nu}\right) = g^{\kappa\nu}(\delta T_{\mu\kappa,\nu} - \delta T_{\mu\rho}\Gamma^\rho_{\nu\kappa} - \Gamma^\rho_{\mu\nu}\delta T_{\rho\kappa}) = 0 \tag{4.4}$$

In general, these yield four independent partial differential equations which are of first order in time and space. We perform our mode calculations by assuming a harmonic time-dependence $e^{i\sigma t}$ for all four variables (e.g. $H(t, r, \theta) = \bar{H}(r, \theta)e^{i\sigma t}$), searching for frequencies which allow non-trivial solutions of the perturbation equations.

4.1.3 Boundary conditions

We need to take into account boundary conditions at the center and at the surface of the star, and a regularity condition in the angular direction. At the center, all variables are required to vanish by the regularity condition there. This results from Taylor expansion of the perturbed and unperturbed variables close to the center which reveals their behavior there, $\delta p \sim r^\ell$, which is also the behavior of f_θ, f_ϕ while f_r goes somewhat slower to zero at the center: as $r^{\ell-1}$. For the $m \geq 2$ case that we are mainly interested, we implement this condition simply by setting all variables to zero at $r = 0$. For the axisymmetric modes ($m = 0$), we need to let the perturbed variables be determined through eqs. 4.4, where their the derivatives are then zero.

Table 4.2: The symmetries with respect to the rotational axis of the perturbed fluid variables for both parities of $m > 0$.

Pert. variable	angular dependence	Symmetry wrt axis	
		Even m	Odd m
δp	$P_\ell^m e^{im\phi}$	symmetric	antisymmetric
δu_t	$P_\ell^m e^{im\phi}$	symmetric	antisymmetric
δu_r	$P_\ell^m e^{im\phi}$	symmetric	antisymmetric
δu_θ	$\partial_\theta(P_\ell^m e^{im\phi}) - \frac{1}{\sin\theta}\partial_\phi(P_\ell^m e^{im\phi})$	antisymmetric	symmetric
δu_ϕ	$\frac{1}{\sin\theta^2}\left[\partial_\phi(P_\ell^m e^{im\phi}) + \sin\theta\partial_\theta(P_\ell^m e^{im\phi})\right]$	symmetric	antisymmetric

At the surface, all perturbation variables must vanish: this follows from the definition of the variables given in Eqs. (4.2), since $p = \epsilon = \partial_r p = 0$ (for polytropic equations of state) and $\delta p \sim \partial_r p$ (to first order in a Taylor expansion). This justifies our special choice of defining the perturbed variables, since otherwise only the pressure perturbation would vanish on the surface for the equations of state that we consider here.

For the boundaries in the θ-direction one may use the fact that the rotational axis itself is special: For $m > 0$, all variables have to vanish on the rotational axis due to regularity conditions [1]. This can be used directly to set the discretized variables to zero there by hand.

For $m = 0$ we may construct a grid in such a way that no grid points fall on the rotational axis. In specific, the first point lies $\Delta\mu/2$ away from the axis, where $\Delta\mu$ is the fixed spacing in $\mu \equiv \cos\theta$ of the background model. In this case, one must use the symmetry to construct a boundary condition in the θ-direction. This technique is also applicable for $m > 0$, keeping in mind that the symmetry is different for even and odd values of m. In particular, for even m δp, δu_r and δu_ϕ are symmetric with respect to the axis ($\theta = 0, \pi$) and δu_θ is antisymmetric there. This is what one finds from the symmetries of the Legendre Polynomials themselves (see appendix B) and their derivatives that define the perturbed 4-velocity. For example, δu_θ – having the same symmetry properties as f_θ – can be expressed as the sum of polar contributions and axial ones, whose θ-behavior are $\frac{\partial P_\ell^m}{\partial\theta}$ and $\frac{im}{\sin\theta}P_\ell^m$ respectively; 'axial-led' are then called the modes with ℓ taking values $m + 2k$ for the first term and $m + 2k + 1$ for the second (k integer), while 'polar-led' in the opposite case. For even m both terms are antisymmetric with respect to the rotational axis. Table 4.2 shows the symmetries for all perturbation variables and both cases of parity. For axisymmetric perturbations the δu_θ and δu_ϕ have purely polar and axial behavior respectively but should retain the symmetry indicate for $m > 0$. The other perturbed variables behave as scalars under rotation and keep the symmetries

[1] The $e^{im\phi}$-dependency of the fluid perturbations requires that on the axis all possible azimuthal angles give the same value, i.e. zero. This is rather a physical condition, since, mathematically speaking, the definition of δu_ϕ would eg. allow the ϕ part to be non-vanishing.

indicated above. We implement these symmetries when needing to use a point out of the discretization grid to express the θ-derivatives of a variable.

We have used both techniques for the boundary conditions for the $m = 2$ case and found no significant difference. In order to make the code applicable both in the axisymmetric and the non-axisymmetric case, we implemented the second possibility of leaving out the axis from the grid.

4.1.4 Numerical effect of background on perturbations

The RNS code itself has finite resolution and thus introduces some numerical error into the results. We will always see a combination of numerical error coming from the RNS code and from our own code. When we attempt to study convergence properties we therefore use a high but fixed resolution of the RNS code, varying only the resolution of our eigenvalue code. In order to avoid the use of interpolation and the additional error associated with it, we run our code only with grid spacings which are multiples of the fixed grid spacing we have chosen for the RNS code. So, for a model with 101 radial points[2] and 100 angular ones, the background grid we use can have a combination of 11,21,26,51 or 101 radial points and 10,20,25,50 or 100 angular points. No arbitrary combination of the two is though allowed, since segmentation faults occur if the matrix dimension of our code (number of variables times n_r times n_θ) is higher than $\sim$4000 points.

4.1.5 Differentiation scheme

Although central differences is the most common and trusted scheme for expressing derivatives on a numerical grid, we need to test this when solving a system of equations instead of a higher order (single) equation. We solved for the simple case of non-rotating star in two dimensions (see subsection 4.2.1 and eqs.4.5) for $m = 2$. In table 4.3 we show the lowest resulting eigenfrequencies for the model poly-2 (see table 4.1) for a fixed θ-resolution [3] and increasing resolution in the radial direction. The computed frequencies show the expected convergence (second order for central differences and first order for one-sided differences) so one can extrapolate the computed values to get an eigenfrequency of 'infinite' resolution (see also figure 4.1). The relative mean deviation of the fitted numbers are of the order or less than 1%. Note that there is an additional systematic error, related to the finite accuracy of the background quantities, of the same order. The two lowest-frequency modes of the second order scheme –identified as the fundamental pressure modes for $\ell = 2$ and $\ell = 3$ (see also subsection 4.2.1)– were also found with a one-sided differences scheme but close to each of those frequencies, we find additional solutions with similar eigenfunctions. It becomes obvious from their non-appearance in the well resolved equivalent analysis in one dimension (chapter 2) that these solutions are just numerical artifacts. The reason for this is probably due to the different behavior

[2]The RNS code requires an odd number of radial points.

[3]More points in the θ direction do not seem to affect the results and are computationally expensive.

Table 4.3: The lowest frequency solutions of the system of equations 4.5 for the poly-2 equation of state (see 4.1) with several resolutions in the radial direction and a fixed number of θ-points. The third and last columns show the fundamental modes corresponding to $\ell = 2$ and $\ell = 3$, while the intermediate solutions found are numerical artifacts from the central differencing scheme. In the next to last row the extrapolated values for 'infinite' r-resolution (see figure 4.1) are listed, while the last one shows the corresponding solutions of the second order system.

n_θ	n_r	$f_{\ell=2}$	$f'_{\ell=2}$	$f'_{\ell=3}$	$f_{\ell=3}$
10	5	3478	3788	4796	5096
	10	3234	3413	3927	4072
	20	3203	3362	3784	3894
	25	3199	3358	3776	3883
	∞	**3192**	**3349**	**3760**	**3858**
2^{nd}OS		3220			3868

of the four eigenfunctions, in contrast to the single eigenfunction of the second order equation. After a numerical trial-and-error procedure we found that with a one-sided differentiation scheme – in different direction for the two variables with θ derivatives – these unphysical modes disappear and we obtain consistent results. It is not clear why this specific numerical scheme resolved the inconsistency, it might though be due to over-determination by use of more conditions at the angular boundary than the system itself allows. We will, from now, on only use one-sided differentiation to solve the system of equations needed.

4.2 Axisymmetric perturbations

We begin our analysis by using the corresponding equations in their general form, including all terms with arbitrary m. Setting $m = 0$ we select perturbations that are symmetric around the rotation axis, which include all $\ell \geq 0$ contributions. Axisymmetric perturbations have been studied by Font *et al* (2001) using nonlinear time-evolution; we will turn to their results for comparison. In order to gain a better understanding of the underlying physics and numerics, we first solve Eqs. (4.4) for the non-rotating case, where expressions can also take a considerably reduced form. We then proceed to include rotation at arbitrary rotation rate.

Table 4.4: The frequencies ($\frac{\sigma}{2\pi}$) of the first three fundamental modes (f) and the lowest pressure mode (p^1) for axisymmetric oscillations of BU0, for several resolutions in the radial direction and a fixed number of θ-points. In the next to last row the extrapolated values for 'infinite' r-resolution (see figure 4.1) are listed, while the last row shows the results of Font *et al* (2001).

n_θ	n_r	$f_{\ell=1}$	$f_{\ell=2}$	$f_{\ell=0}$	$p^1_{\ell=2}$
10	21	1377	1974	3076	4627
	26	1367	1943	3032	4551
	51	1344	1872	2917	4344
	101	1328	1830	2840	4197
	∞	**1317**$\pm$2	**1794**$\pm$3	**2787**$\pm$11	**4102**$\pm$26
Font *et al* (2001)		1335	1846	2706	4100

4.2.1 No rotation

Setting $\Omega = 0$ in Eqs. (4.4) and using harmonic time-dependence the system of equations for the variables defined in Eqs. 4.2 takes the form:

$$\begin{aligned} i\sigma H &= -\frac{imC_s^2 e^{2\rho}U^0}{r^2\sin^2\theta} f_3 - \frac{C_s^2}{e^{2\alpha}U^0}\left\{\frac{1}{r^2}\left(\frac{\partial f_2}{\partial\theta} + \frac{\cos\theta}{\sin\theta} f_2\right) + \frac{\partial f_1}{\partial r} + \left(\frac{3}{2}\frac{\partial\gamma}{\partial r} + \frac{1}{2}\frac{\partial\rho}{\partial r} + \frac{2}{r}\right) f_1\right\} \\ i\sigma f_3 &= -\frac{im}{U^0} H, \qquad i\sigma f_1 = -\frac{1}{U^0}\frac{\partial H}{\partial r}, \qquad i\sigma f_2 = -\frac{1}{U^0}\frac{\partial H}{\partial\theta} \end{aligned} \tag{4.5}$$

In this simple case, one variable (H) would be sufficient to describe the whole oscillation problem since one can transform the system of Eqs. (4.5) into a single second order equation. Solving the latter with the numerical procedure described earlier (subsection 4.1.5) gave same results as solving Eqs. (4.4) for $\Omega = 0$, so we will keep presenting results from the full first-order system for consistency [4].

Table 4.4 shows the lowest resulting eigenfrequencies for the model BU0 with increasing resolution in the radial direction, starting from 21 points. Increasing the resolution in the θ direction again does not seem to affect the results for these models and we therefor keep it fixed.

Figure 4.1 shows a plot of the ($l = 2, m = 0$) f-mode frequencies from Table 4.4 as a function of the radial resolution. They follow an inverse power law of the form $f = f_\infty + \delta f/n_r + \ldots$, i.e. first order convergence, as one would expect for one-sided differences. We may thus extrapolate the computed values to obtain an eigenfrequency f_∞ at nominally infinite resolution. In general, the relative mean deviation of the fitted numbers is less than 1%. Note that there is an additional systematic error of the same general magnitude, resulting from the finite accuracy of the background quantities (see subsection 4.1.4).

Since the background is spherically symmetric, we can still assign a definite value of ℓ to the oscillation modes. Comparing the extrapolated frequencies in

[4] For rapid rotation this transformation to a single equation will probably not be possible.

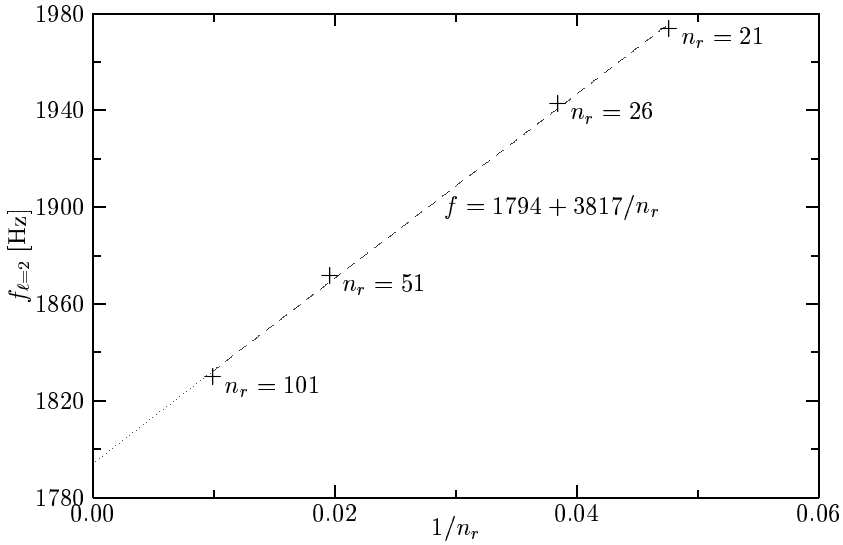

Figure 4.1: The computed eigenfrequencies (here the $\ell = 2$ f-mode for BU0) follow an inverse power law. We may extrapolate to $n_r \to \infty$ to obtain the frequencies for nominally infinite radial resolution.

Table 4.4 with results by Font *et al* (2001), we conclude that they correspond to the fundamental modes that correspond to $\ell = 0, 1, 2$ and the first pressure mode for $\ell = 2$, with an agreement up to a few percent. The small differences are likely due to the finite resolution of the background calculation.

Eigenfunctions of p-modes The identification of the pressure modes was based in this case just on looking at the frequencies of the resulting solutions and comparing with the literature. The corresponding eigenfunctions, though, were also examined, and in some cases, were the frequency separation of two modes was small[5], they revealed the order of the modes. This will become very important for inertial modes, were the frequency separation between modes is expected to be much smaller. In figures 4.2 and 4.3 we plot the eigenfunction of the modes whose frequencies were followed and shown in Table 4.4. Shown is the pressure perturbation, which is the main quantity for such modes.

The above method remains basically the same when we turn on rotation. We thus expect to obtain the fluid modes with similar accuracy even for rapid rotation. The picture may change, though, for the rotation-driven modes: These are degenerate at zero frequency in the non-rotationg case. Therefor, there are no results for the non-rotating case that can be used as an indication for the

[5]This can happen more easy for low resolution, since modes converge differently with n_r and in some cases one mode might appear with lower frequency than another which in 'infinite' resolution appears first on the frequency axis.

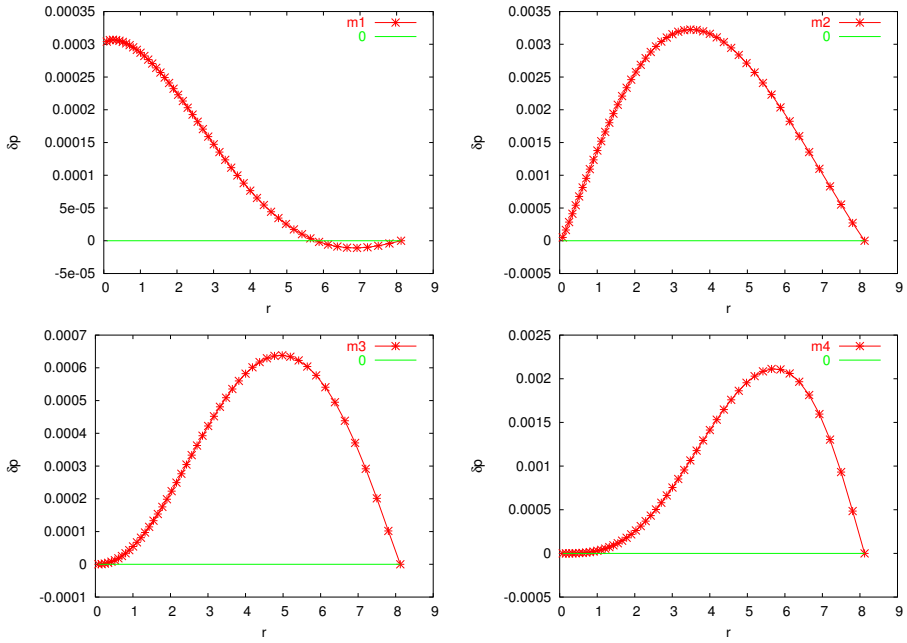

Figure 4.2: The r-dependence of the eigenfunctions of the $\ell = 1$ and $\ell = 2$ f-modes that are presented in table 4.4 (at an angle of $\sim \pi/4$).

accuracy of our computational results.

4.2.2 Rapid rotation

With rotation being included the equations of motion for the fluid become quite lengthy. They take the form:

$$
\begin{aligned}
\Pi\frac{\partial H}{\partial t} \quad = \quad & -\frac{imC_s^2}{r^2\sin^2\theta e^{\gamma+\rho}U^0}\left\{e^{2\rho}r^2\sin^2\theta\Omega^2+\left[e^{2\rho}+\omega r^2\sin^2\theta(\Omega-\omega)\right]^2\right\}f_3 \\
& -C_s^2U^0\frac{e^{\gamma-\rho}}{e^{2\alpha}}\left\{\frac{r^2\sin^2\theta\omega(\Omega-\omega)}{(U^0)^2e^{\gamma-\rho}}\left(\frac{3}{2}\frac{\partial\gamma}{\partial r}-\frac{1}{2}\frac{\partial\rho}{\partial r}+\frac{\partial\ln(p+\epsilon)}{\partial r}+\frac{3}{r}\right)\right. \\
& -r^4\sin^4\theta\left(\Omega-\omega\right)^3\frac{\partial\omega}{\partial r}-e^{2\rho}r^2\sin^2\theta\left[\omega\frac{\partial\omega}{\partial r}+\Omega(\Omega-\omega)\left(\frac{\partial\rho}{\partial r}-\frac{1}{r}\right)\right] \\
& \left.+\frac{e^{2\rho}}{(U^0)^2e^{\gamma-\rho}}\left(\frac{3}{2}\frac{\partial\gamma}{\partial r}+\frac{1}{2}\frac{\partial\rho}{\partial r}+\frac{\partial\ln(p+\epsilon)}{\partial r}+\frac{2}{r}\right)\right\}f_1 \\
& -\frac{C_s^2}{r^2}U^0\frac{e^{\gamma-\rho}}{e^{2\alpha}}\left\{\frac{r^2\sin^2\theta\omega(\Omega-\omega)}{(U^0)^2e^{\gamma-\rho}}\left(\frac{3}{2}\frac{\partial\gamma}{\partial\theta}-\frac{1}{2}\frac{\partial\rho}{\partial\theta}+\frac{\partial\ln(p+\epsilon)}{\partial\theta}\right)\right.
\end{aligned}
$$

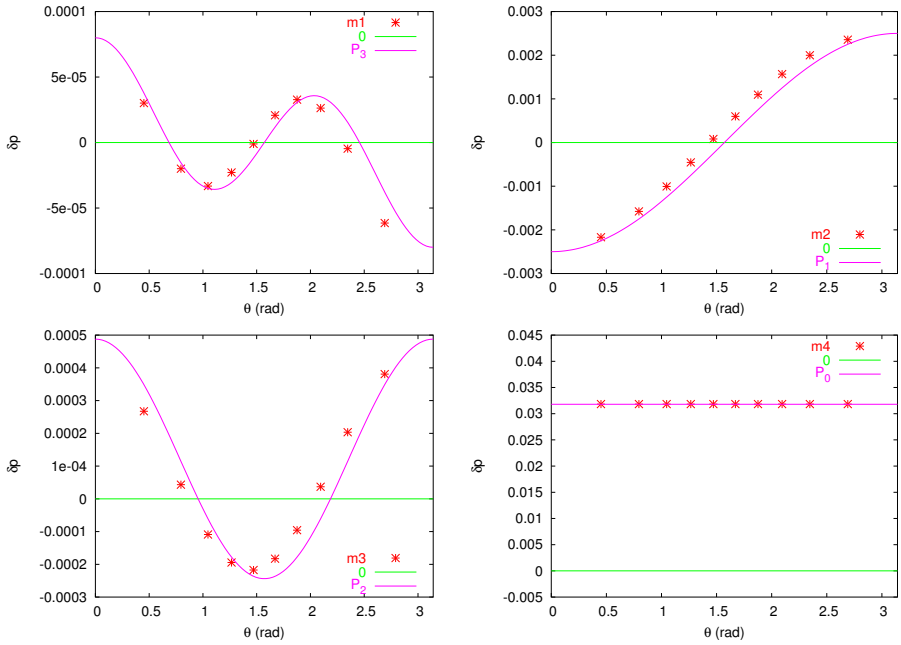

Figure 4.3: The θ-dependence of the eigenfunctions of the $\ell = 1$ and $\ell = 2$ f-modes that are presented in table 4.4.

$$
\begin{aligned}
& -r^4 \sin^4\theta\,(\Omega-\omega)^3\left(\frac{\partial\omega}{\partial\theta}+2\omega\frac{\cos\theta}{\sin\theta}\right)-e^{2\rho}r^2\sin^2\theta\left[\omega\frac{\partial\omega}{\partial\theta}+\Omega(\Omega-\omega)\left(\frac{\cos\theta}{\sin\theta}-\frac{\partial\rho}{\partial\theta}\right)\right] \\
& +\frac{e^{2\rho}}{(U^0)^2e^{\gamma-\rho}}\left(\frac{3}{2}\frac{\partial\gamma}{\partial\theta}+\frac{1}{2}\frac{\partial\rho}{\partial\theta}+\frac{\partial\ln(p+\epsilon)}{\partial\theta}+\frac{\cos\theta}{\sin\theta}\right)\Bigg\}f_2 \\
& -im\Omega\left(1+C_s^2\right)\left[e^{2\rho}+r^2\sin^2\theta\omega\,(\Omega-\omega)\right]H \\
& -\frac{C_s^2}{U^0}\Bigg\{e^{-2\alpha}\left[e^{2\rho}+r^2\sin^2\theta\omega\,(\Omega-\omega)\right]\left(\frac{\partial f_1}{\partial r}+\frac{1}{r^2}\frac{\partial f_2}{\partial\theta}\right)-\frac{\omega Z-2\Omega e^{2\rho}}{e^{\gamma+\rho}}\frac{\partial f_3}{\partial t}\Bigg\} \qquad (4.6)
\end{aligned}
$$

$$
\begin{aligned}
Z\frac{\partial f_3}{\partial t} \;=\;& im\left(\omega Z-2\Omega e^{2\rho}\right)f_3-ime^{\gamma+\rho}U^0\left[e^{2\rho}+r^2\sin^2\theta(\Omega-\omega)\left(\frac{\Omega}{C_s^2}+\omega\right)\right]H \\
& -r^2\sin^2\theta\frac{\Omega-\omega}{e^{2\alpha}}e^{\gamma+\rho}\Bigg\{\frac{3}{2}\frac{\partial\gamma}{\partial r}-\frac{1}{2}\frac{\partial\rho}{\partial r}+\frac{\partial\ln(p+\epsilon)}{\partial r} \\
& \qquad +\frac{3}{r}+(U^0)^2e^{\gamma+\rho}\left[-\frac{\partial\rho}{\partial r}+\frac{\partial\ln(\Omega-\omega)}{\partial r}+\frac{1}{r}\right]\Bigg\}f_1- \\
& \sin^2\theta\frac{\Omega-\omega}{e^{2\alpha}}e^{\gamma+\rho}\Bigg\{\frac{3}{2}\frac{\partial\gamma}{\partial\theta}-\frac{1}{2}\frac{\partial\rho}{\partial\theta}+\frac{\partial\ln(p+\epsilon)}{\partial\theta}+2\frac{\cos\theta}{\sin\theta} \\
& \qquad +(U^0)^2e^{\gamma+\rho}\left[-\frac{\partial\rho}{\partial\theta}+\frac{\partial\ln(\Omega-\omega)}{\partial\theta}+\frac{\cos\theta}{\sin\theta}\right]\Bigg\}f_2
\end{aligned}
$$

$$-r^2\sin^2\theta(\Omega-\omega)e^{\gamma+\rho}\left\{e^{-2\alpha}\left(\frac{\partial f_1}{\partial r}+\frac{1}{r^2}\frac{\partial f_2}{\partial\theta}\right)+U^0\left(1+\frac{1}{C_s^2}\right)\frac{\partial H}{\partial t}\right\} \tag{4.7}$$

$$\frac{\partial f_1}{\partial t} = -\left\{2(\Omega-\omega)\left(\frac{\partial\rho}{\partial r}-\frac{1}{r}\right)+e^{-2\rho}Z\frac{\partial\omega}{\partial r}\right\}f_3 - im\Omega f_1 - \frac{1}{U^0}\frac{\partial H}{\partial r} \tag{4.8}$$

$$\frac{\partial f_2}{\partial t} = -\left\{2(\Omega-\omega)\left(\frac{\partial\rho}{\partial\theta}-\frac{\cos\theta}{\sin\theta}\right)+e^{-2\rho}Z\frac{\partial\omega}{\partial\theta}\right\}f_3 - im\Omega f_2 - \frac{1}{U^0}\frac{\partial H}{\partial\theta}, \tag{4.9}$$

where

$$\begin{aligned}\Pi &= e^{2\rho}+r^2\sin^2\theta(\Omega-\omega)\left(C_s^2\Omega+\omega\right)\\ Z &= e^{2\rho}+r^2\sin^2\theta(\Omega-\omega)^2\\ \left[(U^0)^2e^{\gamma-\rho}\right]^{-1} &= e^{2\rho}-r^2\sin^2\theta(\Omega-\omega)^2,\end{aligned}$$

while U^0 is the t-component of the unperturbed 4-velocity with upper indices, $u^\alpha = U^0\{1,0,0,\Omega\}$.

This system could not be transformed into a higher order system with less equations, so we have to deal with all 4 equations and variables. When using the harmonic time-dependence, the frequency σ would appear also on the right hand side. Therefore, this form is not suitable for performing an explicit eigenvalue calculation as described in subsection 3.3.1. We thus define new variables:

$$\begin{aligned}F &= \Pi H + AC_s^2 f_3\\ V &= \mathrm{Z}C_s^2 f_3 + BH,\end{aligned}$$

where

$$\begin{aligned}A &= \left(2\Omega e^{2\rho}-\frac{\omega}{(U^0)^2e^{\gamma-\rho}}\right)\frac{1}{e^{\gamma+\rho}U^0}\\ B &= r^2\sin^2\theta(\Omega-\omega)e^{\gamma+\rho}U^0(1+C_s^2),\end{aligned}$$

which together with f_1, f_2 form the set of variables we will use from now on. The eigenvector $\vec{X}$ for the code (see 3.3.1) consists of the values of these four variables at each combination of radial and angular coordinate i, j, ie $\vec{X} = \{F^{1,1}, V^{1,1}, f_1^{1,1}, f_2^{1,1}, F^{1,2}, V^{1,2}, f_1^{1,2},, f_2^{1,2}\ldots, F^{i,j}, V^{i,j}, f_1^{i,j},, f_2^{i,j}, \ldots, F^{n_r,n_\theta}, V^{n_r,n_\theta}, f_1^{n_r,n_\theta},, f_2^{n_r,n_\theta}\}$, where n_r, n_θ are the number of points in the radial and angular direction respectively. The full set of equations eventually becomes:

$$\begin{aligned}i\sigma F = {} & \frac{imF}{Z\Pi-AB}\left\{B\frac{\left[e^{2\rho}+r^2\sin^2\theta\omega(\Omega-\omega)\right]^2+e^{2\rho}\Omega^2r^2\sin^2\theta}{r^2\sin^2\theta e^{\gamma+\rho}U^0}\right.\\ & \left.-(1+C_s^2)\Omega Z\left[e^{2\rho}+r^2\sin^2\theta\omega(\Omega-\omega)\right]\right\}\\ & -\frac{imV}{Z\Pi-AB}\left\{\Pi\frac{\left[e^{2\rho}+r^2\sin^2\theta\omega(\Omega-\omega)\right]^2+e^{2\rho}\Omega^2r^2\sin^2\theta}{r^2\sin^2\theta e^{\gamma+\rho}U^0}\right.\end{aligned}$$

$$
\begin{aligned}
&-(1+C_s^2)\Omega A\left[e^{2\rho}+r^2\sin^2\theta\omega(\Omega-\omega)\right]\Bigg\}\\
&-C_s^2U^0\frac{e^{\gamma-\rho}}{e^{2\alpha}}\Bigg\{\frac{e^{2\rho}+r^2\sin^2\theta\omega(\Omega-\omega)}{(U^0)^2e^{\gamma-\rho}}\left(\frac{3}{2}\partial_r\gamma-\frac{1}{2}\partial_r\rho+\frac{3}{r}\right)\\
&-r^4\sin^4\theta\left(\Omega-\omega\right)^3\partial_r\omega+\frac{e^{2\rho}}{(U^0)^2e^{\gamma-\rho}}\left(\partial_r\rho-\frac{1}{r}\right)\\
&-e^{2\rho}r^2\sin^2\theta\left[\omega\partial_r\omega+\Omega(\Omega-\omega)\left(\partial_r\rho-\frac{1}{r}\right)\right]\Bigg\}f_1\\
&-\frac{C_s^2}{r^2}U^0\frac{e^{\gamma-\rho}}{e^{2\alpha}}\Bigg\{\frac{e^{2\rho}+r^2\sin^2\theta\omega(\Omega-\omega)}{(U^0)^2e^{\gamma-\rho}}\left(\frac{3}{2}\partial_\theta\gamma-\frac{1}{2}\partial_\theta\rho+2\cot\theta\right)\\
&-r^4\sin^4\theta\left(\Omega-\omega\right)^3\partial_\theta\omega+\frac{e^{2\rho}}{(U^0)^2e^{\gamma-\rho}}\left(\partial_\theta\rho-\cot\theta\right)\\
&-e^{2\rho}r^2\sin^2\theta\left[\Omega(\Omega-\omega)\left(\cot\theta-\partial_\theta\rho\right)-\omega\partial_\theta\omega\right]\Bigg\}f_2\\
&-\frac{C_s^2}{U^0}e^{-2\alpha}\left[e^{2\rho}+r^2\sin^2\theta\omega\left(\Omega-\omega\right)\right]\left(\partial_r f_1+\frac{1}{r^2}\partial_\theta f_2\right) \qquad (4.10)
\end{aligned}
$$

$$
\begin{aligned}
i\sigma V &= -\frac{im}{Z\Pi-AB}\Bigg\{B\left(\frac{\omega}{(U^0)^2e^{\gamma-\rho}}-2\Omega e^{2\rho}\right)\\
&+U^0e^{\gamma+\rho}Z\left[C_s^2e^{2\rho}+r^2\sin^2\theta(\Omega-\omega)(C_s^2\omega+\Omega)\right]\Bigg\}F\\
&+\frac{im}{Z\Pi-AB}\Bigg\{\Pi\left(\frac{\omega}{(U^0)^2e^{\gamma-\rho}}-2\Omega e^{2\rho}\right)\\
&+U^0e^{\gamma+\rho}A\left[C_s^2e^{2\rho}+r^2\sin^2\theta(\Omega-\omega)(C_s^2\omega+\Omega)\right]\Bigg\}V\\
&-C_s^2r^2\sin^2\theta\frac{\Omega-\omega}{e^{2\alpha}}e^{\gamma+\rho}\Big\{\frac{3}{2}\partial_r\gamma-\frac{1}{2}\partial_r\rho+\frac{3}{r}\\
&+(U^0)^2e^{\gamma+\rho}\left[-\partial_r\rho+\partial_r\ln\left(\Omega-\omega\right)+\frac{1}{r}\right]\Big\}f_1\\
&-C_s^2\sin^2\theta\frac{\Omega-\omega}{e^{2\alpha}}e^{\gamma+\rho}\Big\{\frac{3}{2}\partial_\theta\gamma-\frac{1}{2}\partial_\theta\rho+2\cot\theta\\
&+(U^0)^2e^{\gamma+\rho}\left[-\partial_\theta\rho+\partial_\theta\ln\left(\Omega-\omega\right)+\cot\theta\right]\Big\}f_2\\
&-C_s^2r^2\sin^2\theta(\Omega-\omega)e^{\gamma+\rho}e^{-2\alpha}\left(\partial_r f_1+\frac{1}{r^2}\partial_\theta f_2\right) \qquad (4.11)\\
i\sigma f_1 &= \Bigg\{\frac{B}{C_s^2}\,\frac{2(\Omega-\omega)\left(\partial_r\rho-\frac{1}{r}\right)+e^{-2\rho}Z\partial_r\omega}{Z\Pi-AB}+\frac{\partial_r\ln\left(p+\epsilon\right)}{U^0(\Pi-AB/Z)}
\end{aligned}
$$

$$
\begin{aligned}
& -\frac{1}{U^0}\partial_r\left(\frac{Z}{Z\Pi - AB}\right)\Bigg\}F \\
& -\Bigg\{\frac{\Pi}{C_s^2}\,\frac{2(\Omega-\omega)\left(\partial_r\rho - \frac{1}{r}\right) + e^{-2\rho}Z\partial_r\omega}{Z\Pi - AB} + \frac{\partial_r \ln(p+\epsilon)}{U^0(Z\Pi/A - B)} \\
& -\frac{1}{U^0}\partial_r\left(\frac{A}{Z\Pi - AB}\right)\Bigg\}V \\
& -\frac{\partial_r F}{U^0(\Pi - AB/Z)} + \frac{\partial_r V}{U^0(Z\Pi/A - B)} - im\Omega f_1 \qquad (4.12)
\end{aligned}
$$

$$
\begin{aligned}
i\sigma f_2 \;=\; & \Bigg\{\frac{B}{C_s^2}\,\frac{2(\Omega-\omega)\left(\partial_\theta\rho - \cot\theta\right) + e^{-2\rho}Z\partial_\theta\omega}{Z\Pi - AB} + \frac{\partial_\theta \ln(p+\epsilon)}{U^0(\Pi - AB/Z)} \\
& -\frac{1}{U^0}\partial_\theta\left(\frac{Z}{Z\Pi - AB}\right)\Bigg\}F \\
& -\Bigg\{\frac{\Pi}{C_s^2}\,\frac{2(\Omega-\omega)\left(\partial_\theta\rho - \cot\theta\right) + e^{-2\rho}Z\partial_\theta\omega}{Z\Pi - AB} + \frac{\partial_\theta \ln(p+\epsilon)}{U^0(Z\Pi/A - B)} \\
& -\frac{1}{U^0}\partial_\theta\left(\frac{A}{Z\Pi - B}\right)\Bigg\}V \\
& -\frac{\partial_\theta F}{U^0(\Pi - AB/Z)} + \frac{\partial_\theta V}{U^0(Z\Pi/A - B)} - im\Omega f_2 \qquad (4.13)
\end{aligned}
$$

In Fig. 4.4 we show the solutions (up to 50kHz) returned by the eigenvalue code for axisymmetric perturbations of model BU1, using a low radial resolution of $n_r = 25$. As far as results for pressure modes are available from the literature we list them along with our results in Table 4.5. No previous results are available for axisymmetric inertial modes of rapidly rotating relativistic stars; see Ruoff *et al* (2003) for modes of slowly rotating stars. Very recently Dimmelmeier *et al* (2006) published frequencies of the three strongest axisymmetric inertial modes

Table 4.5: Frequencies (in kHz) of two fundamental $m = 0$ pressure-driven oscillations for the polytropic models BU1 and BU6, compared with the results of (Font *et al*, 2001). In the non-rotating limit these correspond to $l = 0$ and $l = 2$ modes. Again, our values have been extrapolated to nominally infinite radial resolution. Convergence in this case was not as clean as shown in Fig. 4.1, especially for the rapidly rotating model BU6. This is reflected in larger uncertainty estimates.

	$f_{l=0}$ (BU1)	$f_{l=2}$(BU1)	$f_{l=0}$(BU6)	$f_{l=2}$(BU6)
This work	2.720±20	1.834±25	2.292±193	1.718±85
Font *et al* (2001)	2.657	1.855	2.456	1.762

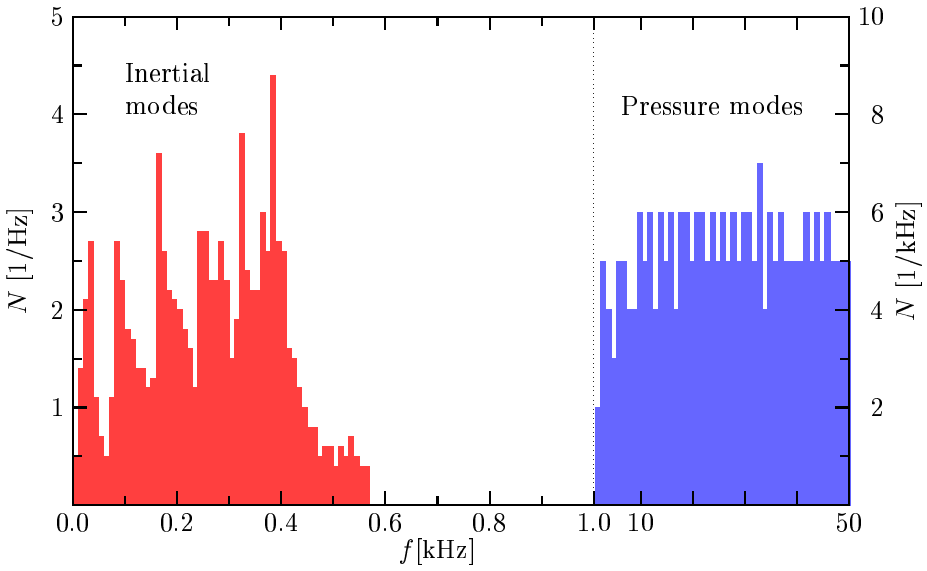

Figure 4.4: A histogram of the number of all solutions returned by the eigenvalue code for the $m = 0$ eigenvalue problem of the model BU1 up to a specific frequency. Both axis are scaled logarithmically; the frequency bins have a constant width of 10 Hz for the inertial mode frequencies and 1 kHz for the pressure mode frequencies.

in the conformally flat approximation. They all lie inside the corresponding inertial mode spectrum (see below). We will first concentrate on some general properties of the spectrum and then on individual modes.

The oscillation mode spectrum We notice from Fig. 4.4 that the eigenvalues are clustered into two groups, one above 1000Hz and one below. These correspond to the expected frequency ranges for pressure modes and inertial modes. The latter range is more densely populated; for example, we see more solutions between, say, 500 and 520 Hz than between 2 and 5 kHz. This is not as surprising as it may seem at first: according to theory (see eg. (Lockitch *et al*, 2004) for an overview table), there is an infinite number of pressure modes, with frequencies extending to infinity. For the inertial modes though, one expects an infinite number of modes as well, but confined to a well defined frequency range. According to our computation this range appears to extend from 0 to about 600 Hz for the model BU1.

In Fig. 4.5 we show the $p-$mode and inertial mode ranges separately for increasing radial resolution. In both ranges the number of frequency eigenvalues increases with increasing resolution. There is an important distinction, however: in the p-mode range, higher frequency ranges are increasingly populated as

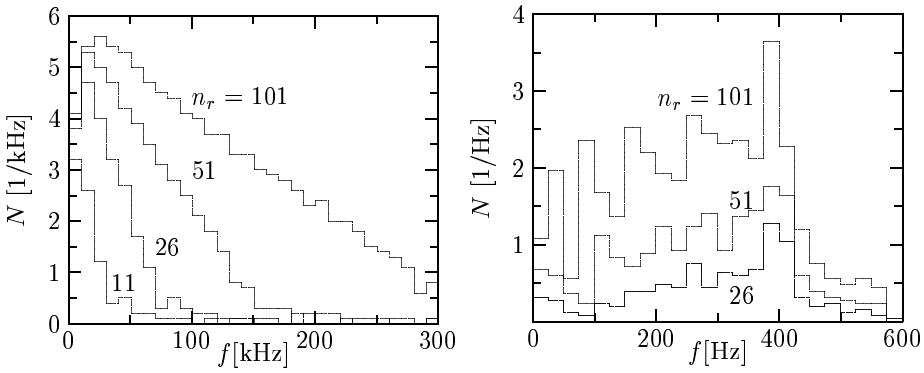

Figure 4.5: A histogram of the number of modes per frequency bin computed for the $m = 0$ eigenvalue problem of the model BU1 and for several resolutions; left for the p-modes with bins equally sized at 10kHz, and right for the inertial modes with a bin size of 25Hz.

the resolution increases, while the population of low frequencies approaches a limiting value. We observe that as the radial resolution n_r increases, the number of computed eigenvalues increases as $10 \times n_r$. The lowest p-mode frequency, which belongs to the $m = 2$ f-mode, is roughly the same for all resolutions. It shifts in frequency by a few hundred Hz, which is just a few percent of the bin size. Typically the number of solutions per frequency bin approaches a limit value α like $N_{\rm bin} \approx \alpha + \beta/n_r$ with some constant β.

For each stellar model the maximum value of frequency eigenvalues tends to infinity for increasing resolution. This is similar to the situation for quasi-normal modes of black holes, with an infinite number of modes which is not confined to a finite part of the complex frequency plane (see Nollert, 1993). In the case of black holes, however, the imaginary part of the frequency is unbounded, while it is the real (oscillatory) part of the frequency for pressure modes of relativistic stars.

In the inertial mode range, on the other hand, the frequency range does not change as the resolution increases; in fact, the upper limit (600Hz for model BU1) is quite robust. Instead, the population increases fairly homogeneously over the whole frequency range. The total number of solutions calculated develops, just as for the p-modes, like $10 \times n_r$. The number of points per bin grows linearly; for the bin e.g. around 400Hz, as $N_{\rm bin} \simeq 2 \times n_r$. This is a strong indication that an infinite number of solutions exists in this frequency range. It would seem likely that there is an infinite number of physical modes in this range as well.

While the upper limit for the frequency range does not depend on the resolution used in the numerical calculation, it actually depends linearly on the rotational frequency of the star, as shown in Fig. 4.6. The linear fit reveals $\sigma_{max} = 1.674 \times \Omega$ with a negligible statistical error.

The picture in Fig. 4.5 is actually quite common for numerical studies of

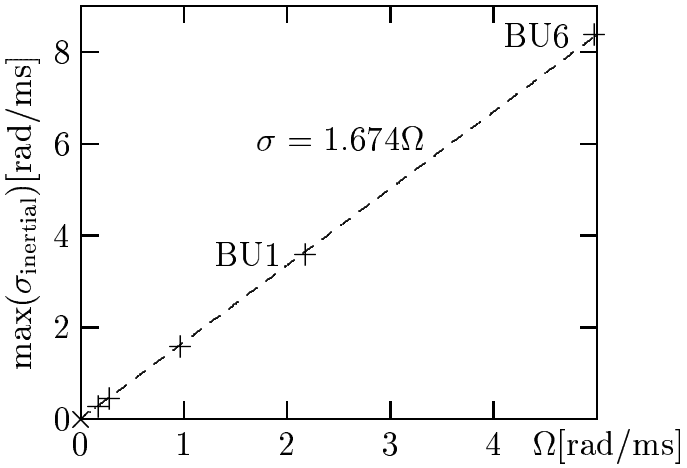

Figure 4.6: The highest inertial mode frequency as a function of the star's rotational frequency, starting at the model BU0 (no rotation) and moving up to model BU1 (2185Hz).

oscillation spectra: as one increases the resolution, frequency ranges at increasingly higher frequency become populated, while there is a finite limit for lower frequency ranges. Usually one expects that at low resolution, only modes with low frequencies can be computed reliably, since they are the only ones which can be resolved sufficiently well. High frequencies solutions are too inaccurate and cannot be trusted. With increasing resolution, the number of accurate solutions increases and their range extends to higher frequencies.

On the other hand, if we are confronted with a finite frequency range which shows an increasing number of solutions with increasing resolution, such a distinction cannot be made in a meaningful way. It is therefore not clear which of the numerical solutions in the frequency range corresponding to inertial modes should be considered physical solutions, and which should be discarded as numerical artefacts.

Just as in the non-rotating case, one can establish convergence for any finite value of the frequency in the upper range (Fig. 4.5), since there is a finite number of distinct modes in any finite frequency interval. The limit values very likely correspond to physical modes of the star. In the lower frequency range (left panel of fig. 4.5) it is not even clear how to establish a correspondence between eigenvalues at increasing resolutions, let alone define convergence and establish a correspondence to physical modes. However, given our numerical results, we consider it likely that the frequency range from 0 to 600 Hz does *not* contain only a *finite* number of inertial modes, in agreement with theoretical expectations. This leaves the following possibilities: There may be an infinite number of discrete frequencies, there may be a continuous spectrum, or

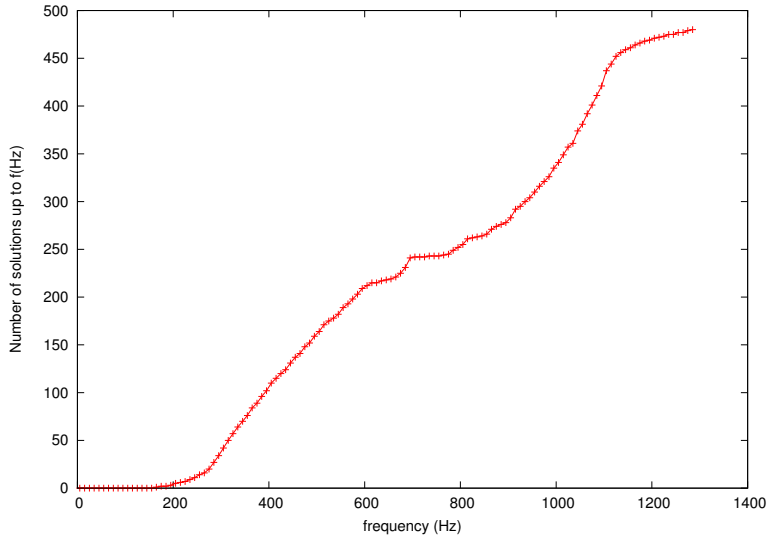

Figure 4.7: The number of solutions found in the inertial mode range for the BU6 model up to a frequency against that frequency.

a combination of these two. Note that an infinite number of frequencies in a finite frequency range implies the existence of at least one accumulation point. Such an accumulation point must be part of a continuous spectrum. A common example is the spectrum of a highly excited atom: it has an accumulation point at zero energy, which marks the edge of the continuous spectrum. However, the numerical limitations do not allow us to draw more specific conclusions, such as to the extent of a continuous spectrum, whether there are discrete modes in addition, where they may be, etc. The rather uneven distribution of solutions across the frequency range in question is an indication, though, that the actual spectrum may be far from having a simple structure.

An important indication for the existence of a continuous spectrum would be the appearance of accumulation points inside the frequency distributions of the inertial modes. We plot therefor an accumulative histogram in figure 4.7. The derivative of the total number of modes found up to a frequency over the frequency, is quite smooth without extremes, not supporting the existence of discrete accumulation points in that range.

Eigenfunctions The axisymmetric pressure modes calculated for the BU1 model, are not expected to differ significantly from the ones calculated for no rotation (BU0 model), as also seen from the frequencies. This becomes clear when one looks at the profiles of these modes. In figure 4.8 we see the eigenfunctions of the $\ell = 2$ fundamental pressure modes for BU0, BU1 and BU6. The pressure perturbation is plotted at an angle of 45 degrees for the radial eigen-

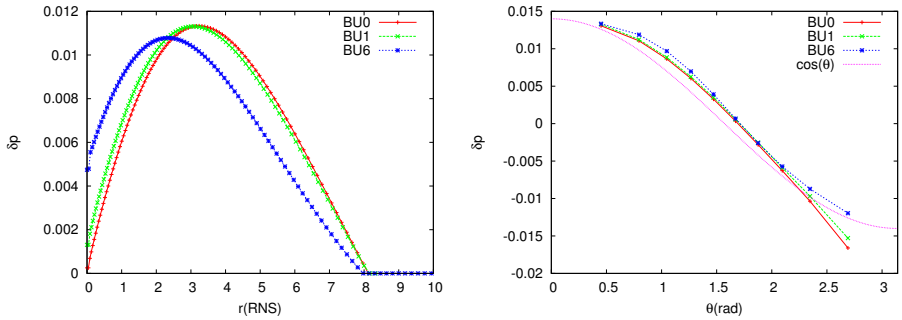

Figure 4.8: The pressure perturbation of the axisymmetric f-mode corresponding to $\ell = 1$ for $n_r = 101$ and for the models BU0, BU1 and BU6; on the right along the angular direction, at about half the radius and on the left along the radial direction at about 45 degrees.

function and around half the radius of the star for the angular one, (although for these modes it hardly makes a difference).

The eigenfunction corresponding to the $\ell = 1$ f-mode, does not change much from BU0 to BU1; for BU6 it has, though, already a slightly different form –the maximum of the pressure perturbation moves closer to the center of the star [6] – still different though from other f-modes of different ℓ. The corresponding extrapolated eigenfrequencies are 1326.5Hz, 1335.5 Hz and 1445.0 Hz for BU0, BU1 and BU6 respectively, with the convergence however not being always nice, possibly because a constant θ resolution is not any more a good approximation. This high rate of rotation influences also slightly the θ-eigenfunctions, which for this low order pressure mode still resembles very much [7] the Legendre polynomial for $\ell = 1$ and $m = 0$ ($P_0^1 = \cos\theta$, see App. B).

This picture is expected to change for inertial modes, where contributions might be less dominated by the first order term of the expansion. A typical inertial mode has a profile as in figure 4.9; it is clear that it belongs to a mode of higher order with complicated structure, both in r and θ. Unfortunately very little is available in the literature about the axisymmetric inertial modes. In order to be sure about these results we need to check with known eigenfunctions, since the frequency itself cannot uniquely define a mode inside this dense spectrum. The fundamental $\ell = m = 2$ r-mode is a good point of reference, since it has been the focus of many studies, both analytically and numerically. For that we will have to turn to axisymmetric modes, and concentrate on the $m = 2$ case.

[6] The sudden cut-off close to $r = 0$ is apparently due to the weakness of the code to describe the steep eigenfunction and the regularity condition there for axisymmetric modes.

[7] The opposite sign and different scaling compared to fig.4.3 is due to the different normalization.

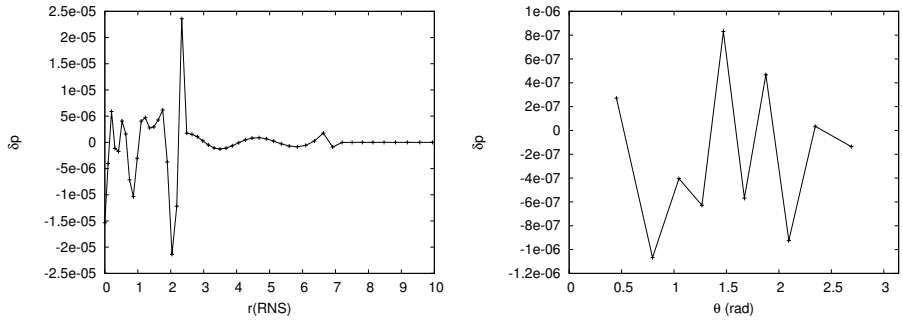

Figure 4.9: The pressure perturbation of a randomly chosen inertial mode of the BU6 model for $n_r = 51$, plotted in the same way as in figure 4.8. The mode has $\sigma = 0.77\Omega$.

4.3 Non-axisymmetric perturbations

For $m > 0$ the picture is more complicated but also more interesting than the axisymmetric case since the $m = 2$ modes are the ones most unstable to gravitational radiation. Solving this system for $m = 2$ and the BU1 model in the way described in the previous section we find a set of eigenvalues, containing both positive and negative frequencies. In the axisymmetric case negative eigenvalues are equivalent to the positive frequency solutions. Breaking axial symmetry shifts frequencies (for an asymptotic observer) towards negative values, so that much or even all of the frequency range corresponding to inertial modes becomes negative.

In Newtonian gravity (see e.g. Unno *et al* (1989)), a polar mode of order n, harmonic index ℓ and frequency σ_0, splits under rotation to $2\ell + 1$ modes with frequencies shifted to $\sigma = \sigma_0 - m\Omega E_{n\ell}$ $(+O(\Omega^2))$ where $E_{n\ell}$ is a function depending on the eigenfunction of each mode. For low order pressure modes the value of this function is about 0.1, so one would need rotational frequencies close to the Kepler limit for the frequency to change sign.

However, there are modes which have $\sigma < 0$ for *any* rotation rate, such as the r-modes which in the Newtonian, slow-rotation limit have $\sigma = -2m\Omega\frac{(\ell-1)(\ell+2)}{\ell(\ell+1)}$. This is the picture we find for $m = 2$, with all inertial modes having negative frequencies. Such a change of sign is often used as an indication for the corresponding mode to become unstable (see eg. Stergioulas, 2003).

In Fig. 4.6 we saw that the upper cutoff frequency for the inertial mode range grows linearly with the rotational frequency of the star. In the non-axisymmetric case, there is also a dependence on m. For the series of models listed in Table 4.1 we obtain a least square fit of $\sigma_{\max}/\Omega = 1.64 - 1.06 \times m$. The standard deviations in the above numbers are of the order of 0.01. For less relativistic models with a central energy density 1/10 that of BU1, this changes to $\sigma_{\max} = \Omega(1.93 - 1.03m)$ (with similar error-bars), close to what Lindblom and Ipser (1999) calculated and Brink *et al* (2004) found for Newtonian stars,

where $\sigma_{\max} \approx \Omega(2-m)$.

In the axisymmetric case a zero-frequency mode in the rotating frame has 0 Hz also for an inertial observer, it corresponds to the mid-point of the inertial mode frequency range. For non-axisymmetric perturbations the center of the spectrum is expected to shift to $-m\Omega$, which indeed appears to be the case in our results. The corresponding inertial mode spectrum for a specific azimuthal index $m > 0$ is however not completely symmetric since modes with different order n or harmonic indices ℓ have different frequency shifts. This shift is rather small for pressure modes. As the azimuthal index m can take arbitrarily large values, the inertial modes can, according to the above, reach arbitrarily large negative frequencies. Since these are equivalent to positive frequencies with a phase difference, the frequency range of inertial modes will overlap with that of pressure modes. An overview of the spectra for three different values of the azimuthal index m can be seen in Fig. 4.10.

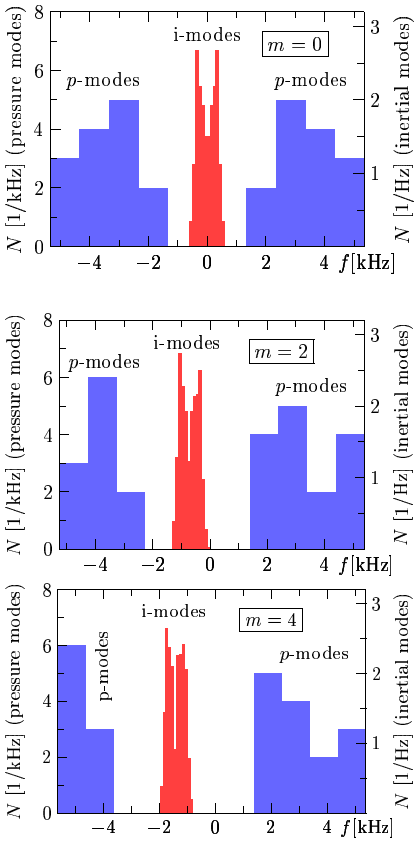

Figure 4.10: The histogram of both positive and negative solutions of the eigenvalue code for $m = 0, 2$, and 4. The values for the inertial modes (middle) are scaled differently for better presentation.

The oscillation frequencies are influenced not only by changes in the equilibrium configuration of the star, but also by other effects, such as the frame dragging at the surface and the center (Kojima & Hosonuma, 1999). These also scale linearly with Ω. Knowing the range of inertial mode frequencies as a function of the star's rotational rate in advance may be quite helpful for actual observations of gravitational radiation emitted by these oscillations. In the next section we search for individual modes, such as the fundamental r-mode.

4.3.1 Pressure modes

In table 4.6 we show the first pressure modes for the rapidly rotating model BU1 as in table 4.4; no $\ell = 0$ and $\ell = 1$ modes are present since we are looking at $m = 2$ perturbations. In this case we have to be careful when comparing results, since the work of Font *et al* (2001) considered axisymmetric perturba-

Table 4.6: The first two pressure modes for BU1 for a fixed θ-resolution and increasing r-resolution; the one to last row are the extrapolated values. The results by Font *et al* (2001) are being subtracted by $m\nu(1-C_{n\ell})$ and are shown in the last row; they include a standard deviation error of $\sim$ 15Hz due to numerical integration.

n_θ	n_r	$f_{\ell=2}$	$p^1_{\ell=2}$
10	10	1753	5086
	20	1574	4042
	25	1533	3947
	50	1443	3740
	∞	**1350**	**3520**
Font *et al* (2001)*		1330	3400

tions [8]. As known by theory (see eg (Unno *et al*, 1989)), rotation causes the m-degeneracy to be broken. A (polar) mode with frequency f_0 in a non-rotating star, changes to $f_i = f_0 - m\nu(1-C_{n\ell})$ $(+O(\nu^2))$ when rotation is switched on, where $C_{n\ell} = \frac{\int \rho r^2[2\xi_r\xi_h+\xi_h^2]}{\int \rho r^2[\xi_r^2+\ell(\ell+1)\xi_h^2]}$ can be determined (also numerically) from the mode's eigenfunction (ξ_r, ξ_h represent the displacement vectors in the radial and angular direction). The computed value for the f-mode is $C_{12} = 0.24$ which results in a 525Hz reduction of the frequency, and $C_{22} = 0.079$ for the p^1-mode, with a resulting 640Hz decrease in frequency (typical errors 0.02, ie. 15 Hz). The agreement is of the same order as before. The reason for the discrepancy is believed to lie with the finite resolution having a larger impact on the high-order modes.

In fig. 4.11 we show the eigenfunction of the fundamental pressure mode for m=2. This cannot be compared directly with any of the eigenfunctions of the previous section since there are different modes under consideration, namely for $m = 2$ and $m = 0$. We see that the eigenfunction is already described well with low resolution and the form does not change as more radial points are considered in the background. The θ-eigenfunction (right) is practically identical (after normalization) for all resolutions and very similar to the P_2^2 Legendre polynomial. In fig. 4.12 we show also δu_θ for the same mode. While the r-eigenfunction behaves like a power law throughout the star – like r^2 up to $\sim R/3$ –, the θ-eigenfunction resembles now $\partial_\theta P_2^2 = 3\sin 2\theta$, which is the leading order contribution of the expansion into spherical harmonic function for this polar mode (the next one being $P_2^3/\sin\theta$, see also the next subsection and eq. 4.14).

[8] For $\Omega = 0$ this does not make a difference.

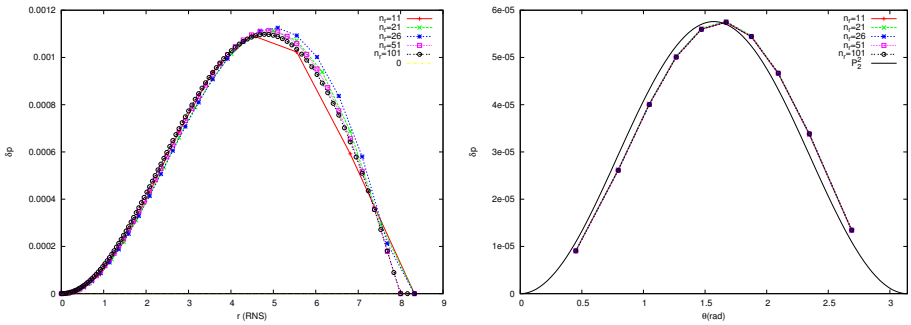

Figure 4.11: The r and θ parts of the eigenfunctions of the pressure perturbation for the $f_{\ell=2}$ mode of the BU1 model for several resolutions. The θ parts (bottom) are not distinguishable from each other and very close to P_2^2. The r eigenfunction is plotted at an angle of ~ 45 degrees, while the θ eigenfunction at the first non-zero radial point.

4.3.2 Identification of inertial modes

The task of identifying inertial modes is much more tedious than the study of the general properties of the frequency distribution. By definition (see section 1.1) the identification of a mode should be based on its eigenfunction. Since, however, the number of modes found are proportional to the product of number of points in both directions, an increasingly large number of eigenfunctions are to be checked. We can ease this search by concentrating on a range of frequencies where the modes of interest are expected to be. For p-modes this is well restricted (see eg. susection 2.3.2), but for inertial modes, only the fundamental r-mode has a well studied frequency (around 1.4ν). But even the uncertainty in the value of the latter (of about 10%) combined with the dense population of inertial modes, still leaves us several dozens up to a few hundred (depending on the resolution) modes to examine.

One other important distinction between p-modes and inertial modes – regarding their eigenfunctions and the mode identification – is the coupling of polar and axial contributions, which does not appear to be really strong for the p-modes, while for the inertial modes it can produce a rather complicated eigenfunction, departing significantly from the form of the leading order term and being rather a mixture of the first few (3-4) terms. Lockitch and Friedman (1999) computed the leading order terms of several modes in a Newtonian framework and expressed them as power series. Later Lockitch *et al* (2003) extended this by the use of general relativity, but did not present the explicit terms in their paper. What is important to note is that the resulting eigenfunction will not be just a sum of the individual (polar and axial) terms of all orders, but one has to calculate the contributions as they are scaled by the corresponding θ-behavior. So, for example, the θ-part of the velocity perturbation, will be (in

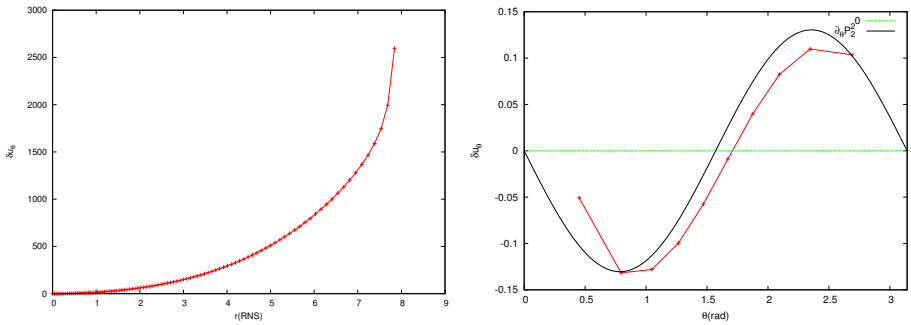

Figure 4.12: The r and θ part of the eigenfunctions of the θ component of the perturbed 4-velocity for the same mode as in fig. 4.11. Also shown with the θ-eigenfunction, the leading order term of the expected expansion in spherical harmonics and their derivatives, $3\sin 2\theta$ (see also text).

the notation of Lockitch and Friedman (1999))

$$\delta u_\theta \approx \Sigma_{k=0}^{n} \frac{1}{r}\left(V_{m+2k+1}\frac{\partial P^m_{m+2k+1}}{\partial\theta} + \frac{m}{\sin\theta}U_{m+2k}P^m_{m+2k}\right), \tag{4.14}$$

[9] where U_ℓ, V_ℓ are powers series of $x = r/R$ for the axial and polar contributions respectively. For δu_ϕ the corresponding expansion is:

$$\delta u_\phi \approx \Sigma_{k=0}^{n} \frac{i}{r}\left(\frac{mV_{m+2k+1}}{\sin\theta}P^m_{m+2k+1} - U_{m+2k}\frac{\partial P^m_{m+2k}}{\partial\theta}\right), \tag{4.15}$$

while for δu_r the series would include only polar terms:

$$\delta u_r \approx \Sigma_{k=0}^{n} \frac{W_{m+2k+1}}{r}P^m_{m+2k+1} \tag{4.16}$$

as also for δp with different functions $\tilde{W}$.

In figure 4.13 we show how δu_θ of Lockitch and Friedman (1999) looks like, along some characteristic coordinate values of our grid, for the $m = 2$ axial-led inertial mode with $\sigma = -1.51\nu$ ($k = 0.4669$). The terms that contribute to forming that eigenfunction are the axial vectors for $\ell = 2$ and $\ell = 4$ as well as the polar one for $\ell = 3$, ie. $\frac{2}{\sin\theta}U_2P_2^2$, $\frac{2}{\sin\theta}U_4P_4^2$ and $V_3\frac{\partial P_3^2}{\partial\theta}$ respectively. We see that although the function $U_2(x)$ is the leading order term, the r part of the eigenfunction is not dominated by its contribution. Moreover, we note that the r part of the eigenfunction can well cross the x axis along several angular directions. In contrast to the pressure modes, the θ part of the eigenfunction is different at different radial points; it also deviates significantly from $\sin\theta$ ($= P_2^2/\sin\theta$), especially at the outer parts of the star. This means that the

[9] n is theoretically extending to infinity but in practice truncated at some $\ell_{\max}$; in Lockitch and Friedman (1999) this is 4 for most modes considered

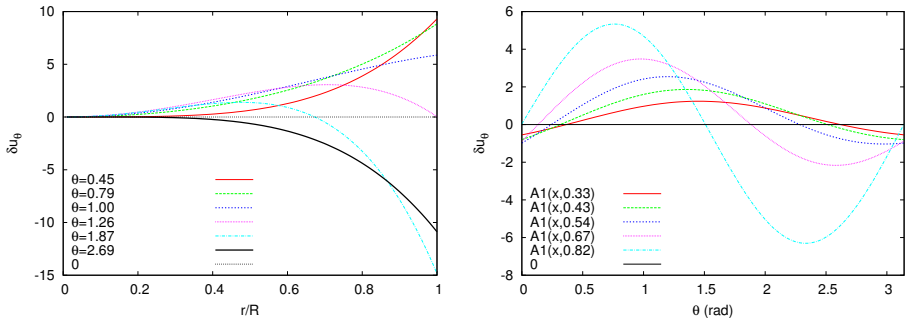

Figure 4.13: The r and θ eigenfunctions of the $\sigma/\Omega = -1.51$ axial-led inertial mode of Lockitch and Friedman (1999) along some characteristic directions in the star; for the r-eigenfunction (upper panel) along the angles on which our grid points fall: 0.45 rad, 0.79 rad, 1 rad, 1.26 rad, 1.87 rad and 2.69 rad (two more angles at each of the last two θ-spaces were left out since the corresponding change in the eigenfunction is small and the figure would be overcrowded); for the θ-eigenfunctions at $\frac{r}{R} = 0.2$, 0.79, 1, 1.26, 1.87, which is again a selected subspace of the radial coordinate for our lowest resolution ($n_r = 11$).

identification of such a mode, based on δu_θ, should preferably take place at points were the expansion of the eigenfunctions into power series of decreasing order is a good approximation. That would thus be close to the center of the star (for the θ part of the eigenfunction) and close to the rotational axis (for the r part). Due to the low θ-resolution used throughout this work, the latter would be at angles of about $(\pi-)0.45$ rad. Still, in the case of modes with similar profiles, the identification would be very hard, even with a quantification of the similarity to the individual contributions (eg. by fitting the resulting points of the profile with a function like eq. 4.14). High rotation rates can cause even more confusion, and a mode should be identified first for slower rotating models of a sequence. The compactness of the corresponding model should not cause additional complications, as it has minor effect on the contributing terms (and thus the overall eigenfunction) (Lockitch *et al*, 2003).

In our results several modes seem to have profiles similar to what we see in fig. 4.13. We can be confident that expected solutions appear in our results, we do however not proceed in searching for other modes apart from the fundamental r-mode, since even the second order inertial modes hardly produces any gravitational wave emission (Lockitch *et al*, 2003) and is therefor of minor astrophysical interest.

4.3.3 The fundamental r-mode

The procedure followed above for predicting the eigenfunction, does not apply in the same way for the fundamental r-mode, since in Newtonian description the mode has just a single axial contribution, and thus does not mix with higher or-

Table 4.7: The frequencies in Hz of our best candidate for the fundamental r-mode for several resolutions of the BU1 (left) and BU6 (right) models.

n_θ	n_r	r-mode(?)	n_θ	n_r	r-mode(?)
10	10	515.6	10	10	1146.9
	20	504.1		20	1167.9
	25	501.6		25	1166.7
	50	496.7		50	1170.2
	100	494.6		100	1174.2
	∞	**492.0**		∞	**1175.7**

der ones (Lockitch and Friedman, 1999). In this framework, the r-eigenfunction would be a single power of r, while the θ-eigenfunction for δu_θ would, at any radial point, be proportional to $P_2^2/\sin\theta$. Lockitch *et al* (2003) examined the coupling with higher terms introduced by general relativity and found even the first few order terms to be less than an order of magnitude smaller than the first order one. Although the explicit terms are not available, we expect the $\frac{1}{r}U_2P_2^2/\sin\theta$ term to dominate the eigenfunction of δu_θ both in radial and angular direction; For δp the leading order term will be P_3^2 since the axial parts are zero for scalar perturbations.

Based on this we performed a search among the inertial modes given from our eigenvalue code. We concentrate on the θ part of the perturbed velocity, since this is the variable that is expected to be excited the most and does also appear to be larger in magnitude relative to δu_ϕ, δu_r and δp. Depending on the model's compactness and its rotation rate the frequency of the r-mode is expected to lie within $\sim 1.2\nu$ and $\sim 1.5\nu$ (Yoshida *et al*, 2005), which is also the range at which we looked. The restrictions for the mode's δu_θ not to cross the x-axis, to have a r-behavior like r^2 and a θ-behavior like $\frac{P_2^2}{\sin\theta} \sim \sin\theta$ were checked manually for all modes lying in this range. We focused our search at the θ part of the eigenfunctions as they appear close to the center and the r parts along a preferred angle (see above, subsection 4.3.2) of ~ 2.49 rad, but extended that also to different coordinate values . We first looked at the model for the (relatively) slowly rotating star, BU1 and then at the faster one, BU6.

The above criteria were not strictly met for any mode of BU1, but we did find an inertial mode at every resolution that has a very similar behavior. We show the r and θ parts of the eigenfunctions of δu_θ and δp in figure 4.14 and the frequencies of the mode for every resolution in table 4.7. The radial profile of δu_θ reasonably resembles r^2 for all resolutions. Some large-scale deviations are probably due to contributions from higher order terms, while the small-scale deviations, that become more obvious for higher resolution, might be due to numerical contamination from solutions with similar frequency and more com-

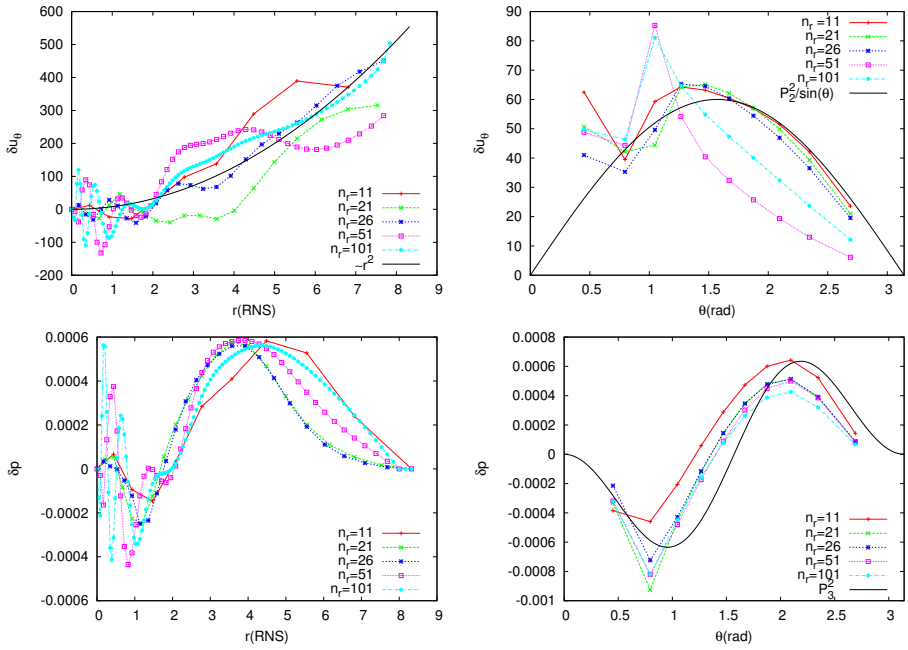

Figure 4.14: The best candidate for the r-mode for the model BU1. The r parts of the eigenfunction are seen at the last angular point ($\theta = 2.69$rad) while the θ ones are seen at the first non-zero radial point.

plicated profile. The angular profile of δu_θ resembles well the leading order term of the expected expansion in Legendre polynomials ($P_2^2/\sin\theta$), with deviations being stronger at the left part of the diagram[10]. For $n_r > 50$ $\delta u_\theta(\theta)$ deviates more from $\sin\theta$, still keeping however the rough form of the lower resolutions. The eigenfunctions of δp were not used for the search of the mode, but are illustrated here for consistency. The radial part has for all resolutions a form that resembles the no-node r-eigenfunctions of the fundamental pressure modes (see eg. fig. 4.11) apart from some small-scale deviations that –again– appear at small r. The θ-eigenfunction on the other hand, has a more clear form, which resembles well a P_3^2 Legendre Polynomial, the expected leading term of the expansion of a axial-led scalar function (see subsection 4.3.2); the form is disturbed only at points close to the left boundary.

For BU6, the search for the r-mode was even more tedious, apparently due to the increased mixing of contributions (see above). We still find a mode behaving similarly to the mode of BU1 that was identified as r-mode, but with even weaker fulfilling of the preset criteria. Its eigenfunctions are plotted as before in fig. 4.15 and the corresponding eigenfrequencies in table 4.7. The main differences of the eigenfunctions, compared to the ones of fig. 4.14 is the larger long-scale deviation

[10]The θ-derivatives appearing in the equation for $f_2 \sim \delta u_\theta$ are discretized with left-hand-sided differences, making it more sensitive to the boundary conditions at the left ($\theta \approx 0$).

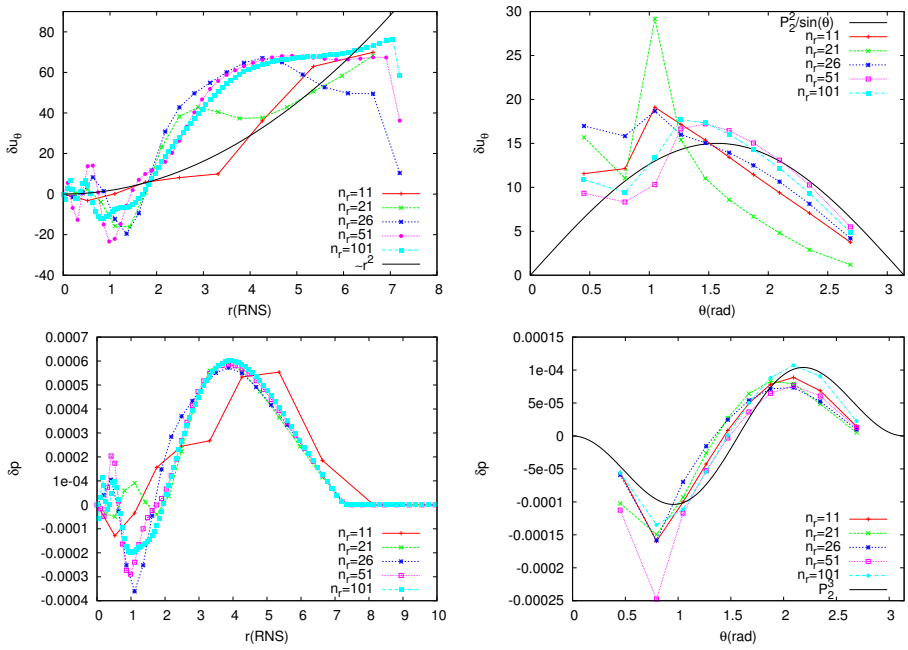

Figure 4.15: As in figure 4.14, but for the model BU6.

from r^2 for $\delta u_r(r)$; this could be the result of a stronger contribution from the higher order terms due to increased rotation. This is, however, not seen in the eigenfunctions that Yoshida *et al* (2005) publish for δu_θ of the r-mode that they computed, although in their analysis only that single mode was derived.

The frequency 'evolution' with resolution, on the other hand, does not follow a nice $1/r$ convergence any more (χ^2/dof=31.1) as it did for the BU1 model. Also the extrapolated frequency of $\sigma/\nu = 1.48$ (as well as the individual ones) are higher than the corresponding one for BU1, which is in contrast to what is found by Yoshida *et al* (2005) for a series of models for the r-mode[11].

The numerical limitations of our code might be able to explain the discrepancy and offers three explanations for the differences with the results of Yoshida *et al* (2005):
Both modes are indeed the r-mode of each model, and the differences in the frequencies, as well as in the eigenfunctions with the results of Yoshida *et al* (2005) are due to the low resolution, especially in the θ-direction. For rapidly rotating models (and thus increased deviation from spherical symmetry) more angular points (together with high radial resolution) are needed to sufficiently solve the problem. Memory-limitations did not allow us to perform such calculations.

[11]The models used by Yoshida *et al* are different than the ones used here, so no direct comparison between the mode frequencies can be made. Still, for their sequence of models c and d (that resemble ours the most), the decrease of the r-mode frequency with rotation energy $T/|W|$ is found to be $\sigma/\Omega \approx 1.41 - 1.95\frac{T}{|W|}$ and $\sigma/\Omega \approx 1.51 - 1.36\frac{T}{|W|}$

One other possibility is that, while the mode for the slower rotating model BU1 is closer to what we expected and can indeed be identified as the r-mode, the mode identified for the BU6 model is not the mode we were looking for. Since the eigenfunctions, on which the search was based, are in this case quite messy, no unique characterization of a mode can be made, hindering us from following such for several resolutions. This means that the r-mode for BU6 would be at somewhat lower frequencies[12].
The last possibility is that both the modes that we pointed out do not correspond to the r-mode; since no other mode with better properties was found among our solution, that would mean that the r-mode is not present in results. This possibility cannot be excluded since the presence of a continuous spectrum of inertial modes and the occasional elimination of the r-mode through that, was suggested in some slow-rotation analyses (see sec. 1.1).

The latter two possibilities cannot be definitely answered through this approach. Not just because a mode calculation cannot resolve the question of continuous spectrum; it is the complexity of the boundary value problem and its sensibility on the conditions implied (especially on the angular directions) that allows to consider minor changes revealing some additional physical conditions and results (see also subsections 2.3.1, 2.3.2). Although the axis has some particular problems (singularity of the variables there), its inclusion in the numerical grid – possibly with a different choice of variables – may allow a more complete description of the boundary conditions there.

[12]We indeed see a mode at $\sigma \approx 1.35\Omega$ with similar properties, but for $n_r > 26$ the picture seems to brake.

Chapter 5

Conclusions

We have presented the first numerical calculation of oscillation frequencies of rapidly rotating relativistic stars for both axisymmetric and non-axisymmetric perturbations, using the relativistic Cowling approximation.

For the polytropic equations of state that we have employed here, we found an infinite set of pressure modes with a range of frequencies bounded only from below at about 2kHz. In addition, there is a presumably infinite set of solutions at lower frequencies in a well defined range which corresponds to inertial modes. In the axisymmetric case ($m = 0$) this frequency range is symmetric around zero. It extends to a maximum frequency which depends linearly on the star's rotation rate ν_{star} and approaches $2\nu_{star}$ for less relativistic stars. For non-axisymmetric perturbations, oscillation frequencies shift towards negative numbers. This affects pressure modes only slightly, while the inertial modes now all have frequencies below zero.

It is not clear whether this low-frequency part of the spectrum is discrete or continuous, or a combination of both. The dense and somewhat uneven distribution of the eigenvalues is an indication that the actual structure of the physical spectrum may be quite complicated. Further investigation is needed into the question how a spectrum with a continuous part can be studied numerically. Furthermore, explicit time evolution of perturbations of the same configurations could provide an independent means of studying their spectrum and checking the results we have presented here.

Inside the dense inertial mode spectrum, individual modes could still be identified, with a mode resembling the expected properties of the fundamental r-mode, being found at $\sigma/\Omega = 1.41$ for a slowly rotating neutron star and at 1.48 at about half the break-up frequency. Some uncertainties, however remain, due to the deviations from the expected form of the eigenfunction of δu_θ and the increase instead of decrease of the frequency with increasing rotation rate.

The numerical procedure definitely affects the accuracy of the results. One can observe this in the eigenfunction, where deviations close to the boundary are stronger (see subsection 4.3.3) as well as an overall shift of the eigenfunctions along the θ axis. An increased resolution in both angular and radial direction

could resolve this, but requires more computational memory than available.

Applying realistic equations of state requires only slight modification of the code and will shift the frequencies to some extent, but the overall picture should remain the same. The effect of a non-barotropic equation of state on the inertial mode spectrum presents a very interesting question for further study.

Finally, for an accurate calculation of the oscillation frequencies, the disposal of the Cowling approximation will be necessary. This is important not just to avoid deviation of the calculated frequencies introduced by the Cowling approximation, which we expect to be small, but also to ensure the consistency of the problem (see Section 1.1). The major problem lies not in the perturbation equations becoming more complex, but in defining the boundary conditions in the spacetime outside the star. Observation of potentially unstable modes with the now-operational gravitational-wave detectors is possible only if precise knowledge of these modes is available as a basis for the analysis of the gravitational wave data.

The oscillation mode problem for rapidly rotating stars has just started giving results, and is definitely not fully solved yet. This work, together with some recent articles, fill some of the last pieces of a puzzle that has long been started. A few more pieces are about to follow and the method presented here can contribute to clarifying important issues, especially regarding the full set of solutions and not just a few individual modes. The point where we will know how real these results are, is not far away.

Part II

Quasi-periodic oscillations in X-rays

Chapter 6

kHz quasi-periodic oscillations from Circinus X-1

As we saw in part I, inertial modes in the fluid of rotating neutron stars have frequencies of the order of a few hundred Hertz and can become unstable. Next to the fascinating perspective of detecting such through gravitational waves, it is also possible that the astronomical analogue of neutron stars – pulsars– shows similar non-radial oscillations at their outer layers through electromagnetic radiation. Radio pulses have been considered to be carrying the signature of such modes (Fender *et al*, 2005) but oscillations in the x-ray spectrum seem like a better candidate (Bildsten *et al*, 1998).

6.1 Introduction

Low mass X-ray binaries (LMXBs) often exhibit quasi-periodic oscillations (QPOs) in their X-ray flux. These QPOs show dramatic changes in their frequency and coherence as a function of a system's location in the X-ray color-color diagram. If the LMXB is a Z source the QPOs generally increase in frequency and in sharpness as the source moves from the horizontal branch to the normal branch and eventually the flaring branch, which is also the path along which the mass accretion rate is believed to be increasing, at least on short time scales. For atoll sources the analog sequence of states is extreme island $\rightarrow$ island $\rightarrow$ banana state. QPOs reaching up to about a kHz (kHz QPOs) are often found along the horizontal branch and upper normal branch for Z sources and in the island state as well as the lower left banana state the for atoll sources. In, so far, 19 cases of LMXBs containing NSs, two kHz QPOs have been seen simultaneously (twin kHz QPOs) with a frequency separation $\Delta\nu$ of several hundred Hz. If the the spin frequency of the NS, ν_s is known, $\Delta\nu$ is always found to be roughly

equal to ν_s or half of it. The frequencies of the twin kHz QPOs are tightly correlated to each other, following a relation that is nearly identical even when switching to other sources (van Straaten *et al*, 2005; Psaltis, Belloni & van der Klis, 1999). Both kHz QPO frequencies also correlate with the frequency of the low-frequency QPO [1], the hump [2] frequency and the break frequency [3] (van Straaten *et al*, 2005). Two high frequency QPOs have also been observed in LMXBs containing a black hole (BH) candidate – although only in two cases simultaneously. These have fixed frequencies different in each source and a constant frequency ratio consistent with 2:3.

Numerous models attempt to explain the nature of the kHz QPOs and describe their correlations. Some refer to a blob formed and orbiting inside the accretion disc, either self-luminous or scattering light, or one producing a hot-spot on the NS-surface by the in-fall of matter from the inner edge of the disc. These models produce a beaming modulation. With $\nu_\phi = \sqrt{GM/(4\pi^2 r^3)}\left(1 + j\,(r_g/r)^{3/2}\right)^{-1}$ the orbital frequency of a particle in an equatorial circular orbit in Kerr spacetime around a point particle [4] with mass M and angular momentum J ($r_g \equiv GM/c^2, j \equiv Jc/GM^2$), the radial and epicyclic frequencies in slightly tilted and eccentric orbits will be $\nu_r \approx \nu_\phi(1 - 6r_g/r)^{1/2}$ and $\nu_\theta \approx \nu_\phi\left(1 - 4j\,(r_g/r)^{3/2}\right)^{1/2}$ (see e.g. van der Klis, 2004). In the relativistic precession model (Stella & Vietri, 1999) as well as in the sonic-point model (Lamb & Miller, 2003) the upper kHz QPO is identified with ν_ϕ, while the lower kHz QPO is interpreted in the first case as due to the periastron precession $\nu_\phi - \nu_r$ and in the second case the beat between ν_ϕ at the sonic radius and the spin (approximately $\nu_\phi - \nu_{spin}$ or $\nu_\phi - \nu_{spin}/2$ depending on conditions at the spin resonance radius where the beat emission is generated). Kluźniak & Abramowicz (2001, 2003) suggest a fixed ratio of QPO frequencies in NSs such as is seen in BHs, resulting from resonance frequencies in the disc. Models related to orbital motion, in general, have difficulties explaining the modulation or the damping of the oscillations. A maximum frequency according to such models would be the orbital frequency at the inner-most stable circular orbit (ISCO) of the compact object, which scales inversely with its mass M, e.g. $\nu_{ISCO} \approx (c^3/2\pi 6^{2/3} GM)(1 + 0.75j)$ for Kerr spacetime. Neutron Star oscillations are also considered among the possible generators of the QPOs (Bildsten *et al*, 1998). There are several difficulties in this scenario, mainly including the rapid change in frequency of the QPOs (which could not correspond in a similar change in the frequency of a specific mode – although possibly to different ones). For an extend review on timing features of LMXBs and QPO models see van der Klis (2004).

Circinus X-1 Circinus X-1 is a galactic X-ray source positioned in the galactic plane at a distance of ∼4 to 8 kpc (Iaria *et al*, 2005; Glass, 1994; Goss & Mebold,

[1] Sharp QPO peak in the 1-60Hz range, represented by L_{LF}.

[2] Broad noise component or QPO with usually a somewhat higher characteristic frequency than the L_{LF}, represented by L_h.

[3] Broad noise component in the 0.01-20Hz range, represented by L_b.

[4] Which approximates the the metric around a NS

1977). From optical and infrared observations, a subgiant star of $3 - 5M_{\odot}$ was identified which is thought to be in an eccentric orbit ($e \sim 0.7 - 0.9$) with the compact object (Johnston *et al*, 1999). The strong radio emission of the source (see e.g. Fender *et al*, 2005), relativistic jets (Fender *et al*, 2004) and the hard X-ray emission and strong X-ray variability from the system (Samimi *et al*, 1979; Jones *et al*, 1974), resemble typical properties of black hole candidates. However, Type-I X-ray bursts seen in 1986 (Tennant *et al*) from the field of Circinus X-1 classified it as a probable NS, with later spectroscopic analysis (Maisack *et al*, 1995; Done & Gierlinski, 2003) supporting this thesis. At lower intensities the source was reported to exhibit atoll-source behavior (Oosterbroek *et al*, 1995), while subsequent observations showed a Z-source-like track (Shirey *et al*, 1999). On the horizontal branch of this track, Shirey *et al* (1996, 1998) found a narrow QPO moving from 1.3 Hz to 32 Hz. The frequency of this QPO was strongly correlated with the break frequency at lower frequencies and a broad peak ranging from 20–100 Hz. No 6-Hz-QPOs were seen on the normal branch and no (twin) kHz QPOs were reported so far.

In this work we concentrate on the high frequency part of the power spectra of Circinus X-1 and perform an extensive survey for kHz QPOs. We find that twin kHz QPOs occur in Circinus X-1. We describe our methodology in Section 6.2, present our results in Section 6.3 and comment on them and on theoretical models in Section 6.4.

6.2 Observations and Analysis

We used the publicly available data [5] of Circinus X-1 obtained with the proportional counter array (PCA) on board Rossy X-ray timing explorer (RXTE), from March 1996 till January 2005. They correspond to 21 observation IDs (listed in Table 6.1) and contain in total about 2 Msec of data.

The source was observed with 13 different combinations of instrumental modes covering the full energy range (channels 0–249, effective energy range 3-60keV), and one more starting from channel 8 (3.68 keV) with which 21 observations were taken in 2003 (cycle 8), where the intensity, however, was very low (below 1000c/s/PCU, between 0.22 and 0.42 Crab) and from which we eventually did not include any in our final analysis. Every observation was divided into time segments of 16, 64, 128 or 256 sec, depending on the time resolution such that they contained 1048576 points. These were Fourier-transformed, added together and averaged to give the power spectrum of each observation.

We then selected the observations that could be described by more than one Lorentzian. Power spectra that showed broad plateau-like features at low frequencies ($\sim$ 10Hz) and those showing no appreciable power at all were not of our interest and are not included in this analysis. In total we fitted 119 power spectra (PSa) from the, in total, 497 observations. The fits were made without any reference to expected features, including all significant Lorentzians that could be fitted.

[5] At the start- time of this project, February 2005.

Table 6.1: The IDs of the RXTE-observations used in this analysis.

obs-id
10068-08
10122-01
10122-02
10122-03
20094-01
20095-01
20097-01
20415-01
30080-01
30081-01
40059-01
50136-01
60024-01
60025-01
70020-01
70020-02
70020-03
70021-01
80027-01
80114-01
90025-01
90426-01

Since this work concentrates on kHz QPOs, we need to be very careful when subtracting the deadtime modified Poisson noise power. We used the usual Zhang function (Zhang *et al*, 1995) to describe the Poisson spectrum, but instead of the approximate deadtime value $t_d = 10\mu s$ (Zhang *et al*, 1996; Jahoda *et al* , 2005) or one the often used of $8.5\mu s$ (Klein-Wolt *et al*, 2004), and either the nominal $t_3^{VLE} = 150\mu s$ (Zhang *et al*, 1996) or the calibrated $t_3^{VLE} = 170\mu s$ (Jahoda *et al* , 2005) very large event (VLE) deadtime value of the satellite [6], we calculate these parameters directly from our observations, by fitting the Zhang function to data where no source contribution is expected (see Appendix C), $t_d = 8.87\mu s, t_{VLE-3} = 162\mu s$, and used those when estimating the Poisson spectrum. This method does not alter the significances of the twin kHz QPOs.

After subtracting the noise, we renormalized the power spectra to rms squared and plotted them in the power $\times$ frequency representation. For the fitting we used a multi-Lorentzian model (plus a power law at low frequencies when needed), in the ν_{max} representation described in Belloni *et al* (2002). To obtain the centroid frequency ν_0 , we used the expression $\nu_0 = \frac{2Q\nu_{max}}{\sqrt{1+4Q^2}}$, where Q is the

[6] For the VLE setting '2'.

quality factor defined as $Q = \nu_0/FWHM$. Since all Lorentzians for which we applied this conversion are sharp-peaked ($Q \geq 1$), the errors computed for ν_{max} are also a good representation for ν_0. For the twin kHz QPOs, we recalculated the ν_0-errors by separately fitting with centroid frequencies, and typically found 5% (usually $< 1Hz$) difference. For sharper QPOs, as the L_{LF}, this difference is much smaller.

We use the 16-s time-resolution Standard 2 mode to calculate X-ray colors as in Altamirano *et al* (2005). The hard color is defined as the ratio between count rates in the 9.7–16 keV and 6–9.7 keV range, while the soft one for 3.5–6 keV/2–3.5 keV. Dropouts were removed, background was subtracted and deadtime corrections were made. In order to correct for the gain changes as well as the differences in effective area between the PCUs themselves, we normalized the colors by the corresponding Crab color values (see Kuulkers at al., 1994; van Straaten *et al*, 2003) that are close in time but in the same RXTE gain epoch. All active PCUs were used to calculate the colors.

6.3 Results

In 80 of the 119 fitted observations we found a QPO which we interpret as a kHz QPO (see subsection 6.3.2) while in 8 of them we found a significant ($> 3\sigma$) second one. A second kHz QPO, with a significance between 2.5σ and 3σ, could be fitted at 5 more cases. We discuss whether the latter (as well as the former) are real or not in subsection 6.3.1. All the significances quoted are single-trial.

A typical power spectrum exhibiting twin kHz QPOs is the one of 20094-01-01-01, shown in plot E of Figure 6.1. The low-frequency QPO is the prominent narrow feature seen in all 119 observations – sometimes as a double peak. The break frequency was also seen in all but three cases while a hump component was present in more than half (69) of the power spectra. Power laws were needed only in nine cases, and always only produced appreciated power below ∼1Hz.

The soft and hard colors of all observations are displayed on the color-color diagram (CCD, Figure. 6.2, left-hand panel). The large majority of the observations form a narrow track, with all the observations that we fitted (except of a very late one, 90025-01-01-05) falling on there. This track corresponds to the one that Shirey *et al* (1999) show in their color-color diagram (their Figure 2), despite the slightly different definition of the colors. There is an indication for two sub-branches emerging at the upper end of the main track, which appears also if plotting the colors for every 16sec. A hardness-intensity diagram is provided in Figure 6.3 (left-hand panel). The vast majority of the PSa that showed a low-frequency QPO (and which we fitted) had intensities about 1 Crab.

Suspecting that the frequencies of the several QPOs are related to each other (see Section 6.1) we plot all features in a frequency-frequency diagram (Figure 6.4). Indeed the points can be easily separated into five groups of corresponding frequencies. Slightly above the low frequency QPO (identified as such as the most significant feature in our PSs) but clearly separated from it we see a group of points associated with the hump frequency. Parallel to those and at somewhat

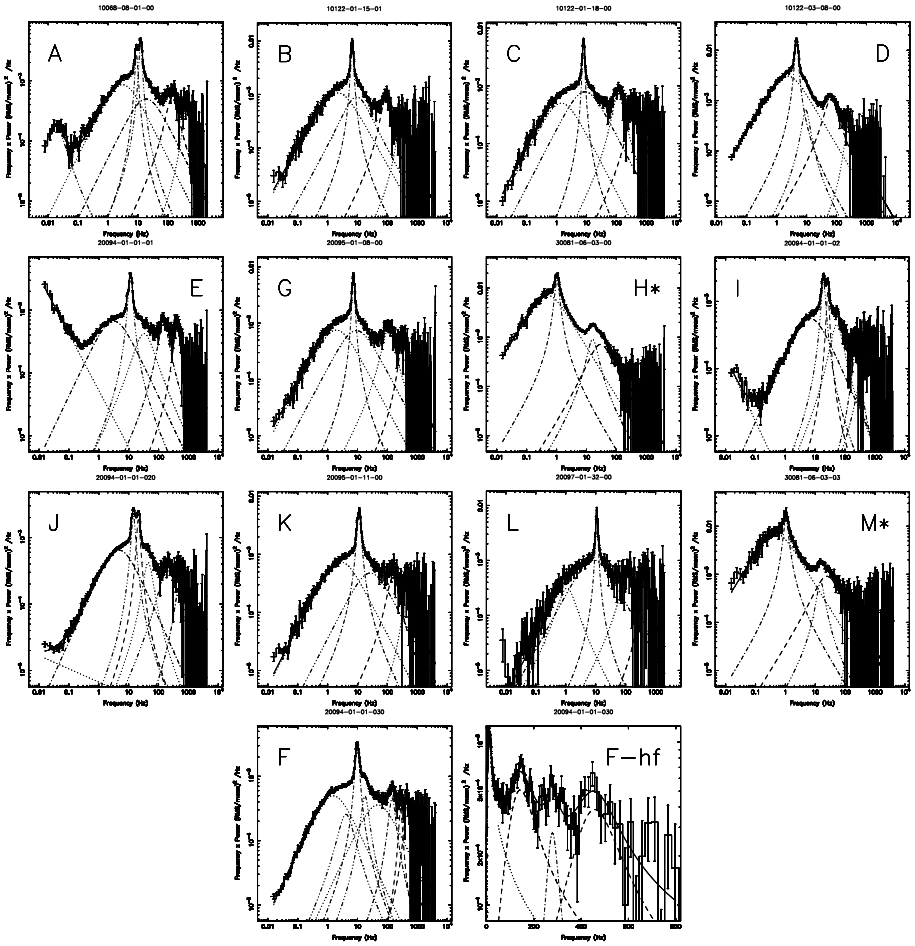

Figure 6.1: Power spectra and fit functions in the power spectral density times frequency representation for the 11 observations showing twin kHz QPOs. The curves mark the individual Lorentzian components of the fit. The last row shows the PS containing three kHz QPOs with a blow-up at high frequencies. For simplicity each observation is marked with a letter, while the ones with an asterisk will eventually be identified as showing a single kHz QPO rather than two (subsection 6.3.1). The scaling of the frequency axis in the latter is linear.

higher frequencies there is an almost continuous series of points extending up to about 250 Hz. Another group of points above these has similar characteristics although less dense and extends up to about 500 Hz. From the large frequencies to which they extend and their, over a decade, variability, we identify these as kHz QPOs. We conclude that the former points correspond to lower kHz QPOs and the latter to upper kHz QPOs. The first ones coincide with the 'low kHz QPOs' reported by Psaltis, Belloni & van der Klis (1999), the rest extending though up to several hundred Hz. Finally, there is a group of points below the low-frequency QPO, less confined on a line, which according to their frequency range we identify as the break frequency. This component does not form the focus of our analysis and may well be a mix of more than one noise components. We elaborate on each category of QPOs in the following.

6.3.1 Twin kHz QPOs

All the observations that showed twin kHz QPOs with significance of more than 3σ for one of the kHz QPOs, and at least 2.5 for the second are listed in Table 6.2; their PSa are shown in Figure 6.1. From the right-hand panels of Figures 6.2 and 6.3 we see that the latter group lies inside the range of colors and intensities of the former group. Also the QPO frequencies (Figure 6.4) are in the same range and the correlations seem to hold for both groups of points. It is safe thus to include the 5 observations with significance of the second kHz QPO between 2.5σ and 3σ among the observations with twin kHz QPOs, assuming that the statistics were poor in these cases.

The two twin kHz QPOs seen in cycle 3 (PSa H and M of Figure 6.1) have frequency separations small compared to their widths and although the fits are better with two high frequency features, a single one also describes the PS at high frequencies quite well. Since these frequencies would be by far the lowest kHz QPO frequencies ever found, we need to test the existence of two features rather than one. If we look at the frequency- frequency diagrams of Figures 6.6 and 6.4, the two pairs seem to diverge significantly from the picture and position of the other twin kHz QPOs and do not seem to follow the correlation of the others. Also from the position of these observations in the CCD (Figure 6.2, right panel) the two cycle 3 observations seem to be separated from the rest; although their intensities are similar (Figure 6.3). The rms amplitudes of the kHz QPOs do not seem to follow the almost linear decrease of the lower kHz QPOs of the other pairs (Figure 6.5). We conclude that the second kHz QPO appearing in PSa H and M is probably not real, and the PSa should be fitted with a single Lorentzian at high frequencies. Two intermediate observations with similar PSa best fitted with a single kHz QPO support this thesis.

We remain thus with 11 twin kHz QPOs. We plot the centroid frequencies of these QPOs versus each other in Figure 6.6 and their frequency separation against the frequency of the upper one in Figure 6.7. The Circinus X-1 points above could be described with a linear relation, but the match with twin kHz QPO frequencies from other LMXBs containing a NS strongly suggests a power law relation. The best fit is a power law of $\nu_u = 15.7(\pm 6.3) \times \nu_\ell^{0.67(\pm 0.08)}$

Table 6.2: All observations showing twin kHz QPOs with significances more than 3σ for both kHz QPOs (upper 8), and more than 3σ for the one kHz QPO and at least 2.5σ for the other (lower 5). Listed are, apart from the observation-ID and centroid frequencies with their error-bars (in Hz), the rms amplitudes with their error-bars (in percent), as well as the quality factors with the corresponding errors. In one case a 3rd kHz QPO is also reported with its error, with a significance of 2σ. The two observations marked with $*$ will eventually be considered to have a single kHz QPO instead of two (see Subsection 6.3.1).

obs-id	$\nu_\ell(\pm)$	% rms($\pm$)	Q($\pm$)	$\nu_u(\pm)$	% rms($\pm$)	Q($\pm$)
10068-08-01-00	122.3 (7.2)	2.61 (0.19)	0.9(0.2)	406.6 (32.8)	1.74(0.24)	1.8(0.7)
10122-01-15-01	83.1 (2.5)	2.94 (0.15)	1.3(0.2)	280.6 (32.0)	1.69(0.32)	1.6(0.9)
10122-01-18-00	106.5 (2.5)	2.93 (0.13)	1.2(0.1)	358.6 (42.1)	2.28(0.25)	0.9(0.4)
10122-03-08-00	56.1 (1.3)	3.88 (0.11)	0.8(0.1)	229.2 (17.5)	1.41(0.24)	2.1(1.2)
20094-01-01-01	136.5 (5.4)	2.65 (0.21)	1.1(0.2)	403.8 (17.1)	2.08(0.19)	1.9(0.5)
20094-01-01-030	127.6 (3.6)	2.53 (0.12)	1.0(0.1)	445.0 (20.2)	1.60(0.24)	1.8(0.5)
($\hookrightarrow \nu_3$)	277.8 (7.1)	0.87 (0.23)	5.5 (5.3)			
20095-01-08-00	97.5 (2.7)	3.13 (0.12)	1.0(0.1)	311.2 (19.8)	1.93(0.21)	1.8(0.5)
30081-06-03-00*	14.8 (0.2)	3.17 (0.35)	1.2(0.1)	18.4 (3.3)	3.95(0.33)	0.4(0.1)
20094-01-01-02	225.8 (17.5)	1.24 (0.28)	1.8(1.0)	505.2 (51.4)	1.65(0.22)	1.5(0.5)
20094-01-01-020	156.7 (21.6)	2.37 (0.26)	0.6(0.2)	496.8 (60.7)	1.47(0.33)	1.3(0.6)
20095-01-11-00	137.4 (5.4)	2.19 (0.39)	1.1(0.3)	438.1 (38.2)	1.47(0.31)	2.0(1.3)
20097-01-32-00	99.8 (25.7)	2.74 (0.40)	0.8(0.5)	418.7 (48.0)	2.03(0.43)	2.6(1.6)
30081-06-03-03*	14.6 (0.4)	2.46 (0.58)	1.6(0.5)	13.1 (3.1)	4.57(0.39)	0.3(0.1)

($\chi^2/dof = 2.04$). A linear best fit $\nu_u = 115.31(\pm 35.95)\nu_\ell + 2.25(\pm 0.31)$ $\nu_u = 110.54(\pm 33.45)\nu_\ell + 2.30(\pm 0.28)$ does not fit better than the power law ($\chi^2/dof = 2.48$) and diverges significantly from the points of other sources at higher frequencies. A constant ratio of $\nu_u/\nu_\ell = 3.18(\pm 0.11)$ is excluded at the ($\chi^2/dof = 4.78$) significance level. The range of twin kHz QPOs reaches the lowest frequencies observed so far in LMXBs containing neutron stars.

One of the power spectra showing two kHz QPOs with significances higher than 3σ also has a marginally significant (2σ) third kHz QPO, with its centroid frequency being 9% larger than (and 3.4 σ different from) twice the first kHz QPO frequency, and 14% smaller than (and 5.5 σ different from) the frequency separation of the two. This PS (F of Figure 6.1) could be better (>99% confidence level, F-test) fitted with two Lorentzians at frequencies below L_{LF}. In that case the 3rd kHz QPO exceeds 3σ (with the kHz QPO frequencies staying roughly unchanged). Since we restrict ourselves to a unified description for all power spectra throughout this work, we adopt the results of the original fit for our further analysis, but exceptionally take this low-significance QPO into

account as a possible signature of the second harmonic of the lower kHz QPO (see Section 6.4).

A remarkable fact is that all observations showing twin kHz QPOs had very similar intensities, as seen at the hardness-intensity diagram (HID, Figure 6.3). All but one (E) had intensities ranging in just between 2545 and 2770 c/s/PCU, or 1.025–1.115 Crab. The one exceptional case (with 1991 c/s, 0.787 Crab) had the highest hard and soft colors among the observations with twin kHz QPOs and kHz QPO at all (0.693 and 1.496 respectively, the upper right point in the CCD, Figure 6.2).

6.3.2 kHz QPOs

Apart from 11 twin kHz QPOs we observed 69 single ones, forming one of the largest samples in LMXBs. All the single kHz QPO points show a remarkable correlation with the L_{LF} (Figure 6.4). Only the two points at the upper right end of the diagram seem to diverge from the line more than one sigma. Since these seem to fall, instead, on the line for the upper kHz QPO, and because a less significant feature is in those power spectra present at frequencies consistent with a lower kHz QPO, we classify these two QPOs as upper kHz ones, with the lower kHz QPO remaining formally undetected due to statistics. This is consistent with the decrease in rms seen for the lower kHz QPOs with increasing frequency (Figure 6.5). The least squares power law fit for these points gives $\nu_\ell = 19.41(\pm 0.61) \times \nu_{LF}^{0.74\pm0.02}$ ($\chi^2/dof = 22.85$).

The quality factors of the kHz QPOs were typically about 1. Due to the relatively large uncertainties in these values as well as in the frequencies, no conclusions could be drawn regarding the correlation among them.

6.3.3 Other QPOs

The frequency of the hump seems to correlate also very well with the peak frequency on a line consistent with $2 \times \nu_{LF}$ (a least square fit gave $\nu_h = 1.79(\pm 0.24)\nu_p^{1.00\pm0.05}$) ($\chi^2/dof = 68.2$), which indicates it being a harmonic of the low frequency QPO. For the break frequency on the other hand, there does not seem to be a single correlation describing all the points well. Since this work mainly concentrates on kHz QPOs, the PS-fits might have been less accurate at low frequencies (see earlier in this section). The presence of two parallel groups is considered as possible, indicating that in some case two break frequencies could be fitted instead of one. This seems e.g. to be the case in PS F (subsection 6.3.1). More work in that direction is needed to resolve this issue. An increase of the break frequency for increasing L_{LF}-frequency is in any case evident.

6.4 Discussion

We discovered for the first time twin kHz QPOs from Circinus X-1. In 8 observations both kHz QPOs were significant ($> 3\sigma$) while in 5 observations one of the two had significance more than 2.5 and were accepted as real based on their similarities in the colors and frequency correlations. Two more observations with very low kHz QPO frequencies, had their upper kHz QPO considered unreal based on the colors and frequency correlations. For the final 11 twin kHz QPOs, the frequency of the upper kHz QPO ranged from 229 to 503 Hz. In one case also a third kHz QPO was marginally detected at a frequency about twice the lower kHz QPO and close to the frequency separation of the twin kHz QPOs.

In total 80 observations showed at least one kHz QPO, with their range covering more than a decade, extending from about 500 Hz down to 20 Hz, the lowest kHz frequency seen so far in LMXBs, testing the terminology of such components. The frequency separation of the twin kHz QPOs is spanning a range larger than the one covered by all previous twin kHz QPO detections from other sources. The fact that we do not see kHz QPOs above 500Hz, supports the thesis that Circinus X-1 is a Z source, since frequency ranges for kHz QPOs not extending to very high frequencies are typical for this class. (see Belloni *et al*, 2005). Interesting is also the fact that the upper kHz QPO seems to disappear at lower frequencies, despite the appearance of lower kHz QPOs there. An apparent decrease of rms amplitude of the higher kHz QPO seen in Figure 6.5 might explain this, although the statistics are not good enough. All these justify the peculiarity of Circinus X-1 and the difficulties in classifying it.

The new range of kHz QPO frequencies of Circinus X-1 allows unique tests of theoretical models. The decrease, for example, of the frequency separation with decreasing lower kHz QPO frequency was foreseen by the relativistic precession model. The predicted relation $\Delta\nu = \nu_u\sqrt{1-6\left(2\pi M\nu_u\right)^{2/3}/c^2}$ describes well our data points (figure 6.7), with the best fit giving a mass for the neutron star of $M = 2.0 \pm 0.1 M_\odot$ $\chi^2/\mathrm{dof} = 0.416$, which agrees with observations from other sources and that Stella & Vietri (1999) also adopted. The fit for the Alfen wave oscilaltion model of Zhang *et al* (1995) is even better ($\chi^2/\mathrm{dof} \simeq 0.6$) and gives for A (mean density) a value of 0.56 ± 0.02 – which translates to $R = 14.7 \mp 0.035\mathrm{km}\left(M/M_\odot\right)^{1/3}$ – but might be physically more difficult to support. The points could also be represented by a straight line (although with $\chi^2/\mathrm{dof} = 0.416$). The least square fit gave $\Delta\nu = 0.62(\pm0.05)\nu_u + 27.33(\pm19.54)$, which is inconsistent with a 2:3 ratio for the two kHz QPO frequencies ($\Delta\nu = 0.33\nu_u$) predicted by relativistic resonance models also for NSs (Kluźniak & Abramowicz, 2001); it does though agree well with a 1:3 ratio that could be picked up by resonances 1:2:3:5 (Kluźniak & Abramowicz, 2003). Since that would, however, be a combination frequency of the main 2:3 resonance, the weakness of the latter remains to be explained. The frequency of the third kHz QPO found in one observation could actually fit to this scenario as the radial epicyclic frequency, but its low significance and non-detectability in other

observations making it rather unlikely. Beat-frequency models in general, based on a constant frequency separation related to the spin frequency, would have difficulties explaining the up to 200Hz (factor 2) changing frequency separation of the kHz QPOs of Circinus X-1. Modified models explaining the decrease of the frequency separation with increasing accretion rate (Lamb & Miller, 2003) would need further elaboration to explain also a corresponding increase.

The large variability of the twin kHz QPO frequencies is a strong indication that the underlying source is not a black hole. The strong deviation from a 2:3 ratio and their simultaneous appearance supports this thesis. It is the first such evidence since the discovery of bursts about 20 years ago (Tennant *et al*, 1986) from its field. The fact that the kHz QPOs of Circinus X-1 lie in the frequency-frequency diagrams between the ones for NSs and black holes (Figure 2 of Psaltis, Belloni & van der Klis (1999)), justifies the debates on its nature. The low frequencies on the other hand speak for a massive neutron star, if for example the upper kHz QPO indeed associates with orbital motions, scaling like $1/M$.

6.5 Conclusions

QPOs do carry the imprint of the compactness of the LMXB's central object, but most likely are related with features in the disc rather than the neutron star itself. Burst oscillations on the other hand might be produced by oscillations on the neutron star surface, making Type-I X-ray bursts more interesting observationally for the identification of eigenmodes. Finite-temperature equations of state are needed for computing such oscillations numerically and data with high time-resolution are required for the observational analysis. A successful identification of non-radial oscillations from a neutron star, can also in X-rays allow to study the composition of neutron stars, still a holy grail in astronomy.

Figure 6.2: The color-color diagram of all public observations of Circinus X-1 that we used together with the 119 that we fitted (left panel), with a blow-up of the region containing all but one fitted observations (dotted box) with pointed out the ones showing kHz QPOs (right panel).

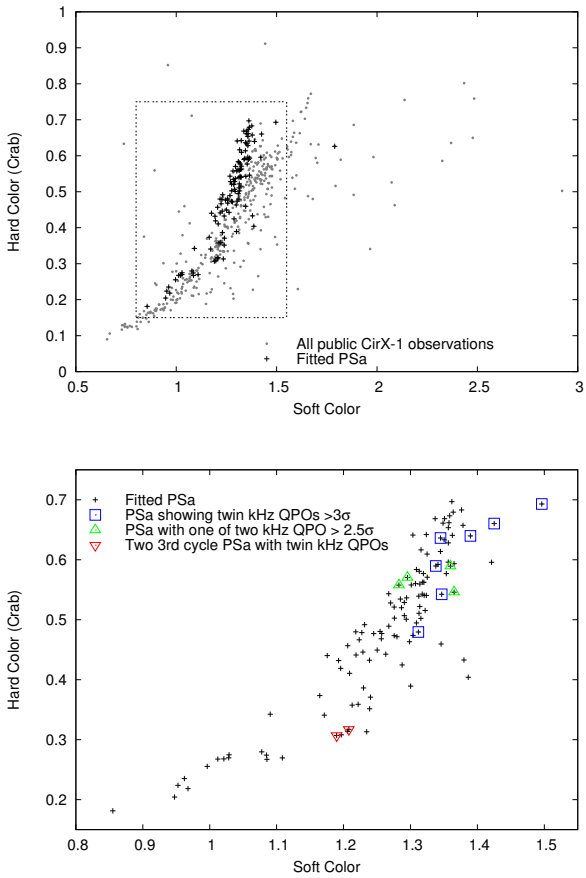

Figure 6.3: The Hard color against the Intensity, both normalized to Crab. In the left graph the Intensity is in logarithmic scaling. Symbols are as in Figure 6.2.

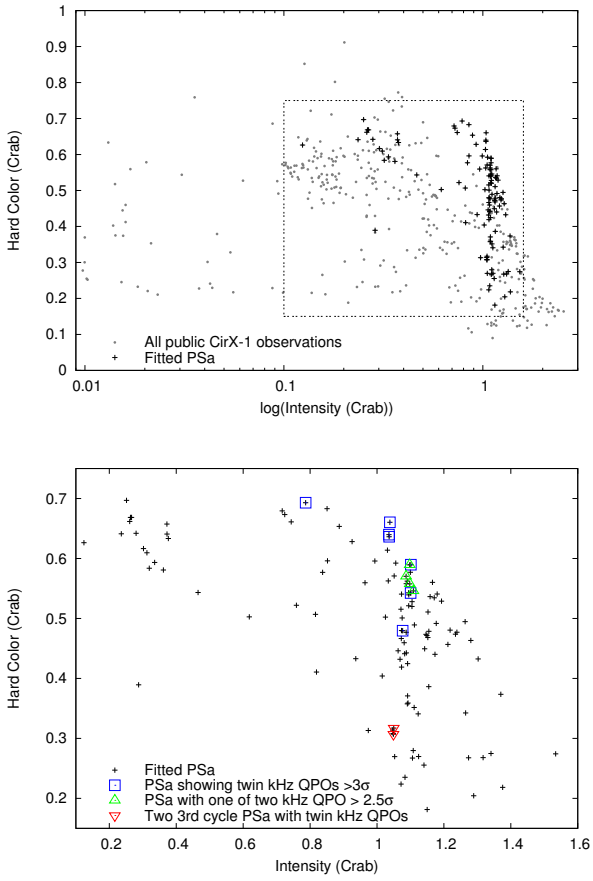

Figure 6.4: The frequency in ν_{max} representation of the upper and the lower kHz QPO as well as the hump and the break frequency against the low-frequency QPO in log-log scaling.

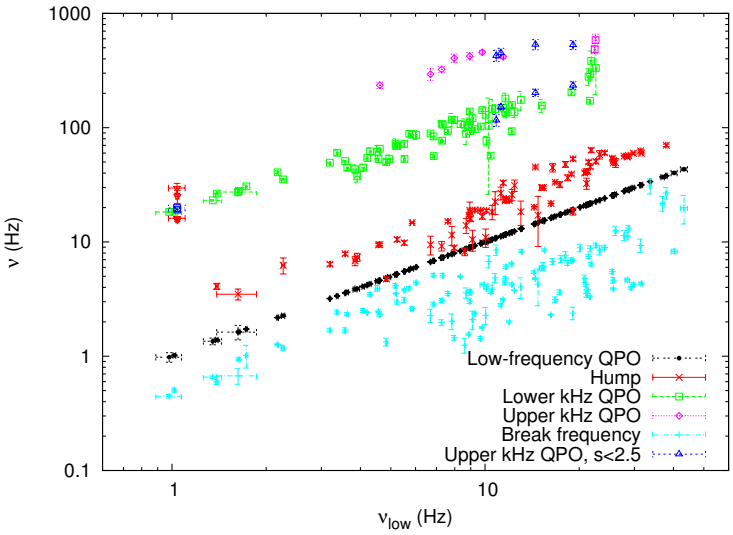

Figure 6.5: The rms amplitude of the twin kHz QPOs expressed in % as a function of the kHz QPO frequency. Single kHz QPOs are symbolized by small gray circles. All of them appeared to be lower kHz QPOs except of two high frequency (>400Hz) ones (see subsection. 6.3.2). Large black circles are the lower kHz QPOs of the 11 twin ones while blue squares are the corresponding upper kHz QPOs. The two most left pairs of points belong to the two lowest twin kHz QPOs of the 3rd observation (see subsection 6.3.1). If a single QPO is fitted, the two lower kHz QPOs in principle take the place in the diagram of the upper kHz QPOs of the same observation.

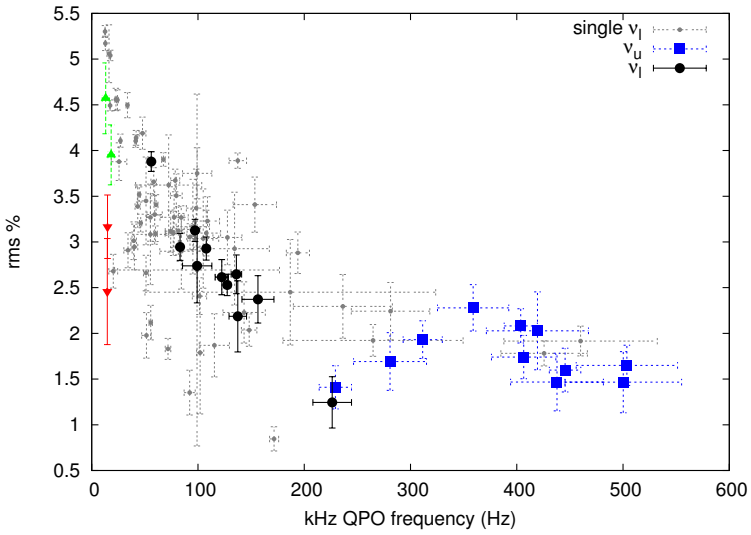

Figure 6.6: The centroid frequency of the upper kHz QPO and the lower frequency QPO against the lower kHz QPO in double logarithmic scaling, for Circinus X-1 (pink and blue points respectively) and other sources used by Psaltis, Belloni & van der Klis (1999). The red inverse triangles stand for the two 3rd cycle twin kHz QPOs, while the green triangles are for the same observations with one kHz QPO. The green lines is the power law fit to the Circinus X-1 data points and the red one the corresponding constant-ratio fit.

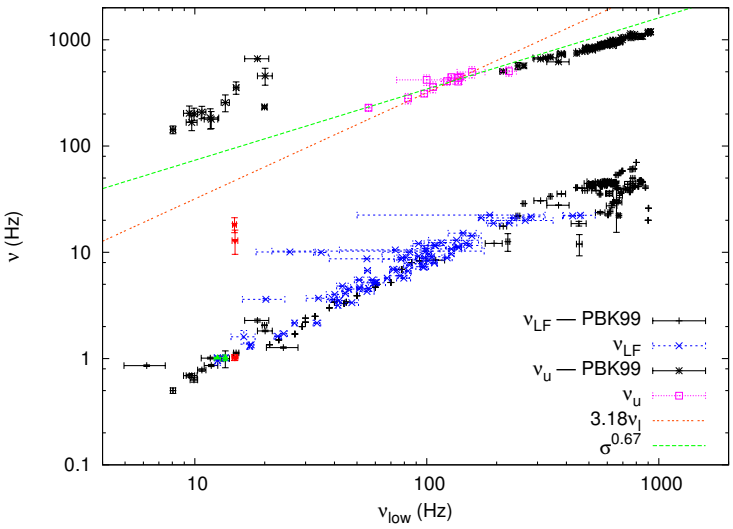

Figure 6.7: The frequency separation of the twin kHz QPOs against the upper kHz QPO frequency. Also plotted are the best linear fit of the points and the curve for the relativistic precession model for the best fitted value of M as well as the Zhang model for the best fitted value of A.

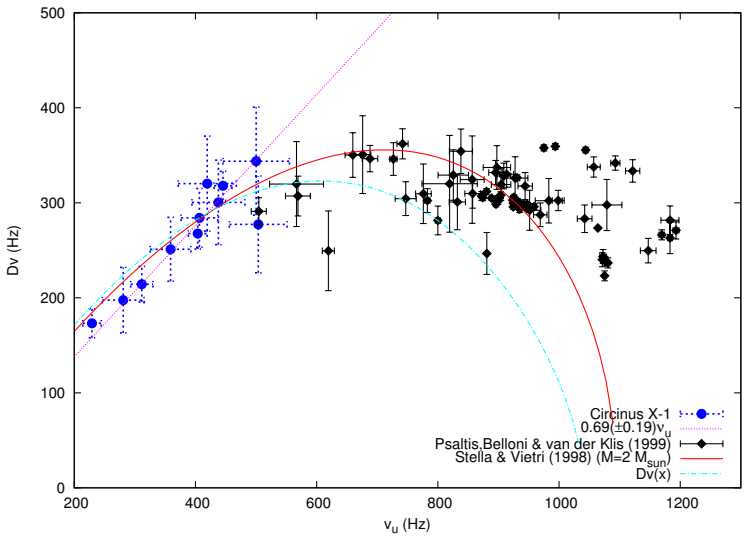

Figure 6.8: The histogram of all analyzed QPO-frequencies from Circinus X-1

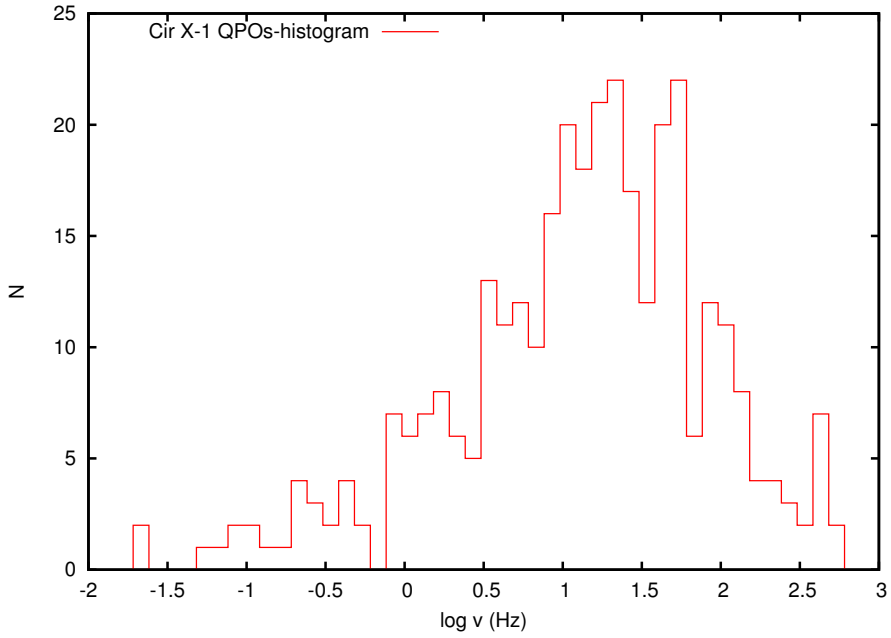

Appendix A

Geometrical & RNS units

A.1 Geometrical units

In this common convention, the speed of light c and the gravitational constant G are set to 1, which relates the SI and CGI units with each other:

$c = 1 \Rightarrow 1$ sec $= 3 \times 10^{10}$cm $\equiv 3 \times 10^{5}$km

$G = 1 \Rightarrow$ 1gr$= 7.415 \times 10^{-29}$cm

A.2 RNS units

The last degree of freedom for fixing the length unit is imposed by using the polytropic constant for that: $k^{\nu/2} = 1$

For the polytropic equations of state that we use in the paper ($\nu = 2$), this conditions translates in $1 = 14.76$km.

The choice of using $1M_{\odot} = 1$ for fixing the additional unit, gives a factor 10 difference in the numbers, since then $1 = 1.476$km.

One other possibility sometimes used is $1 = 1$km. In this work we exclusively used the RNS units when working dimensionless.

Appendix B

Associated Legendre polynomials

A list of some associated Legendre polynomials P_ℓ^m for some values of m and ℓ that interest us in this work.

$$
\begin{aligned}
P_0^0 &= 1 \\
P_1^0 &= \cos\theta \\
P_1^1 &= \sin\theta \\
P_2^0 &= \frac{1}{2}(3\cos^2\theta - 1) \\
P_2^1 &= \frac{3}{2}\sin 2\theta \\
P_2^2 &= \frac{3}{2}(1 - \cos 2\theta) \\
P_3^0 &= \frac{1}{2}\cos\theta(5\cos^2\theta - 3) \\
P_3^2 &= 15\cos\theta\sin^2\theta \\
P_4^2 &= \frac{15}{2}\sin^2\theta(7\cos^2\theta - 1) \\
&\vdots \\
P_\ell^2 &= \frac{\sin^2\theta}{2^\ell \ell}\frac{d^{\ell+2}}{d\cos^{\ell+2}\theta}\left(\cos^2\theta - 1\right)^\ell
\end{aligned}
$$

All associated Legandre polynomials cross zero at 0 and π. Even-m ones are symmetric, odd-m ones antisymmetric with respect to $\theta = 0, \pi$. They have an $(-1)^{\ell+m}$ parity.

Appendix C

The determination of the Poisson Level

For a high frequency analysis an accurate description of the Poisson noise power is required. This is mainly determined by the values of the deadtime and VLE-window [1]. The technical description of RXTE gave only approximate values for these and correspond to 10 and 150 respectively (Zhang *et al*, 1996). Conventionally, values of $8.5\mu s$ were used for the first, while an additional shifting at higher frequencies was introduces to compensate for deviation from the observations (Klein-Wolt *et al*, 2004). Recently, the VLE-window was estimated to $170\mu s$ via calibration (Jahoda *et al* , 2005). Since these values should, though, be unique for the satellite and the ones used till now do not agree with observations (see Figure C.1), we attempt to estimate them via the large sample of data that is provided for Circinus X-1. Provided the consistency of the Zhang-function no shifting should be applied to the computed PL.

We used of 84 representative RXTE observations of Circinus X-1; observations with high time-resolution were preferred but ones with lower resolution did not show a different picture, neither did ones with extreme high resolution (Nyquist frequency ∼33kHz). For avoiding power from the source we looked only at power above 1.6 kHz (up to the Nyquist frequency). All observations used for this analysis covered the whole energy range (channels 0–249). We used the function describing the Poisson power spectrum according to Zhang *et al* (1995):

$$P_\nu = 2 - 4r_0t_d\left(1 - \frac{t_d}{2t_b}\right) - 2\frac{N-1}{N}r_0t_d \times \left\{\frac{t_d}{t_b}\cos 2\pi\nu t_b + 2r_{VLE}t_{VLE}^2 \sin\frac{\sin \pi t_{VLE}\nu}{\pi t_{VLE}\nu}^2\right\},$$

where, t_d is the deadtime, t_{VLE} is the VLE deadtime, N is the number of points in the time series, r_0 is the source's count rate per detector, r_{VLE} is the VLE count rate per detector, $t_b = 1/2\nu_N$ and ν_N is the Nyquist frequency. By

[1] In our analysis only the 3rd setting appears and to that we refer.

using the first two as free parameters and knowing the other precisely, we fitted this function to the power spectra above 1.6 kHz, for each of the 84 observations. All fits gave a good representation of the data without need for shifting, for a t_d spanning a narrow range, while t_{VLE} was also well determined. The average values are

$$t_d = 8.87 \pm 0.2 \times 10^{-6}\text{sec}, \quad t_{\text{vle}} = 162^{+7}_{-12} \times 10^{-6}\text{sec}$$

These numbers are between the values given by the RXTE team (Jahoda *et al* , 2005) and those occasionally used by authors (Revnivstev *et al*, 2000; Wei, 2006). Whether the above values describe accurately the actual satellite properties needs to be tested among source with intensities at different range, as well as for the other VLE settings. For Circinus X-1 they give, in any case, a precise description of the noise and these values were used throughout the whole analysis.

We fitted the PS also with the previously used deadtime values $(8.5, 150\mu s)$ for the observations showing twin kHz QPOs (subsection 6.3.1) and found no systematic deviation compared to the suggested values. This was also the case when shifting at high frequencies, where occasionally an extra component was necessary at very high frequencies (above 1kHz) to account for the additional power appearing. The significant twin kHz QPOs stay significant even with the previously used deadtime values (with and without shifting).

Figure C.1: Two examples of observations whose Poisson Level (PL) would not have been estimated accurately enough with the common values for the deadtimes. Left: The PL according to the Zhang model and the previously suggested deadtime values (Zhang *et al*, 1995) would fail describing the power at high frequencies (dotted line). With a parallel shift, on the other hand, to fit data at high frequencies (dashed line) as introduced by Klein-Wolt *et al* (2004), the power at lower frequencies would be well overestimated, and even the third kHz QPO (see subsection 6.3.1) would exceed the 3σ significance level. The PL computed with the deadtime values estimated here (continuous line) does not need any shifting and follows more consistently the form of the data at the range ($>$ 1600Hz) where no contribution from the source is expected. Right: The strong frequency dependence of the PL at very high frequencies (observed for high time resolution) cannot be followed with the Zhang function for the previously used deadtime values. It lies systematically above the data for several kHz or partially above and partially below it when shifted, at frequencies where the data should purely describe noise.

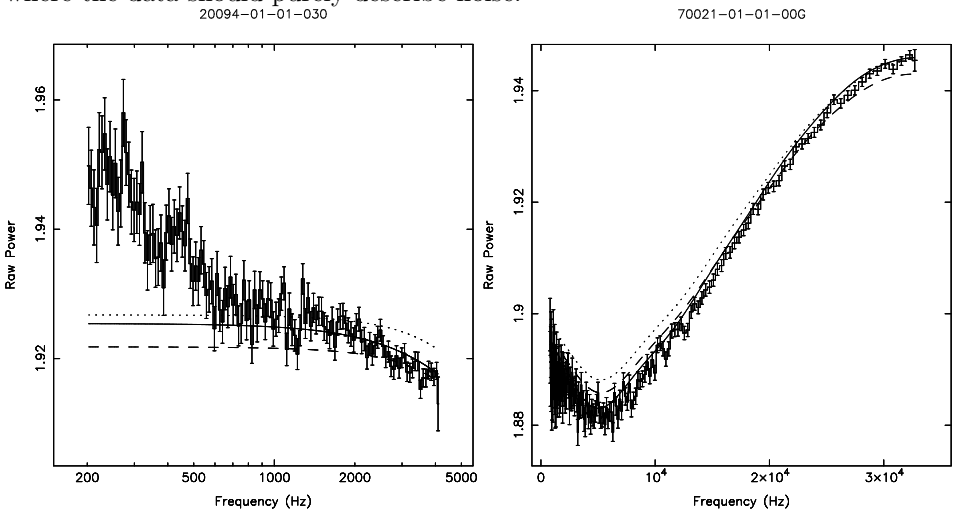

Bibliography

Altamirano D., van der Klis M., Mèndez M., Migliar S., Jonker P.G., Tiengo A., Zhang W., ApJ **633**, 358 (2005)

Andersson N., Astroph. J. **502**, 708 (1998)

Andersson N., Class. Quant. Grav. **20**, 105 (2003)

Andersson N. and Kokkotas K., Mon. Not. R. Astron. Soc. **299**, 1059 (1998)

Andersson N. and Kokkotas K., Int. J. Mod. Phys. **D10**, 381–442 (2001)

Astone P.*et al*, Class. Quant. Grav. **19**, 5449 (2002)

Bildsten L., Cumming A., Ushomirsky G, Cutler C., ASP Conference Series, **135**, 437 (1998)

Belloni T., Mèndez M., Homan J., A&A **437**, 209 (2005)

Belloni T., Psaltis D., van der Klis, ApJ **572**, 392 (2002)

Beyer H. R. and Kokkotas K. D., Mon. Not. R. Astron. Soc. **308**, 745 (1999)

Brink J., Teukolsky S. A. and Wasserman I., Phys. Rev. D **70**, 124017 (2004)

Brink J., Teukolsky S. A.and Wasserman I., Phys. Rev. D **70**, 121501 (2004)

Chandrasekhar S., Phys. Rev. Letter **24**, 611 (1970)

Chandrasekhar S. & Ferrari V., Proc. R. Soc. A **450** 463 (1995)

Clemens J. C. & Rosen R. , ApJ **609**, 340 (2004)

Cowling T. G., Mon. Not. R. Astron. Soc. **101**, 367 (1941)

Detweiler S. L. & Lindblom L., ApJ **292**, 12 (1985)

Dimmelmeier H., Stergioulas N. and Font J. A.*astro-ph/0511394*

Emden R. "*Gaskugeln*", Teubner, Leipzig (1907)

Finn L. S., Mon. Not. R. Astron. Soc. **232**, 259 (1988)

Fender R., Tzioumis T., Tudose V., ATel **563**, 1 (2005)

Fender R., Wu K., Johnston H., Tzioumis T., Jonker P., Spencer R., van der Klis M., Nature **427**, 222 (2004)

Font J. A., Dimmelmeier H., Gupta A. and Stergioulas N., Mon. Not. R. Astron. Soc. **325**, 1463 (2001)

Friedman J. L. and Schutz B. F., Astroph. J. **221**, 937 (1978)

Gierlinski M. & Done C., MNRAS, **342**, 1041 (2003)

Glass I.S, MNRAS, **268**, 742 (1994)

Goss W.M. & Mebold U., MNRAS, **181**, 255 (1977)

Greenspan H. P., "The theory of rotating fluids", Cambridge (1968)

Hough J., *www.ligo.caltech.edu/docs/G/G040400-00/G040400-00.pdf*

Iaria R., Spanó M., Di Salvo T., Robba N.R., Burderi L., Fender R., van der Klis M., Frontera F., ApJ, **619**, 503 (2005)

Jahoda K., Swank J. & Zhang W. /astro-ph0511

Johnston H. M., Fender R., Kinwah W.,MNRAS **308**, 415 (1999)

Jones C., Giacconi R., Forman W., Tananbaum H., ApJ,**191**, 71 (1974)

Klein-Wolt M., Homan J., van der Klis M., NuPhS **132**, 381 (2004)

Kluźniak W. & Abramowicz M., astro-ph/0105057 (2001)

Kluźniak W. & Abramowicz M., astro-ph/0304345 (2003)

Komatsu H., Eriguchi Y. & Hachisu I., MNRAS **237** 355 (1989)

Kokkotas K., MNRAS **268**, 1015 (1999)

Kokkotas K. and Schmidt B., Liv. Rev. Rel. **2**, 2 (1999)

Kojima Y. and Hosonuma M., Astroph. J. **520**, 788 (1999)

Kuulkers E., van der Klis M., Oosterbroek T., Asai K., Dotai T., van Paradijs J., LewinW.H.G., A&A **289**, 795 (1994)

Lai D., Mon. Not. R. Astron. Soc. **307**, 1001 (1999)

Lamb F.K. & Miller M.C., astro-ph/0308179

Ledoux P., ApJ **114**, 373 (1951)

Leigthon R.B., R.W. Noyes & G.W. Simon, ApJ **135**, 474 (1962)

Leins, PhD thesis (1994)

Lindblom L. and Ipser J. R., Phys. Rev. D **59**, 044009 (1999)

Lockitch K. H. , Andersson N. and Friedman J. L. , Phys. Rev. D **63**, 024019 (2001)

Lockitch K. H., Andersson N. and Watts A., Class. Quant. Grav. **21**, 4661–4676 (2004)

Lockitch K. H. and Friedman J. L. , Astroph. J. **521**, 764 (1999)

Lockitch K. H., Friedman J. L. and Andersson N. , Ph. Rev. D **68**, 124010 (2003)

Maisack M., Staubert R., Balucinska-Church M., Skinner G., Doebereiner S., Englhauser J., Aref'ev V. A., Efremov V. V., Sunyaev R. A., AdSpR **16**, 91 (1995)

Miller M.C., Lamb F.K., Psaltis D., ApJ **508**, 791 (1998)

Nollert H.-P., Phys. Rev. D **47**, 5253 (1993)

Nollert H.-P., Class. Quant. Grav. **16**, 159 (1999)

Nollert H.-P., PhD Thesis (1990)

Oosterbroek T., van der Klis M., Kuulkers E., van Paradijs J., Lewin W.G.H., A&A **297**, 141 (1995)

Oppenheimer J.R. & Volkoff G.M., Phys. Rev 56, 455-459 (1939)

Provost J., Berthomieu G. and Rocca A., Astron. Astroph. **94**, 126–133 (1981)

Psaltis D., Belloni T. & van der Klis M., ApJ **520**, 262 (1999)

Revnivtsev M.,Gilfanov M.,Churazov E., A&A **363**, 1013 (2000)

Rezolla L., Lamb F.K. & Shapiro S.L., ApJ **531**, 139 (2000)

Ruoff J., Phys.Rev.D. **63**, 064018 (2001)

Ruoff J. , private communication

Ruoff J., Stavridis A. and Kokkotas K., Mon. Not. R. Astron. Soc. **339**, 1170 (2003)

Samimi J., Share G.H., Wood K., Yentis D., Meekins J., Evans W.D., Shulman S., Byram E.T., Chubb T.A., Friedman H.,Nature **279**, 434 (1979)

Shirey R. E., Bradt H.L., Levine A.L., ApJ **517**, 472 (1999)

Shirey R. E., Bradt H.L., Levine A.L., Morgan E.H., ApJ **469**, 21 (1996)

Shirey R. E., Bradt H.L., Levine A.L., Morgan E.H., ApJ, 506, 374 (1998)

Stergioulas N. and J. L. Friedman, Astroph. J. **444**, 306 (1995)

Stergioulas N., Apostolatos T. & Font J. A., MNRAS **352** 1089 (2004)

Stergioulas N., Liv. Rev. **6**, 3 (2003)

Stella L. & Vietri M., Phys.Rev.L **82**, 17 (1999)

Tennant A.F., Fabian A.C., Shafer R.A., MNRAS **221**, 27 (1986)

Thorne K.S. & Campolattaro A. , ApJ **149** 591 (1967)

Tolman R.C., Phys. Rev, 55, 364-373 (1939)

Unno W., Osaki Y., Ando H. and Shibahashi H., *Non-radial Oscillations of Stars*, Tokyo: University Press (1989)

van der Klis M., astro-ph/0410551 (2004)

van der Klis M., in Astronomical Time Series. ASSL **218** 121 (1997)

van Straaten S.,van der Klis M., Mendez M., ApJ **596** 1155 (2003)

van Straaten S.,van der Klis M., Wijnands R., ApJ **619**, 455 (2005)

Wei D., MIT senior thesis, in preparation

Willke B. *et al*, Class. Quant. Grav. **23**, 207 (2006)

Yoshida S. and Kojima Y. , Mon. Not. R. Astron. Soc. **289**, 117 (1997)

Yoshida S.'I. and Eriguchi Y. , Astroph. J. **515**, 414 (1999)

Yoshida S.'I., Yoshida S. and Eriguchi Y., Mon. Not. R.Astron. Soc. **356**, 217 (2005)

Zhang W., Jahoda K., Swank J.H., Morgan E.H., Giles A.B., ApJ **449**, 930 (1995)

Zhang W., Morgan E.H., Jahoda K., Swank J.H., Strohmayer T.E., Jernigan G., Klein R.I., ApJ **469**, 29 (1996)

Acknowledgements

Since the doctorate is not just a personal academic achievement but also a part of someones life, I would like to spent some words for some of the people that contributed to this directly.

The first person to mention is Prof. Kostas Kokkotas whose suggestion to come here gave the incentive that finally led to this PhD. Even if not everything turned out as one would expect, his continuous supervision and mental support gave me the strength to bring this work to the end.

Next to my supervisor, PD. Hans-Peter Nollert, who gave me the opportunity to get involved in the doctorate and followed my progress to the end, I need to deeply thank Prof. Hanns Ruder for his support during my whole thesis. Not all PhD students have the opportunity to explore their fields of interest with so much freedom and propulsion. I may also be one of the few at the institute who may have benefited also from the presence of the other professor, namely Willy Kley. In general, I never felt isolated inside a working group and believe to have advanced from the presence of all members. From PD Jörg Frauendiener I got some very useful suggestions concerning numerical procedures, some of which were implemented in this work. Dr. Jochen Peitz offered the discussion-person that one often needs. At any chance Dr. Roland Speith was eager to aid. Technical issues were very common and without the friendly help of the system-administrators (Daniel Kobras, Dr. Christoph Schäfer, Dr. Richard Günther) much more time would have been lost. Daniel Kobras has also assisted me with his excellent language skills during the writing of proceedings or proposals. Erich Gaertig and Isabel Rica Mendez (later also Wolfgang Kastaun) were my closest colleagues regarding the working subject, and whom I wish the best in their further evolution. There is hardly any person in the institute with whom I have not scientifically interacted and whether still present or not, I devote the analogue piece of acknowledgment. Martina, Heike, Bettina, Anna and Birgit, each to her extent, helped in mastering the frequently occurring paperwork.

During my training position in Amsterdam, I had the privilege to work for Prof. Michiel van der Klis, next to which I advanced as a scientist and thank him for his interest and attention. Prof. Rudy Wijnands astonished me with the time he spent with me concerning scientific discussions as well as helping me with technical and administrative issues. To Diego Altamirano I owe a large part of my fast development using timing software and help at crucial points of the project. This warm feeling and eagerness for interaction was diffuse among

the members of the institute and the X-ray group in particular. Manuel Linares and Dr. Tom Maccarone were two more good examples of that. So did also Dr. Marc Klein Wolt when rejoining the group and even our disagreements in scientific issues helped me in improving my arguments. Although Dr. Martin Heemskerk always stressed out not being a system-administrator he was able and willing to help me whenever technical issues showed up. Dr. James Miller-Jones and Dr. Rhaana Starling assisted me with their language knowledge whenever needed. With my officemate Hanno Spreeuw I had an ideal working environment. Very important was the aid that I got for administrative issues, and for that I need to thank Lidewijde Stolte, Minou van Beurden, Annemiek Lenssen and Fieke Kroon. since their help went far more than their duties and they let me always feel as a full member of the institute. In general, it is seldom that so many people and groups are joined together so harmonically, and I was glad to be part of it.

Apart from members of my two host institutes, people from several other groups contributed occasionally. A significant and long-lasting contribution was made my Prof. Nik Stergioulas. Especially in the beginning of this work, Dr. Johannes Ruoff was always available and willing to help me with issues that can be problematic for a young PhD and of which is was well aware of. A special thank should be also given to Dr. Nils Andersson as well as Dr. Shin Yoshida. With Dr. Adamantios Stavridis, Miltos Vavoulidis and Mina Maniopoulou fruitful discussions took place.

Of course, in these years not only academic progress was made, but I also evolved as a individual, which also led in its way to this PhD. To list or even count all the people that contributed to this sounds illusive, and is not the scope of this text. Even if I have not always shown the appropriate piece of recognition, the connection with everyone will always stay in my heart. If one person was closest to me throughout this whole period and stood by me, that is my colleague and friend Nikos Papageorgiou. The last word is often kept for the people that are considered standard, but to whom the most warm thanks are devoted. These are my beloved family members, the ones no distance can alienate and the ones I lost.

Deutsche Zusammenfassung

Neutronensterne sind eines der möglichen Endstadien der Sternentwicklung. Sie stellen die kompakteste Form von Materie dar, die noch Dimensionen besitzt. Mehr als eine Sonnenmasse konzentriert sich auf ein Gebiet von ungefähr 20 km Durchmesser. Das macht eine relativistische Beschreibung der Gravitationswirkung erforderlich. Die Zustandgleichung der Materie unter diesen Bedingungen ist bislang nur ansatzweise bekannt. Pulsare sind nach allgemeiner Überzeugung das beobachtbare Gegenstück zum theoretischen Neutronensternmodell; Pulsare sind kompakte Objekte, die mit Perioden hinunter bis zu ~ 1 msec rotieren. Solch extreme Bedingungen sind auf der Erde nicht zu reproduzieren. Das macht schnell rotierende kompakte Objekte zu einem interessanten Forschungsgebiet mit einzigartiger Physik.

Elektromagnetische Strahlung ist bislang die einzige Möglichkeit, diese Objekte zu beobachten. Die von der allgemeinen Relativitätstheorie vorhergesagten Gravitationswellen öffnen jedoch ein vielversprechendes, neues Fenster, um Informationen zu gewinnen. Aktuelle Entwicklungen in der Laser-Interferometrie machen es wahrscheinlich, in naher Zukunft Gravitationswellen aus unserer Milchstraße auf der Erde nachzuweisen. Neben kurzzeitigen, besonders heftigen Phänomenen wie der Kollision zweier kompakter Objekte, stellen auch Schwingungen einzelner Neutronensterne eine Quelle möglicher Gravitationswellensignale dar. Unterschiedlichste astrophysikalische Szenarien können einen Neutronenstern zu Schwingungen anregen. Manche Schwingungsmoden werden instabil und strahlen dann besonders starke Gravitationswellen ab. Der Zeitraum ist lange genug, um das Signal auf der Erde nachzuweisen, vorausgesetzt, es liegen genaue Informationen vor über die genauen Schwingungseigenschaften wie beispielsweise Frequenz und Zerfallszeit. Damit lässt sich die Empfindlichkeit der Detektoren optimal auf das erwartete Signal abstimmen. Zahlreiche Studien wurden dadurch bereits motiviert.

Mit Hilfe vollrelativistischer, dreidimensionaler Zeitentwicklungsrechnungen ließe sich das Problem umfassend numerisch simulieren. Der nötige Aufwand stößt jedoch an die Grenzen aktueller Computerhardware. Einfachere Simulationen in verschiedene Näherungen haben bisher zu widersprüchlichen Ergebnissen geführt, vor allem deshalb, weil die häufig verwendete Annahme sphärischer Symmetrie für rotierende Sterne nicht zutrifft. Die vorliegende Arbeit versucht daher, das Problem auf einfache, aber konsistente Art zu lösen, um Einblicke in die grundlegenden Eigenschaften von Neutronensternschwingungen

zu erhalten. Die Schwingungen werden hier mit Hilfe linearer Störungstheorie beschrieben, das Verhalten der Neutronensternmaterie durch eine polytrope Zustandsgleichung modelliert. Die Ergebnisse im nichtrotierenden Grenzfall unter sphärischer Symmetrie bestätigen frühere Studien: So fand sich eine unendliche Reihe von Druckmoden über $\sim$2 kHz, Raumzeitmoden fallen in noch höhere Frequenzen ($\sim$10 kHz). Die zwei Gruppen von Moden sind in diesem Fall auf Grund von unterschiedlicher Parität klar getrennt.

Rotierende Sterne wurden statt in sphärischer in Achsensymmetrie untersucht, und durch kleine Auslenkungen der Form $e^{im\phi}$ gestört. Die θ-Abhängigkeit lässt sich durch zugeordnete Legendre-Polynome, P_ℓ^m, beschreiben. Das führt zu deutlich komplizierteren Gleichungen und Problemen im numerischen Verfahren. Das machte es nötig, Störungen der Raumzeit für die Rechnungen zu vernachlässigen und nur Änderungen in den hydrodynamischen Zustandsgrößen zu berücksichtigen. Diese so genannte Cowling-Näherung hat sich in vorherigen Studien bereits als konsistent und relativ genau erwiesen. Damit ließ sich letztendlich ein Eigenwertproblem formen, für das alle möglichen Lösungen gesucht wurden. Neben der unendliche Reihe von Druckmoden, tauchen nun auch Trägheitsmoden auf. Ihr Anzahl ist ebenfalls unbegrenzt, ihre Frequenz ist jedoch auf einen endlichen Bereich beschränkt, der sich je nach Rotationsfrequenz und Kompaktheit des Sterns verändert. Es konnte nicht ausgeschlossen werden, dass es sich hierbei sogar um ein kontinuierliches Spektrum handelt. Ist der Wert des azimuthalen Index m gröser als zwei, sind alle Trägheitsmoden instabil. Für sehr große Werte von m überlappt deren Frequenzbereich mit dem der Druckmoden.

Während Druckmoden sich sowohl über ihre Eigenfunktionen, als auch ihren Frequenzbereich leicht identifizieren lassen, konnten einzelne Trägheitsmoden nur deutlich schwerer extrahiert werden. Der geringe Abstand zwischen den Moden im Frequenzraum macht es notwendig, jeweils die Eigenfunktionen zu Hilfe zu ziehen. Die zeigen in diesem Fall jedoch ein kompliziertes Verhalten, da sich die Beiträge verschiedener ℓ vermischen. Nichtsdestotrotz konnten Moden identifiziert und über wachsende Auflösungen hinweg verfolgt werden. Mit Blick auf bereits bekannte Charakteristika der θ-Komponente der Geschwindigkeitsstörung konnte eine ähnliche Mode in einem langsam rotierenden Modell nachgewiesen werden. Deren Frequenz – die $1,41$-fache Rotationsrate des Sterns– stimmt mit den Ergebnissen früherer Studien in diesem Bereich überein. Für schnell rotierende Modelle eines Neutronensterns lässt sich eine ähnliche Mode bestimmen, ihre Eigenfunktion weicht jedoch stärker vom erwarteten Verlauf ab, und auch die Frequenz ist nicht etwa niedriger (wie von andere Studien erwartet), sondern höher als bei langsamer Rotation.

Obwohl einige neue allgemeine Eigenschaften des Spektrums der Trägheitsmoden gefunden wurden, bleibt es nach wie vor problematisch, einzelne Moden zu identifizieren. Grund dafür ist die Anwesenheit einer unendlichen Anzahl von Trägheitsmoden – möglichweise sogar eines Kontinuums –, das die r-Mode vollständig unterdrücken könnte. Doch selbst wenn sie auftritt, ist ihr Verlauf vermutlich kontaminiert durch angrenzende Lösungen. Vor allem bei schneller Rotation erschwert das die Identifikation oder macht sie vielleicht sogar unmög-

lich. Mehr Speicher und Rechenleistung ist nötig, um diese Fragen durch höher aufgelöste Simulationen zu klären. Vor allem dreidimensionale Zeitentwicklungsrechnungen könnten eine Antwort liefern. Endgültige Klärung brächte der Nachweis einer solchen Mode in einem Gravitationswellendetektor.

In der Auswertung des elektromagnetischen Signals aus dem kompakten Röntgenbinärsystem Circinus X-1 fanden sich keine Hinweise auf nichtradiale Neutronensternmoden, die eine Verbindung hergestellt hätten zwischen quasiperiodischen Oszillationen (QPOs) und Quasinormalmoden. Die beobachtete Frequenzbreite der Kilohertz-QPOs konnte jedoch auf einen neuen Bereich ausgedehnt werden, der einzigartige Tests verschiedener QPO-Modelle erlaubt. Korrelationen zwischen Frequenzen von QPOs bestätigten, dass es sich bei dem zugrundeliegenden Objekt um einen Neutronenstern handelt.